CdSe based Nanowires for the Photocatalytic Production of Hydrogen Gas

A dissertation submitted in partial fulfilment for the degree of Master of Science in Chemical Engineering

by

Ilyaas Abdullah

2018

Supervised by:

Associate Professor Pieter Levecque

Department of Chemical Engineering

University of Cape Town

Associate Professor Mark Blumenthal

Department of Physics

University of Cape Town

Abstract

Photocatalytic production of hydrogen was investigated towards achieving a decarbonized supply of hydrogen gas for clean energy conversion technologies such as the proton exchange membrane fuel cell (PEMFC). This study uses a template-directed electrodeposition technique to synthesize multi-segmented CdSe based nanowires for use as a photocatalyst device for hydrogen production.

CdSe, Ni, Au and Pt nanowires were successfully synthesized with dimensions ranging from 100 nm to 350 nm in diameter and up to 10 μm long. The CdSe stoichiometry was not easily controlled despite following literature protocols and requires a more systematic investigation. The electrodeposition of Ni nanowires was found to be most effective with very few problems encountered. Improvements in the morphology of Au and Pt nanowires were made by using a constant current as opposed to constant potential electrodeposition techniques.

Multi-segmented nanowire devices were prepared with nanowires left embedded in a porous anodized aluminium oxide (AAO) template. Polymer PEDOT:PSS and noble metal Pt was used as an anode and cathode electrocatalyst materials respectively. A prototype photocatalytic testing system was set-up using a 1600 W xenon arc lamp as a light source, an in-house made photoreactor as the device holder, and a mass spectrometer for online gas detection measuring ionic currents of evolved species. The set-up was able to successfully detect hydrogen evolved during the tests but does require further development if more complete photocatalytic testing is to be conducted in future.

Photocatalytic hydrogen production from the irradiated devices was inconclusive, but hydrogen detection from devices was observed in an 80 % MeOH solution with no irradiation. Through these tests it was learned that photocatalytic activity needs to be differentiated from regular catalytic activity. This is particularly the case if testing is conducted in organic media and if the photocatalytic phenomena is to be properly isolated and understood correctly.

Plagiarism Declaration

I know the meaning of plagiarism and declare that all the work in the document, save for that which is properly acknowledged, is my own. This thesis/dissertation has been submitted to the Turnitin module (or equivalent similarity and originality checking software) and I confirm that my supervisor has seen my report and any concerns revealed by such have been resolved with my supervisor.

Name: Ilyaas Abdullah

Student Number: ABDILY001

Signature: Signed by candidate

Date: 08/04/2018

Acknowledgements

I would firstly like to acknowledge my parents and my sister, without which this dissertation would not have been written. Their unflinching belief in me and support for my pursuits has been an invaluable part of my journey thus far.

To my family and friends for always encouraging me and the countless conversations which were motivating, inspiring and that has kept me mostly sane – Thank you.

A big thanks to the incredibly knowledgeable people in the electrochemistry group, Nobhule, Colleen, Archie, Rhiyaad, Jessica, And Graham. Thank you for your guidance and input towards my project and making the lab a pleasant place to work in.

In Chemical engineering, thanks to Gideon, Waldo, Rachel, Eghsaan and Portia who were ready to help at any point. Thanks to Dr. Jack Fletcher (JV) for helping me set-up the Mass Spec. Thank you to the administration staff, Lee-Anne, Shireen, Belinda and Leigh who made the administration aspects a breeze and who I could go to any problem with to get sorted. Thanks to the cleaning staff in the labs and the desk spaces I worked in, even though I didn't see you all the time, working in a clean environment is a privilege.

To my co-supervisor, Mark Blumenthal, thank you for assimilating me into the Physics Department so seamlessly, I found the collaboration between Science and Engineering incredibly enlightening. Thanks for being such a good teacher and always being open to explain complicated semiconductor physics topics to a simple engineer. Your patience and support has been invaluable. Thank you to Nasheeta, Marija and Mirette for making it easy for me to get going with your support and openness to discuss any ideas. The brain storming sessions in-front of the white board helped a lot. Thanks to the technical support staff in the Physics department, Kerwin and Clint who were always ready to help.

Last, but not least, thank you to Pieter Levecque my main supervisor for being such a great supervisor who managed to move me along without pushing me, for weighing in when I had no clue and for making it possible for me to do a project that I'm passionate about. Your consistent support and guidance has been key to the completion of this project.

Table of Contents

List of Figures and Tables

Chapter 1: Introduction

In the imminent era of environmental sustainability, the proton exchange membrane fuel cell (PEMFC) is a strong contender in the arena of efficient and clean energy conversion. Capable of practical fuel utilisation efficiencies of up to 55 % at temperatures as low as 80 °C and pressures between 1 - 2 bar and additionally known for operating silently, makes this technology an attractive option. The environmental sustainability however, as well as the optimisation of performance of this technology is tied to how hydrogen as the fuel is industrially produced. The dominating process routes for hydrogen production are natural gas and oil steam reforming, coal gasification and electrolysis of water (Logan, 2004). Unfortunately, these processing routes typically either have direct or indirect carbon dioxide emissions associated with them.

Decarbonised production of hydrogen from renewable energy sources i.e. solar, wind or hydro etc. used in combination with technologies like the PEMFC drastically reduces its environmental impact. Furthermore, it also increases the operating lifetime of PEMFCs because fossil fuel sources of hydrogen typically contain catalyst poisons such as H_2S, CO and CO_2 etc. These poisons are especially problematic in PEMFCs with Pt/C type electrocatalysts where severe drops in performance of PEMFCs has been shown to occur after exposure to <100 ppm levels of the contaminants mentioned after only a few hours (Cheng *et al.*, 2007). Moreover, renewable production of clean hydrogen is a solid foundation upon which a sustainable hydrogen energy infrastructure can be built, the development of this infrastructure is a pre-requisite for technologies such as PEMFCs to be implemented at large scales.

The possibility of renewable hydrogen production was first realised when Fujishima & Honda (1972), irradiated a TiO_2 semiconductor electrode submerged in water in an electrochemical set-up and evolved H_2 at the counter electrode. Advantageously, this observation in addition to recent advances in the fields of semiconductors, nanotechnology and heterogenous catalysis, has resulted in the exponential growth of the field heterogenous photocatalysis. Since then a great deal of research efforts have been made to replicate this "Fujishima effect" using different semi-conducting materials with various morphologies, sizes and prepared using a variety of synthesis methods for applications in both energy and environmental spaces (Lee, 2005; Coronado, Fresno & Portela, 2013; Preethi & Kanmani, 2013; Ismail & Bahnemann, 2014).

Of these semiconducting material options, cadmium chalcogenides (CdX, X = Se, Te and S) are an interesting class of semi-conducting photocatalyst material for hydrogen production due to their narrow optical band gap sizes, small enough to absorb visible as well as UV light. This

attribute makes them more effective at harvesting solar energy than materials only capable of absorbing UV light such as wide optical band-gap materials like TiO_2. Although the main drawback of using these materials aside from their inherent toxicity is their poor stability in photocatalytic systems where they are deactivated by photo-oxidation processes (Xu, Huang & Zhang, 2016). Inclusion of metals, carbon, and polymers among other strategies have been used to modify these cadmium compounds to be more stable for use as a photocatalyst material.

The advent of nanotechnology has additionally made way to a multitude of useful characteristics for these semiconducting materials by inducing alternate chemical, electronic and optical properties, different to their bulk forms for exploration (Jie *et al.*, 2010). Of recent interest has been one-dimensional nanomaterials consisting of nanowires, nanorods, nanoribbons and related nanostructures with at least one of their physical dimensions ranging from ca. a few nm to a few 100 nm. Furthermore, electrochemical synthesis techniques using aqueous electrolytes of these one dimensional nanostructures have shown to be a simple, low cost and facile means for the synthesis of these nanostructures (Lai & Riley, 2008; Shpaisman & Givan, Uri Patolsky, 2010; Kim *et al.*, 2013).

The main aim of this investigation was to incorporate semiconductor cadmium selenide (CdSe) in the form of nanowires into a photoactive alumina-based device. In addition to CdSe, these devices also include metal co-catalysts materials such as Ni, Au and Pt as has been carried out by previous researchers (Peña *et al.*, 2002; Mubeen *et al.*, 2013; Fawzy, 2016). These devices are prepared using a template-directed electrodeposition technique to form nanowires with multiple segments of connected materials protected by the alumina template that they are grown in.

Proper fabrication of these devices is an important first task before photocatalytic testing can be carried out. Therefore, further aims included: The optimisation of the electrodeposition parameters & techniques for the electrodeposition of CdSe as well as co-catalyst metals Ni, Au & Pt. As well as, the initial design and development of an online hydrogen detection method using mass spectrometry for the detection of photo-catalytically produced hydrogen specifically from template type photocatalytic devices. This includes the design and fabrication of a suitable glass vessel or photoreactor in which optimally fabricated photocatalytic devices can be tested.

The work presented here will form part of further studies to better the understanding of nanowire electrodeposition methodology for the creation of photocatalyst devices as well as photocatalytic testing of these type of devices.

Chapter 2: Literature Review

This chapter draws attention to significant aspects in the literature terrain for photocatalytic hydrogen production. More specifically it looks at the technological routes currently available for hydrogen production from fossil fuels as well as water as a hydrogen source in section 2.1 Section 2.2 introduces some fundamental aspects of heterogenous photocatalysis and the material requirements needed to achieve photocatalytic water splitting with section 2.3 focusing on some significant development in the field since the Fujishima & Honda (1972) benchmark. The following section, 2.4, focuses specifically on the use of cadmium selenide (CdSe) as a photocatalytic semiconducting material for visible light driven hydrogen production with section 2.5 elaborating on the template electrodeposition technique used for the synthesis of CdSe nanowires. Section 2.6 expands on section 2.5 and 2.4 by looking at multi-component photocatalytic systems for improved photocatalytic production of hydrogen using CdSe. Finally, section 2.7 considers the aspects of testing photocatalytic devices and the associated challenges in the field, specifically, regarding standardised performance criteria. These sections of this chapter will lay the foundation upon which the scope, objectives and hypothesis of the current study have been built.

2.1: Hydrogen Production

The hydrogen production industry is based on the reality that diatomic hydrogen (H_2) rarely occurs naturally on Earth. It therefore needs to be extracted from compounds in which it does occur such as hydrocarbons or water. This is achieved using various technological options that can be powered by various energy sources or combinations thereof.

In recent years, due to our current environmental challenges and the subsequent development of the hydrogen economy, the direction of this industry is fast moving to the production of "green hydrogen" .This involves the production of hydrogen using cleaner and more readily available energy and hydrogen sources (Dincer & Acar, 2014). In addition to being an attractive solution to current environmental challenges, green hydrogen production has the potential to reduce geopolitical tension related to energy security (Sharma & Ghoshal, 2015) as well as help maintain economic security (Holladay *et al*., 2009).

2.1.1 Production Overview

Global hydrogen production was estimated to be 50 million metric tons per year on average (Bakenne, Nuttall & Kazantzis, 2016).The means of production is still largely tied to the refining

industry with 47% and 30% produced from the reforming of natural gas and oil respectively, while 19% is derived from the gasification of coal and 4% from the electrolysis of water (Stiegel & Ramezan, 2006).

In the United States, The bulk of hydrogen produced is reported to be used for the production of ammonia (49%), petroleum refining (37%) and methanol production (8%) (Kroschwitz & Nees, 1995). These numbers are expected to change depending on the country and whether or not they export or import refined petroleum for their needs. The fraction of hydrogen not used in the petroleum refining or ammonia industry is demanded in a wide variety of other industries of which some examples are the fuel cell and metal refining industries (Bakenne, Nuttall & Kazantzis, 2016).

2.1.2 Hydrogen production from fossil fuels

The process routes that dominate hydrogen production using fuel processing technology for gas and liquid phase feed streams include steam reforming (SR), auto-thermal reforming (ATR) and partial oxidation (POX). These three options are typically compared based on several criteria: The operating temperature, the ratio between H_2 and CO produced, oxygen requirements and the use of a catalyst. All three of these options however, typically require desulphurisation before further purification (Holladay *et al*., 2009). Solid hydrocarbon feeds such as coal, first undergoes gasification which converts solid carbon to gaseous hydrocarbons via thermal treatment. This gaseous mixture is then reformed into hydrogen using either of the reforming process options.

In addition to reforming, pyrolysis of hydrocarbon materials involves the thermal decomposition of the hydrocarbon into solid carbon and hydrogen in the absence of water or air at temperatures close to 1000 °C. The advantage of this process is that no CO_2 or CO emissions are made since solid carbon is formed, this removes the need for further processing as well as carbon capture and sequestration (CCS) (Nikolaidis & Poullikkas, 2017). This is typically a catalytic process, making use of transition metals such as Ni, Fe and Co as catalyst which allows the reaction to happen at significantly lower temperatures but can be deactivated by the build-up of carbon in the system (Muradov, 2003).

2.1.3 Hydrogen production from water

Water is an attractive carbon free source of hydrogen due to its abundance on Earth and with the only by-product of its decomposition being oxygen:

$$2H_2O\,(l) \quad \leftrightarrow \quad 2H_2(g) + O_2(g) \qquad \Delta G^\circ = 237\ \text{kJ/mol}$$

The three broad classes of hydrogen production from water splitting are thermolysis, the use of thermal energy, electrolysis, use of electrical energy and photolysis, use of light energy.

2.1.3.1: Thermolysis of water

To decompose water using heat energy, temperatures of ca. 2500 °C are required, achieving efficiencies of around 50% (Holladay *et al*., 2009). A lack of sustainable heat sources to continuously operate at 2500 °C is one of the main barriers for direct thermolysis of pure water, although developments in large scale concentrated solar energy may make this more viable (Nikolaidis & Poullikkas, 2017).

To lower the temperature requirements, homogenous catalyst reagents are used to effect water splitting (thermochemical water splitting) through a few reaction cycles with lower temperature requirements. An example of a promising reaction route is with the use of the copper-chlorine (Cu-Cl) thermochemical cycle (Nikolaidis & Poullikkas, 2017), this multi-stage water splitting cycle examined by Orhan, Dincer & Rosen (2008) is illustrated in Figure 2. 1.

$$2CuCl_2\ (s)\ + H_2O\ (g) \rightarrow CuO^*CuCl_2\ (s) + 2HCl\ (g)\quad \boldsymbol{T = 400\ °C}$$

$$CuO^*CuCl_2\ (s)\ \rightarrow 2CuCl\ (l) + 0.5O_2\ (g)\quad \boldsymbol{T = 500\ °C}$$

$$4CuCl\ (s) + H_2O\ \rightarrow 2CuCl_2\ (aq) + 2Cu\ (s)\quad \boldsymbol{T = 25 - 80\ °C}$$

$$CuCl_2\ (aq) \rightarrow CuCl_2\ (s)\quad \boldsymbol{T > 100\ °C}$$

$$2Cu\ (s) + 2HCl\ (g) \rightarrow 2CuCl\ (l) + H_2\ (g)\quad \boldsymbol{T = 430 - 475\ °C}$$

Figure 2. 1: Cu-Cl thermochemical cycle as examined by Orhan, Dincer & Rosen (2008)

Another example includes a novel two-stage SnO_2/SnO thermochemical cycle presented by Abanades *et al*. (2008). Although the splitting of water for this cycle is achieved in two-stages, a temperature up to 1600 °C is needed to drive the first stage. This in addition to minimizing the Gibbs free energy (ΔG) for each reaction, maximising the reaction rates and ensuring there are no additional by-products are among some of the considerations needed for the optimisation of these cycles (Holladay *et al*., 2009).

2.1.3.2: Electrolysis of water

Water electrolysis is the transformation of electrical energy into chemical energy (hydrogen bonds). This occurs as an electrochemical process whereby high-purity hydrogen up to 99.999% pure can be produced (Dincer & Acar, 2014). Technologically, water electrolysis is carried out

using three main routes. First, and most well developed is the alkaline electrolysis route, second, proton exchange membrane (PEM) electrolysis and third, solid oxide electrolysis cells (SOEC)(Holladay *et al.*, 2009).

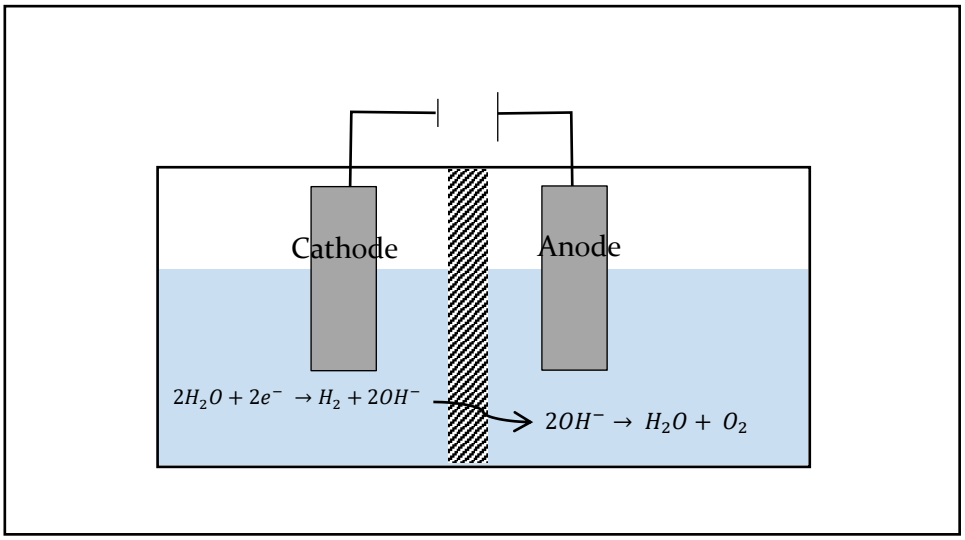

Figure 2. 2: Schematic of alkaline electrolysis

Hydrogen production via alkaline electrolysis is illustrated in Figure 2. 2 and makes use of a basic liquid electrolyte (ca. 30% KOH) separated by a diaphragm permeable to hydroxide ions and water. For the electrodes, Ni with catalyst coatings such as Pt and C are used as the cathode, whereas catalyst coating such as Mn, W, & Rh oxides or Co and Fe can be used for the anode (Holladay *et al.*, 2009; Carmo *et al.*, 2013).

The main challenges associated with alkaline electrolysis are limitations in the achievable current densities (0.2 – 0.4 mA.cm $^{-1}$) due to ohmic losses across liquid and solid layers; decreases in efficiency due to hydrogen and oxygen cross-over; and difficulty in operating at high pressure resulting in large stack sizes (Carmo *et al.*, 2013). The low cost and long-term stability of this technology however, maintains its relevance for large scale hydrogen production.

Development and use of solid polymer-based electrolytes have allowed fuel cell technology as well as PEM water electrolysis to flourish, which is the main competing technology to alkaline water electrolysis for hydrogen production. PEM electrolysis is illustrated in Figure 2. 3.

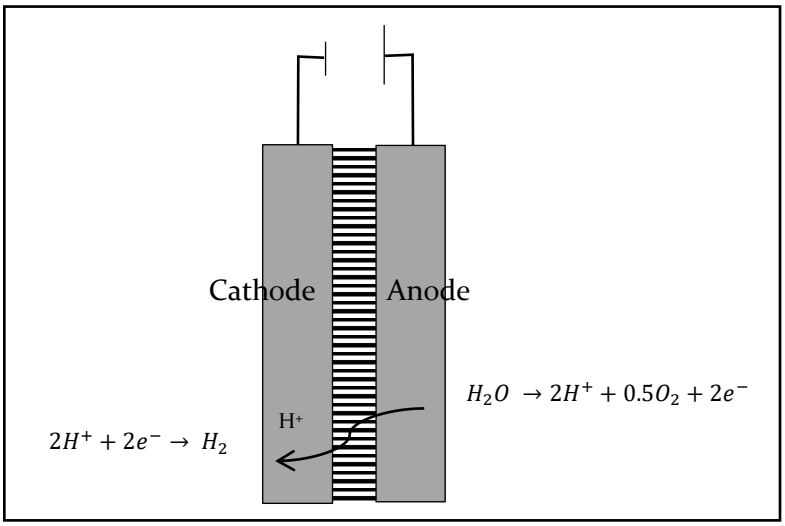

Figure 2. 3 Schematic of PEM electrolysis

Conversely to alkaline electrolysis, water is fed to the anode side for PEM electrolysis where oxygen is evolved, and hydrogen ions are conducted across a solid polymer electrolyte with hydrogen evolved at the cathode side. Catalyst electrode materials are typically noble metals such as Pt and Ir for the cathode and anode reactions respectively with Nafion® as the polymer electrolyte membrane material (Holladay *et al*., 2009; Carmo *et al*., 2013). Much higher current densities (0.6 – 2.0 mA.cm^{-1}) can be achieved with this more compact cell configuration with more or less the same efficiency to that of an alkaline system (Carmo *et al*., 2013).

More recently, SOEC has attracted attention for being a more energy efficient means for hydrogen production compared to alkaline and PEM electrolysis (Wang, Wang, *et al*., 2014). SOEC enables the decomposition of steam at temperatures between 600 – 1000 °C, this has the advantage of lowering the theoretical thermodynamic potential (1.23 V) required for water-

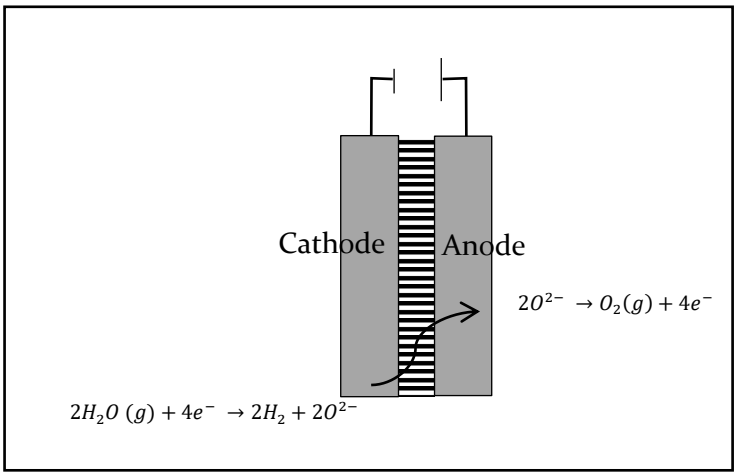

Figure 2. 4 Schematic of solid oxide electrolysis

splitting as well as reducing the required overpotentials and ohmic losses (Wang, Wang, *et al.*, 2014). The most commonly used solid oxide electrolyte used for this system is Y_2O_3 (YSZ) doped ZrO_2 (Yu *et al.*, 2012) with YSZ also used in both anode and cathode electrode materials.

As is illustrated in Figure 2. 4, SOECs operate by feeding steam to the cathode side producing hydrogen gas and O^{2-} ions. These ions are conducted through the solid oxide membrane to the anode side where oxygen gas is evolved. One of the major challenges with SOEC is having a suitable energy source for steam generation which brings down its overall efficiency (Holladay *et al.*, 2009). One significant route being explored to address this, is the use of generated waste heat from various industries (Ni, Leung & Leung, 2007) and most notably from nuclear power waste heat.(Yildiz & Kazimi, 2006).

2.1.3.3: Photolysis of water

Of the three technological routes to hydrogen production from water splitting, photolysis of water which refers to either photocatalytic or photoelectrochemical (PEC) hydrogen production, is a field still very much in its early R&D phase (Dincer & Acar, 2014). Photolysis of water refers to the direct decomposition of water into H_2 and O_2 using light energy (artificial or solar) and some type of photocatalyst material to facilitate the decomposition reaction. Since it has been observed that more light energy strikes the Earth in an hour than all the energy consumed in a year (Lewis & Nocera, 2006), the dire need to exploit this clean and renewable energy source is a main driver in the development of photocatalytic materials.

The concept of water photolysis for hydrogen production was first demonstrated when UV light was used to drive a photoelectrochemical cell consisting of a TiO_2 anode and a platinum black cathode using a small applied potential/bias (Fujishima & Honda, 1972).

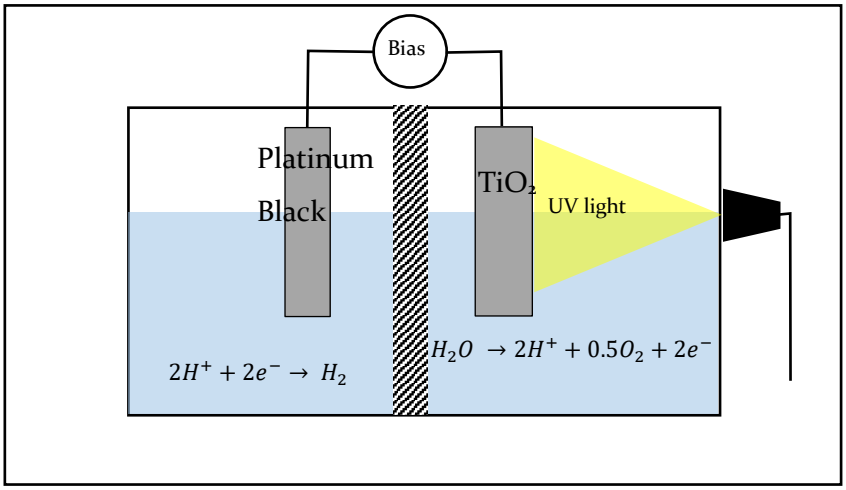

Figure 2. 5: Schematic of TiO2 photoelectrochemical hydrogen production adapted from Fujishima & Honda (1972)

This process is illustrated in Figure 2. 5, where electrons are liberated by an irradiated semi-conductor electrode, which then travel through an external circuit effecting the reduction of hydrogen ions at the cathode and oxidation of water at the anode.

This proof of concept study by Fujishima & Honda (1972), is widely recognized as the seed of heterogenous photocatalytic water splitting which has, since then made progress in a range of different areas. This includes but is not limited to: elucidating the photocatalytic mechanism, the development of various novel UV and visible light active photocatalyst materials, band-gap engineering though doping, dye sensitisation and the use of co-catalysts, combination of semi-conductor materials to form z-scheme systems and the development hydrogen generation systems (Chen, Shen, *et al.*, 2010).

2.2: Heterogenous Photocatalysis

Many consider heterogenous photocatalysis to be a fairly recent concept, with interest being ignited in the early 1970s when Fujishima & Honda (1972) first demonstrated the electrochemical decomposition of water on a TiO_2 photocatalyst anode with H_2 gas being evolved at a Pt black cathode. Although it is true that their pioneering study sparked widespread interest in the development of better photocatalytic materials and systems, it has been chronologically shown that heterogenous photocatalysis actually finds its roots in the early 1900s (Serpone *et al.*, 2012). One of many examples of heterogenous photocatalysis preceding the 1972 benchmark is the use of ZnO for the photo-oxidation of isopropanol looking specifically at chain termination mechanisms (Ikekawa *et al.*, 1964).

2.2.1 The Photocatalytic Mechanism

Photocatalysis, and more specifically heterogenous photocatalysis is the process of driving a targeted chemical change on a solid catalytic surface using light energy. It is well agreed upon (Motegh, 2013; Ismail & Bahnemann, 2014; Spasiano *et al.*, 2015) that the photophysical mechanism of a photocatalyst is as follows:

1. **Formation** of electron & hole charge carriers upon absorption of photons with the correct minimum energy.
2. **Separation and migration** (**or recombination**) of electrons & holes to the solid surface.
3. **Redox reactions** of charge carriers at the solid surface with adsorbed species.

The mechanism described above is equivalent to the formation of an excited state of the material which is also the starting point in chemical change for both thermal and electro catalysis. A schematic representation of how a photocatalyst functions corresponding to the steps above is shown in Figure 2. 6.

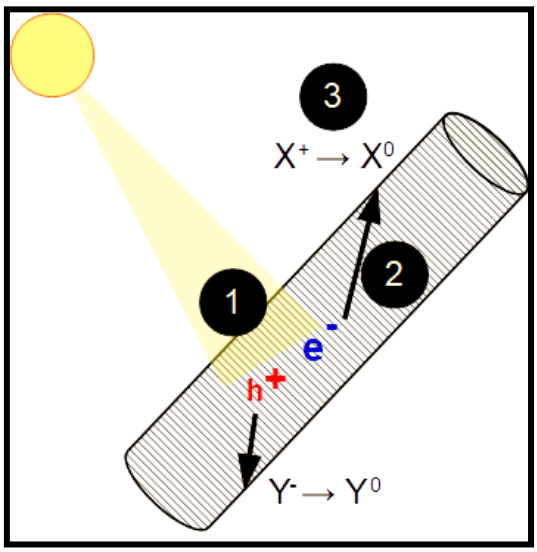

Figure 2. 6: Schematic of generic photocatalytic process

Fundamentally, a pre-requisite for the process shown in Figure 2. 6 to occur is that the light energy (hν) must be equal to or greater than the bandgap energy (E_g) of the photocatalyst semiconducting material. Only once this requirement has been met can photo-generated electrons be excited into the conduction band (CB) and subsequently, holes (h^+), be formed in the valence band (VB). The reducing and oxidising ability of these charge carriers are then determined by the positions of the conduction and valance band edges respectively. The position of the edges of these bands are an intrinsic property of each semiconducting material and can also be influenced by certain chemical species (Uchihara *et al.*, 1990)

In a more realistic sense Fox and Dulay (1993) argue that the primary photochemical product are reduced or oxidised species adsorbed on the surface (such as H atoms) which then participate in surface reactions to form the desired secondary photochemical products. It is important to realise that these photo-generated charge can actually be identified as chemical entities adsorbed on the solid surface (Fox & Dulay, 1993).

2.2.2 The "Photo" in Photocatalysis

Electromagnetic radiation or light is integral to the functioning of any photocatalytic system. Fundamentally, the energy of the irradiating light photons must be equal to or greater than E_g of the semiconducting photocatalyst material to drive any desired reaction. An understanding

of how the light spectrum is segmented and in which segment the bulk of the useful energy is located is therefore needed to design and create feasible photocatalytic systems.

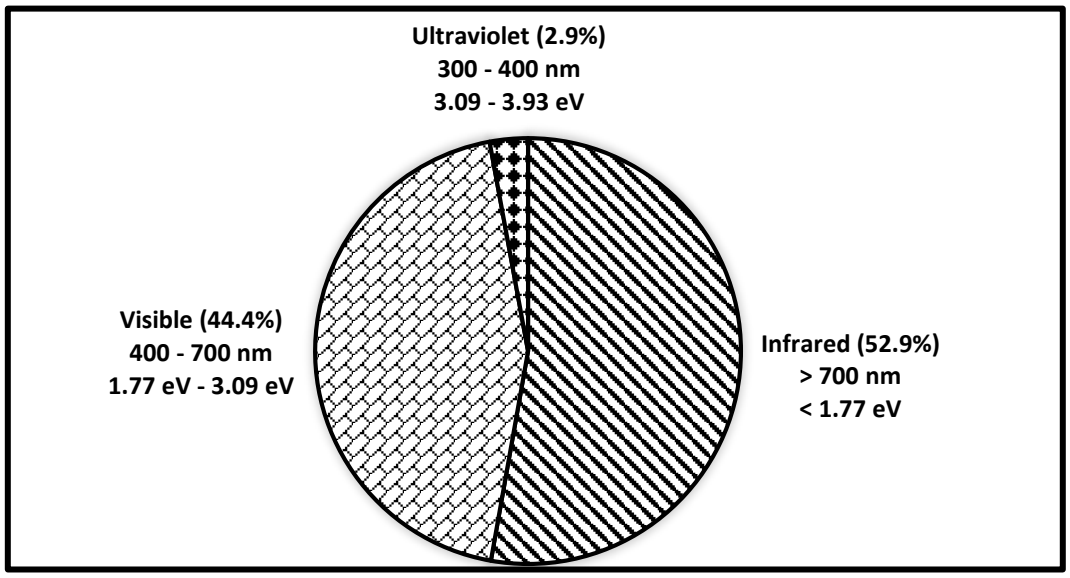

Figure 2. 7: Pie chart showing energy contributions of ultraviolet, visible and infrared irradiation to the solar spectrum adapted from Navarro Yerga *et al.* (2009)

Figure 2. 7 shows that the largest proportion of incoming solar radiation energy is made up of the visible and infrared components with ultra-violet (UV) light only accounting for a mere 2.9%. hence material development is now being directed to be sensitive to components of the spectrum where the bulk of the solar energy is located (Visible and Infrared).

To create an electron & hole pair, using only UV light, a photocatalyst material would need a band gap of approximately 3 - 4 eV. Using only visible light, the photocatalyst would need a bandgap of between 1.77 – 3 eV and so on for the infrared red region as well. The wider the bandgap of the semiconducting photocatalyst the more restricted it is to making use of only high energy photons found in the UV spectrum. Wide band gap semiconductors such as TiO_2 are therefore only able to absorb light in the UV range whilst narrow bandgap semi-conductors such as CdSe, MoS_2 and GaP can make use of UV as well as visible light energy.

It should be noted that Figure 2. 7 represents a simplistic model of the solar spectrum components and that each of the three regions mentioned above can be further sub-divided. Additionally, the contribution of each proportion can also vary quite extensively depending on sky conditions and geographical location (Escobedo *et al.*, 2009).

It is therefore preferable to conduct photocatalytic experiments under consistent illumination conditions, which can be done using artificial lamps such as high-pressure mercury-vapour or xenon lamps. Additionally, solar simulators, which are widely used to test photovoltaic (PV) cells, can provide Air Mass (AM) 1.5 Global (G) illumination which is an approximation of the

most normal incoming solar radiation based on a set of atmospheric conditions and the mass of air (Riordan & Hulstron, 1990).

2.2.3 Material requirements for photocatalytic water splitting

While the type of electromagnetic radiation used to maximise the performance of a photocatalyst is an important aspect for consideration, the, optical, electronic and chemical properties of the photocatalytic material is a domain whereby researchers have much more control in creating a high performing photocatalytic device. Some important functional requirements for effective photocatalytic materials have be outlined in literature (Navarro Yerga *et al*., 2009; Chen, Jaramillo, *et al*., 2010):

1. Ability to absorb visible light energy ($\lambda > 420$ nm)
2. Position of band edge potentials that enables overall water splitting
3. Efficient separation of photo-induced electrons and holes
4. Reduction in energy lost to charge transport and recombination effects
5. Stability of photocatalyst in oxidative or corrosive environments
6. Selectivity for water splitting over self-oxidation reactions

The implications of Figure 2. 7 represents one of the main drivers for the development of visible light active photocatalytic devices. It has therefore been the work of many researchers to find and fabricate photocatalytic materials that maximise light energy harvesting capabilities (Kudo & Miseki, 2009; Ismail & Bahnemann, 2014; Xu, Huang & Zhang, 2016). These efforts include interventions such as band-gap tuning through size confinement effects, creation of Z-scheme photocatalysts, use of co-catalyst materials, dye sensitising and testing of novel materials for photocatalytic activity.

The size of the optical band-gap as well as the positions of the conduction band and valence band edge potentials relative to the potentials of the hydrogen evolution reaction (HER) and oxygen evolution reaction (OER) are a few of the most important parameters for overall photocatalytic water splitting.

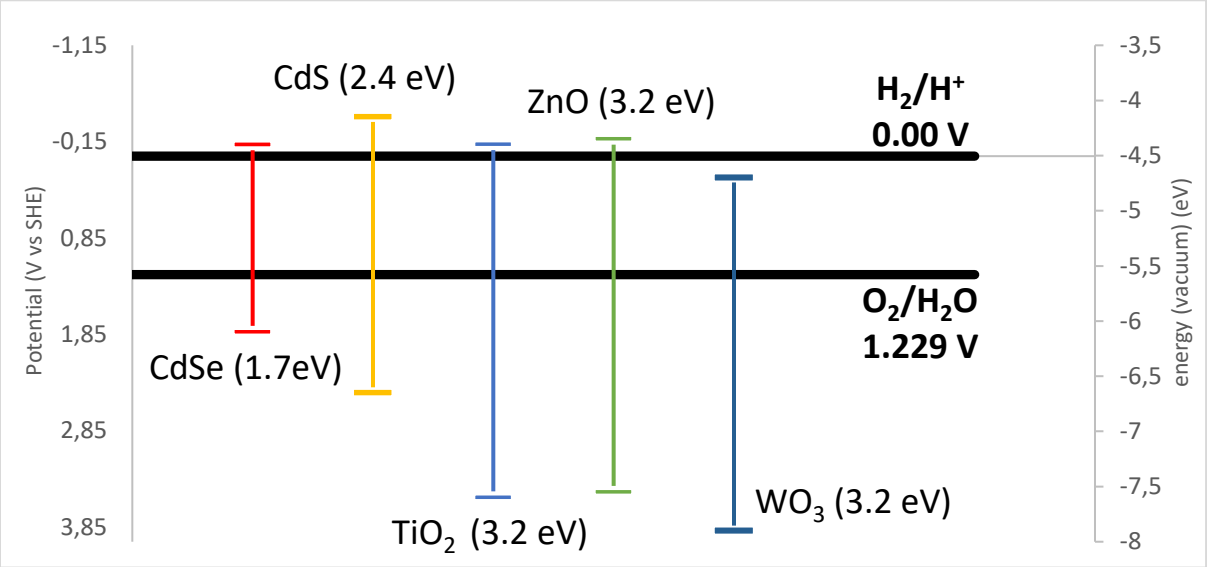

Figure 2. 8: Band gap sizes and edge potentials of five n-type semiconducting materials relative to the energy requirements for the HER and OER. (Adapted from Harriman (1985)*)*

To evolve hydrogen gas, the conduction band potential must be more negative than the potential at which the HER occurs. For oxygen evolution the valance band potential must be more positive than the potential at which the OER reaction occurs. To evolve both gases, both conditions must be simultaneously met by the photocatalytic system used.

As illustrated in Figure 2.8 narrow band gap (CdSe and CdS) as well as wide band-gap (TiO_2 and ZnO) semiconductors have the appropriate electronic structures to split water photocatalytically. Additionally, it should be noted that even if semi-conducting materials have similar bandgap sizes such as TiO_2, ZnO and WO_3., their conduction band and valence band edge positions relative to that of HER and OER determine if the semi-conductor would be a suitable photocatalytic material for overall water splitting or not. In this case TiO_2 and ZnO would be able to drive both reactions but WO_3 would only be able to drive the OER.

HER:	$4H^+ + 4e^- \leftrightarrow 2H_2$	$E°_{cathode} = 0.00\ V\ vs\ SHE$
OER:	$2H_2O \leftrightarrow 4H^+ + 4e^- + O_2$	$E°_{anode} = -1.229\ V\ vs\ SHE$
Overall water splitting:	$2H_2O \leftrightarrow 2H_2 + O_2$	$E°_{cell} = 1.229\ V\ vs\ SHE$

Figure 2. 9: half and overall water splitting reactions at standard conditions

Although these energy requirements are well outlined thermodynamic constraints as shown in Figure 2. 9, the practical energy requirements for photocatalytic water splitting has been estimated to be approximately 0.8 eV wider than the limits shown in Figure 2. 8 (Bolton, 1996). This is mainly due to energy losses caused by an inability of the material to absorb all incident photons, recombination of generated charge carriers and heat production within the material.

Therefore, materials with band gap sizes of approximately 2 eV are more suited for practical water splitting.

2.3: Progress made in photocatalysis

The field of photocatalytic water splitting has gained significant traction since the early 1970s and therefore a few important milestones should be recognized post the Fujishima & Honda, (1972) benchmark.

2.3.1 Artificial photosynthesis

One of the first significant milestones was the idea that photo-induced chemical change could proceed without an applied potential or bias. This was demonstrated by the use of sandwiched semiconductor structures, n-TiO_2/GaP (Nozik, 1977) for water decomposition independently of an external potential. This idea was further re-enforced when platinised(Pt) and metal-free $SrTiO_3$ crystals, another prominent photocatalyst material, was used for photoproduction of H_2 gas (Wagner & Somorjai, 1980). This was significant because it differentiates the technology as being inorganically analogous to photosynthesis, an observation made in the early stages (Nozik, 1977). Today, the term "artificial photosynthesis" is more predominately used to describe chemical change brought about using purely light energy via the use of engineered photocatalytic materials ("Artificial Photosynthesis: Solar Splitting of Water to Hydrogen and Oxygen", n.d.; Mubeen *et al.*, 2013; Ager *et al.*, 2015; Montoya *et al.*, 2016).

2.3.2 Development of UV-light sensitive photocatalysts.

Most of the progress made thus far in the field has been in the development and discovery of novel photocatalytic materials. UV-light sensitive materials ($E_g > 3$ eV) are mainly classified on the basis of their electronic configurations into four main groupings (Ismail & Bahnemann, 2014):

1) d^0 metal oxides (Ti^{4+},Zr^{4+}, Nb^{5+}, Ta^{5+}, W^{6+}, and Mo^{6+})

2) d^{10} metal oxides (In^{3+}, Ga^{3+}, Ge^{4+}, Sn^{4+}, and Sb^{5+})

3) f^0 metal oxides (Ce^{4+})

4) Non- oxides

A look at review articles such as that presented by Kudo & Miseki (2009) quickly shows that about 70 different UV-light active photocatalyst materials were developed and tested from the mid-1980s to the early 2000s for the d^0 metal oxide group alone. Of this group one of the best

performing photocatalysts was a La-doped $NaTaO_3$ perovskite with co-catalyst NiO. This system exhibited activities for H_2 and O_2 and evolution rates of 19 800 and 9 700 $\mu mol.h^{-1}$ respectively with high quantum efficiencies in pure water (Kudo & Kato, 2000; Kato, Asakura & Kudo, 2003).

Some more notable examples of UV-light active photocatalysts for pure water splitting include: $Sr_2KTa_5O_{15}$ with NiO_x as a co-catalyst material (Wang, Schwertmann, *et al.*, 2014) as well as GaN nanowires using Rh/Cr_2O_3 in a core-shell structure as a co-catalyst material (Kibria *et al.*, 2014). Examples of photocatalysts for hydrogen production from electrolytes with organic compounds include: TiO_2 with Au-Pd core-shell structures as co-catalyst for hydrogen evolution from a 25 v% glycerol solution (Su *et al.*, 2014) as well as carbon nanotubes(CNTs)-Ta_2O_5 co-catalysed with Pt for hydrogen evolution from a 50 v% methanol solution (Cherevan *et al.*, 2014). Many more such photocatalyst systems are well reviewed in the literature (Li *et al.*, 2015).

2.3.3 Development of visible light sensitive photocatalysts

The realisation that a completely efficient UV-light (up to 400 nm) active photocatalyst material can only practically effect a 2% solar energy conversion has resulted in the need to develop visible light (up to 600 nm) active photocatalyst materials where a maximum theoretical 16% solar energy conversion can be achieved (Abe, 2010). This is critical if H_2 production is to be achieved at a large economical scale. The harnessing of visible light has been reported to occur using one of two approaches, Z-scheme photocatalyst systems or the use of a single visible-light active photocatalyst (Ismail & Bahnemann, 2014).

2.3.3.1: Z-Scheme photocatalyst systems

Z-scheme photocatalyst systems generally have three components, a photocatalyst for the HER, a photocatalyst for the OER and an electron mediator present in the electrolyte or testing solution. The Z-scheme configuration is advantageous because it allows recombination of photogenerated electrons from the OER photocatalyst to recombine with the photogenerated holes in the HER photocatalyst via the redox mediator as shown in Figure 2. 10. This allows for the efficient separation of charge in the system, such that the electrons and holes with higher reducing and oxidising power respectively participate in the surface reactions.

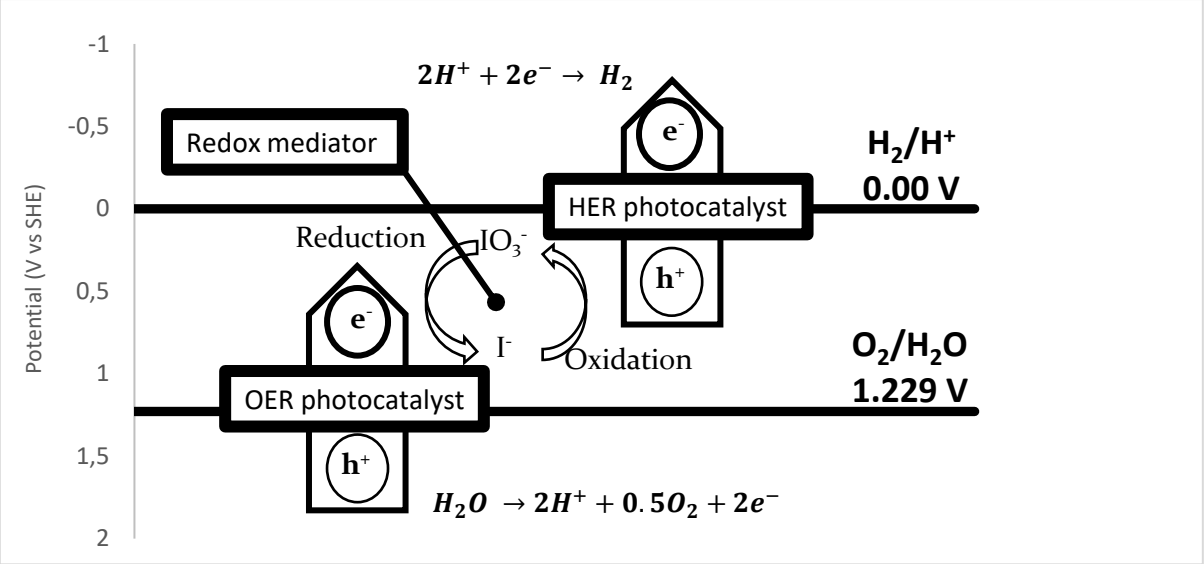

Figure 2. 10: Z-scheme photocatalyst system

Additionally, having separate HER and OER photocatalysts allows for separate gas evolution sites preventing any surface back reactions from occurring (Li *et al.*, 2015) Drawbacks of this system, however, are that they are more complicated than single material photocatalysts and also that twice the amount of photons are needed to drive water decomposition due to the presence of an HER and OER photocatalyst.

One example of a prominent liquid Z-scheme system was the use of Pt/WO_3 and $Pt/ZrO_2/TaON$ as OER and HER photocatalyst respectively with IO_3^-/I^- as the electron mediator (Maeda *et al.*, 2010). This system achieved stoichiometric H_2 and O_2 evolution using visible light without the use of sacrificial reagents. Also, of interest have been solid state Z-scheme systems when Tada *et al.* (2006) initially presented a highly active $CdS/Au/TiO_2$ Z-scheme system with Au used to connect CdS and TiO_2 for HER and OER respectively. Another example using a novel material such as reduced graphene oxide (RGO) functioning as a solid redox mediator with $BiVO_4$ for OER and $Ru/SrTiO_3$:Rh HER showed significant improvement in the transfer of photoexcited electrons within the system under visible light illumination (Iwase *et al.*, 2011).

2.3.3.2: Visible-light active photocatalysts

The availability of photocatalyst materials, with large enough band-gaps to meet the thermodynamic requirements of water splitting and small enough to harvest visible light as well as possesses the correct band-edge positions for overall water splitting, are very limited. One of the only compounds to comfortably meet these requirements and as a result has been extensively studied (Ismail *et al.*, 2009) is CdS (2.4 eV) but it is adversely affected by anodic photo-corrosion leading to its deactivation (Meissner *et al.*, 1986). Many metal sulphides are

active are active in visible light but require additional sacrificial reagents to supress photo-corrosion.

More stable oxide photocatalyst materials modified with co-catalysts, dopants as well as dyes are generally found to be active under visible light conditions for either HER or OER but rarely both. The development of these reaction selective photocatalysts however is not a waste since they can form part of Z-scheme systems (Kudo & Miseki, 2009). A few examples of these photocatalyst include, for OER, WO_3 (Erbs *et al.*, 1984), Bi_2MoO_6 (Shimodaira *et al.*, 2006), $Na_{0.5}Bi_{1.5}VMoO_8$ (Yao & Ye, 2008) and for HER, $SrTiO_3$:Cr/Sb (Kato & Kudo, 2002) and $La_2Ti_2O_7$:Cr (Hwang *et al.*, 2004).

2.4: Cadmium Selenide

CdSe is an n-type semiconductor with a direct, bulk band gap of approximately 1.7 eV. Its narrow band-gap allows for the absorption of a larger proportion of solar energy as can be inferred from Figure 2. 7 and is therefore an interesting material for use a s visible light active photocatalyst for the application of water splitting.

For the case of 1.4 nm thick CdSe nanoribbons, Joo *et al.* (2006) found, using UV-Vis absorption and photoluminescence spectroscopy, that these nanostructures showed extended bandgap sizes of approximately 2.74 eV. This result was understood to be the effects of quantum confinement or size confinement effects of the material. This observation was corroborated by Andrew Frame *et al.*(2008) who also synthesised CdSe nanoribbons of similar size and tested their photocatalytic performance by irradiating them with UV and visible light in an aqueous solution of Na_2S/Na_2SO_3. They confirmed the implications of what Joo *et al.* (2006) reported relating to the extended band gap and showed that this size confinement effect can establish catalytic properties in materials that did not have this property in their bulk form.

The effect of quantum confinement on the photocatalytic activity has also been reported for other materials, including CdS (Yanagida *et al.*, 1995) and WO3 (Tanaka, Oaki & Imai, 2010). This highlights a key effect of nano-sized materials on photocatalytic properties that makes available a much wider range of options to consider for use as effective photocatalysts.

Since the feasibility of CdSe as a photocatalyst for hydrogen production has been established, many different nano-forms of this material has been tried and tested. The most extensively tested forms of CdSe have been zero-dimensional structures such as quantum dots (QDs) or nano-particles (Lin *et al.*, 2010) This has been the case particularly with respect to how changes in their size affect their bandgap (Holmes, Townsend & Osterloh, 2012; Zhao, Holmes &

Osterloh, 2013). Zero dimensional CdSe nanoforms have also been used extensively as a co-catalyst material that functions as a sensitizer for visible light in more complex, multi-component photocatalytic materials (Kim *et al.*, 2011; Sreedhar *et al.*, 2015; Zhang *et al.*, 2015).

Unlike zero-dimensional CdSe, one dimensional structures have been less systematically investigated. These One-dimensional CdSe nanostructures include structures such as nanorods, nanoribbons, nanobelts and the focus of this research, nanowires. Nanowire structures have been reported to be between a few nm to a few 100 nm in diameter (Hurst *et al.*, 2006) and are often a few μm in length. This characteristic high aspect ratio of one-dimensional materials makes them interesting to study for applications in heterogenous photocatalysis such as clean hydrogen production, giving these materials large surface areas.

Nanoribbons synthesised using low temperature wet chemical methods by Andrew Frame *et al.* (2008), were tested for hydrogen production by irradiation with UV and visible light. The nanoribbons were suspended in three different aqueous solutions, pure water, a 20 % methanol solution and a 0.1 M aqueous Na_2SO_3/Na_2S. These additives were used as sacrificial electron donors which help prevent self-oxidation of the photocatalyst material. The hydrogen evolution rate in pure water (0.92 $\mu mol.h^{-1}$) was found to be the lowest, while the evolution rate in the 0.1 M aqueous Na_2SO_3/Na_2S solution performed the best (107 $\mu mol.h^{-1}$). This was attributed to an increase in the number of trapped electrons brought about by the presence of the sacrificial electron donors. Despite, making use of Na_2SO_3/Na_2S, the CdSe nanoribbons still showed evidence of photo-decomposition confirmed by the increased concentration of Cd^{2+} ions in the solution, the colour change from yellow to orange as well as transmission electron microscopy (TEM) characterizations done after 5 hours of testing showing degraded nanoribbon morphology.

This study illustrated that although this material is UV and visible light sensitive and has an extended bandgap, that it is still very challenging to appreciably produce hydrogen from aqueous solutions as shown by the very slow evolution rate. It also illustrates that these CdSe structures are not very stable and undergo photo-corrosion. other researchers have also reported on this observation (Mubeen *et al.*, 2013; Fawzy, 2016).

Nanowires specifically have a range of possible synthetic routes which can be more broadly classified as either top-down methods or bottom-up. These include vapour-liquid-solid (VLS), solution-liquid-solid, supercritical fluid-liquid solid (SFLS), chemical vapour deposition (CVD), laser ablation, metal-organic chemical vapour deposition (MOCVD), and chemical/molecular beam epitaxy (CBE) (Banerjee, Dan& Chakravorty, 2002; Fortuna & Li, 2010). The method that

will be the focus of this dissertation however, is rooted in electrochemistry and is a template directed electrodeposition technique.

2.5: Template Directed Electrodeposition of CdSe

The template directed electrodeposition technique for nanowire synthesis involves the deposition of reducible materials such as metals or polymers from an electrolyte solution into the nano or micro sized pores of a template. The growth starts at the bottom of the pores, where a conducting substrate is placed, where nucleation of the deposited material occurs perpendicularly toward the other end of the pore with the nanowires taking on the dimensions of the pores they grow in.

The mechanism for the formation of CdSe in dilute H_2SO_4 from selenious acid and $CdSO_4$ has been proposed by Skyllas Kazacos and Miller (1980) and is shown in Figure 2. 11.

$$H_2SeO_3 + 6H^+ + 6e^- \rightarrow H_2Se + 3H_2O$$

$$2H_2Se + H_2SeO_3 \rightarrow 3Se + 3H_2O$$

$$H_2Se + Cd^{2+} \rightarrow CdSe + 2H^+$$

Figure 2. 11: Mechanism for the formation of CdSe in acidic electrolytes (Laboratories & Hill, 1980)

The cathodic co-deposition of Cd and Se however was found to be intrinsically richer in Se a result of competing reactions. In an effort to eliminate this problem and form more even ratios between Cd and Se, Kressin *et al.*, (1991) proposed an electrodeposition technique whereby the potential is swept or cycled between two potential limits to synthesise stoichiometric CdSe films. This technique was then carried forward for the synthesis of CdSe nanowires using a porous template.

One of the earliest attempts contributing to how nanowires are electrodeposited into templates today was by Possin (1970), who electrochemically synthesised Sn, In and Zn nanowires inside the pores of Mica with dimensions of approximately 40 nm in diameter an 15 µm in length. Klein *et al.* (1993), then combined Possin's porous template technique with the cyclic electrodeposition technique developed by Kressin *et al.* (1991) to deposit CdSe and CdTe based microdiode arrays into the pores of alumina membranes. Their justification for using this method instead of the other more elegant precipitation techniques was that it allowed for a more precise control over the physical dimensions as well as the composition of the resulting semiconducting materials. They carried out the electrodeposition using $CdSO_4$ and SeO_2 as Cd and Se precursors and using Au, Ni and Ag layers as the conductive substrate.

Pena *et al.* (2002) built on this and constructed CdSe based heterojunction nanowires that consisted of Au-CdSe-Au segments. This structure was deposited by cycling or sweeping the potential back and forth using anodised aluminium oxide as the template in an acidic medium. To obtain a stoichiometric ratio of Cd to Se in the nanowires Peña *et al.*(2002) varied the concentration of SeO_2 while keeping the concentration of $CdSO_4$ constant at 0.30 M in the electrolyte. This was to determine the optimum Cd/Se ratio in the electrolyte.

In contrast to Peña *et al.* (2002), Peng *et al.* (2001), who also synthesised CdSe nanowires but used direct current (dc) electrodeposition in an alkaline medium claimed that the ratio of Cd to Se in the nanowires is dependent on the pH, having varied the pH of the deposition bath keeping all other parameters constant. They claimed that the co- deposition of Cd and Se is easier under alkaline conditions pH ≈ 9. Aside from Peng *et al.* (2001), there have been no other studies found that specifically looked at the effect of pH on CdSe nanowire stoichiometry as most nanowire growth is done using acidic deposition baths.

In addition to Peng, direct current electrodeposition of CdSe has been used successfully in other studies Xu *et al.*(2000) employed dc electrodeposition in non-aqueous electrolytes whereas (Yu-Zhang *et al.*, 2008) employed dc electrodeposition in acidic aqueous electrolytes very similar to that used by Kressin *et al.*(1991), Klein *et al.*(1993) and Peña *et al*, (2002).

Although all these studies had produced, on average stoichiometric ratios between Cd and Se. Methods employed using DC electrodeposition were conducted under a variety of different conditions with no consistent set of conditions that yielded comparable results. This was not the case for cyclic electrodeposition studies where a consistent set of conditions such as concentration, Ph, and temperature was used, and all produced near stoichiometric results.

A drawback of this method however, is that the effect of mass transfer phenomena on stoichiometry is not well understood or accounted for in the reported literature. Consequently, many studies report 1:1 ratios between Cd:Se but these are mostly 'on average' values and can vary quite easily from one batch to the next.

The advantages of the template directed technique, regardless of how the potential wave is applied, is that it allows one to synthesise various materials in a facile manner, provided they come in easily reducible forms soluble in aqueous solutions. Furthermore, it allows for the combination of these various materials to be synthesised within the same substrate, this is a major advantage since the development of functional multi-component photocatalytic materials is gaining traction (Hurst *et al.*, 2006). Additionally, the experimental conditions are

mild, occurring mostly at ambient conditions and fine control over the resulting materials dimensions is possible.

2.6: Fabrication of multi-component photocatalytic devices

A photocatalytic device is referred to as a composite material made up of a variety of different functional materials to help improve photocatalytic performance. These materials can vary in their functionality and include but is not limited to improving charge separation via the formation of ohmic and Schottky junctions, electron trapping, corrosion resistance, promotion of electrochemical surface reactions, mechanical stability and sensitisation to visible light. The core of any such device is the semiconducting or light harvesting material without which, it cannot be called a photocatalyst or photocatalytic device.

With regard to performance, efficient use of absorbed photons is still regarded as one of the biggest challenges for visible light sensitive photocatalyst materials (Lee, 2005) and various strategies have been used to improve this efficiency. These efforts include cation and anion doping of wide band gap semiconductors, creating new single phase materials with band gaps ideal for water splitting (1.23 eV – 3 eV) as well as constructing multi-component materials comprised of a semiconductor for suitable for reduction and one suitable for oxidation (Lee, 2005) or combining an overall water splitting semiconductor with metallic co-catalysts such as Ni, Au and Pt to improve charge separation and efficiency (Pena *et al.*, 2002; Mubeen *et al.*, 2013).

More recently, the previously described electrodeposition technique has been a method to construct scalable, stable, and inexpensive multi-component photocatalytic devices. Building on the construction concept by Pena *et al.* (2002), Mubeen *et al.* (2013) synthesised multi-segmented nanowires consisting of a transparent polymer OER electrocatalyst poly(3,4-ethylenedioxythiophene) poly(styrenesulfonate) (PEDOT:PSS), CdSe as a visible light absorbing semiconductor, and Pt as a reduction electrocatalyst. Additionally, an ohmic contact (Ni-Au) is also used between the CdSe and Pt segments to enhance charge separation. These multi-segmented nanowires remained embedded inside the AAO membrane to increase mechanical stability and provide protection against corrosion effects.

2.6.1 Design and performance of multi-segmented nanowires

The design of the hetero-structure presented by Mubeen *et al.* (2013) is such that the light absorbing material (CdSe) is isolated from the electrolyte but can still absorb light due to the use of a transparent polymer OER electrocatalysts PEDOT:PSS and the translucent nature of

the AAO in solution. This is to reduce occurrence of photodegradation The CdSe is protected both by the polymer and the AAO template.

When light with the correct energy strikes the photoactive semiconducting material (CdSe) an electron-hole pair is formed. Ideally the electron moves towards the cathode and participates in the reduction of hydrogen, while the positive holes move toward the anode electrocatalyst and oxidises the sacrificial electron donors or for oxygen evolution. Co-catalysts help to facilitate this separation of charge (Yang *et al.*, 2012). Pt, Ni, Au and PEDOT:PSS are co-catalyst to CdSe and carry out important functions that enable the photocatalyst device as a whole to perform efficiently and remain stable. Platinum is well known to be the best material for hydrogen evolution due to its moderate adsorption and low desorption energies to and from its surface (Ojha *et al.*, 2016). Nickel and Gold due to their excellent conductive properties are ohmic contacts between the light absorber and Pt cathode (Mubeen *et al.*, 2013) and allow electrons to easily reach the reduction process. PEDOT:PSS has the dual purpose of being the Schottky contact, which absorbs holes as well as an anode electrocatalyst for the OER.

The heterostructures were tested by the photo-electrolysis of HI with KI used as a sacrificial reagent in a highly corrosive environment to illustrate the stability of the structure. This resulted in a performance of 40 μmol/hr of hydrogen production with a quantum efficiency of 7.4 %. The photocatalysts were stable for more than 24 hours indicating that the protective mechanisms of this heterostructure worked quite well considering that they were tested in a highly acidic medium.

2.6.2 PEDOT:PSS as an OER electrocatalyst

Cadmium chalcogenides (CdX, X = S, Se, Te etc.) have been noted for having ideal band-gap sizes and band edge positions to enable overall water splitting but are unstable due to photo-oxidation of the semi-conducting material itself (Andrew Frame *et al.*, 2008; Xu, Huang & Zhang, 2016). Although the use of sacrificial electron donors has been used to minimise photo-oxidation of the photocatalyst, another route of minimisation has been to incorporate novel co-catalyst materials into the photocatalytic device structure.

A very useful conductive and transparent polymer currently being studied extensively, and that's molecular structure is shown below in Figure 2. 12 is poly(3,4-ethylenedioxythiophene) poly (styrene sulfonic acid) (PEDOT:PSS.). This material has been in development in response to an increasing need for highly conductive, transparent, and more easily processed electrodes that are less costly than ITO substrates (Sun *et al.*, 2015).

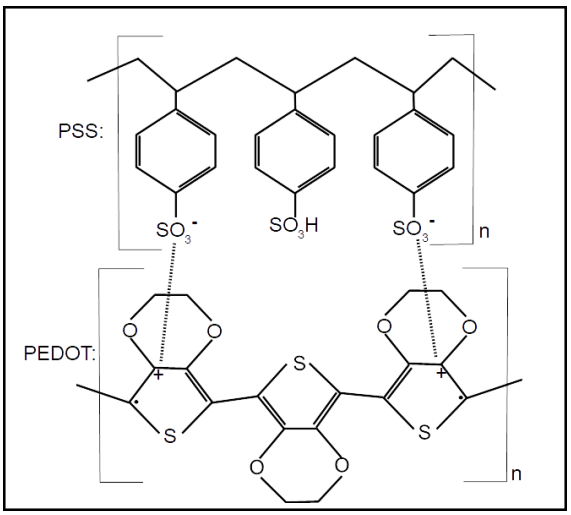

Figure 2. 12: Molecular structure of conducting polymer PEDOT:PSS (adapted from Sun *et al.* (2015)*)*

PEDOT:PSS has been used as co-catalyst material in conjunction with CdSe/TiO_2 nanotube arrays (Chong, Zhu & Hou, 2017), ZnO nanorods (Dhar *et al.*, 2018), CdSe multi-segmented nanowires (Mubeen *et al.*, 2013) as well as Si based solar cells (Jäckle *et al.*, 2017). The incorporation of PEDOT:PSS into these systems was fundamentally to absorb and transfer photogenerated holes from the semi-conductor material. What is symptomatic of this, is extended photocatalyst life times and improved photocurrent stability. For CdSe systems specifically, PEDOT:PSS has been described as a physical passivation layer as well (Chong, Zhu & Hou, 2017), which is also important for the prevention of Cd^{2+} ions leaching into solution.

2.6.2.1: Post treatment of PEDOT: PSS thin films

Although as prepared PEDOT:PSS films are poor conductors for electrode use, with conductivities of less than 1 S/cm being stated (Yu *et al.*, 2016), further treatment of these films have been found to dramatically increase their conductivity. Through treatments with various concentrations, up to 1.5 M H_2SO_4, at elevated temperatures of 160 °C Xia, Sun and Ouyang (2012) attained a maximum conductivity of 3065 S/cm. Treatment of PEDOT:PSS films with various mild and weak organic acids has also been systematically shown to increase the conductivity from 450 S/cm to 2870 S/cm using acetic acid and methanesulfonic acid respectively (Ouyang, 2013). treatments with acetic acid and ethylene glycol can also be used to

alter the solubility of film (Mubeen *et al.*, 2013). In addition to chemical treatments, thermal treatment is also used to improve film quality and stability.

2.7: Photocatalytic testing for hydrogen evolution

Testing of photocatalyst materials in the field of heterogenous photocatalysis has been said to lack proper methodologies that allow for a fair basis of comparison between photocatalytic testing results (Chen, Jaramillo, *et al.*, 2010; Döscher *et al.*, 2016; Qureshi & Takanabe, 2017). Recently efforts have been made to address inconsistent reporting protocols by precisely defining these performance criteria for the case of planar photocatalytic systems for hydrogen production specifically, using single band-gap materials (Chen, Jaramillo, *et al.*, 2010). Even more recently, definitions of performance for photocatalytic powder systems (Qureshi & Takanabe, 2017) has been reported on in an effort to address this problem within the field of heterogenous photocatalysis.

It should be noted that the needs within commercial photoreactor design are very different from the needs of photoreactor design for fundamental research. The former needing maximisation of performance at the cheapest cost whereas the latter depends on what properties of the photocatalyst are being tested. This is most evident when materials of construction are chosen. For commercial processes UV-transmittance of materials would be desired as it would increase the photocatalytic performance. But this would be undesired for research purposes if the aim is to test visible light activity. This section refers to photocatalytic testing under laboratory conditions.

2.7.1 Performance parameters for photocatalytic water splitting

Growth in the field of photocatalysis has been exponential since the 1970s, the current growth and direction of that growth, however, is limited by a lack of standardised reporting guidelines regarding the photocatalytic efficiency as well as stability (Ager *et al.*, 2015). This has made it quite impossible for research efforts across different laboratories to be compared. A few attempts at defining reporting protocols for photocatalytic water splitting have been done, most notably for photoelectrochemical (PEC) water splitting systems for single bandgap, planar, materials.

2.7.1.1: Solar-to-Hydrogen Efficiency (STH)

The solar-to-hydrogen (STH) efficiency which is described by Chen *et al.* (2010) as a "benchmark efficiency", is defined as the amount of chemical energy obtained through the production of

hydrogen divided by the total incident solar energy on the photocatalytic system and is given by the following equation:

$$STH = \left[\frac{(mmol\ H_2.s^{-1}) \times (237\ kJ/mol)}{P_{total}(mW.cm^{-2}) \times Area\ (cm^2)}\right]_{AM\ 1.5\ G}$$

In the numerator, the hydrogen flow rate, which has ubiquitously been obtained using gas chromatography (Andrew Frame *et al.*, 2008; Holmes, Townsend & Osterloh, 2012; Mubeen *et al.*, 2013; Zhang *et al.*, 2015) is multiplied by the standard state free energy change (ΔG^0) for hydrogen production from water decomposition. In the denominator the incident irradiance (P_{total}) is multiplied by the illuminated photocatalytic area. This area is much more easily defined for immobilised photocatalytic systems than suspension-based systems.

This efficiency can only be reported provided that the aforementioned parameters were obtained under the following conditions emphasised by Chen *et al.*(2010):

1. The light source matches Air Mass 1.5 Global (AM 1.5 G) characteristics.
2. For photoelectrochemical systems, there is no applied bias between the working electrode and counter electrode.
3. For photoelectrochemical systems, the working electrode and counter electrode must be kept in the same compartment such that the pH is the same for both electrodes to eliminate any chemical bias.
4. The electrolyte may not contain any sacrificial electron donors or acceptors that will promote hydrogen or oxygen evolution redox reactions.
5. Stoichiometric evolution of H_2 and O_2 must be observed.

Reporting a STH efficiency is not a trivial task but is a critical parameter for comparing the performance of photocatalytic systems for hydrogen production from water splitting. It should also be noted that an analogous efficiency can be calculated for other photocatalytic reactions such as the reduction of CO_2 to other solar fuels, provided the thermodynamics of those reactions are taken into account (Qureshi & Takanabe, 2017).

2.7.1.2: Quantum Efficiency (QE)

Alongside the STH, the quantum efficiency is described as a material diagnostic efficiency by Chen *et al.* (2010) as opposed to a benchmarking efficiency used for comparison. QE is defined

slightly differently depending on if it is being calculated for a photoelectrochemical system vs a photocatalyst suspension system.

The photoelectrochemical community splits QE up into two separate efficiencies, the external quantum efficiency (EQE) or equally the incident photon-to-current efficiency (IPCE) and the internal quantum efficiency (IQE) which can be defined as follows:

$$EQE = IPCE = \frac{Reacting\ electrons\ produced}{Photon\ flux\ (\boldsymbol{incident})}$$

$$IQE = \frac{Reacting\ electrons\ produced}{Photon\ flux\ (\boldsymbol{absorbed})}$$

For photocatalytic suspension systems (Qureshi & Takanabe, 2017) the QE is defined as:

$$QE = \frac{rate\ of\ chemical\ change}{Photo\ flux\ (\boldsymbol{absorbed})}$$

Regardless of the system configuration, the QE is essentially a measure of how many photons (incident or absorbed) yield useful electrons that can participate in the redox surface reactions. This translates to how effective the photocatalytic material is at harvesting light energy.

2.7.1.3: Stability

The stability criterion for photocatalytic systems (PEC or photocatalytic suspensions) is not formally defined. Most research efforts simply report a period of time where the photocurrent or hydrogen (or oxygen) evolution rate is stable (Ager *et al.*, 2015). Even though this is sensible, there are no known existing standard conditions for how these parameters should be measured i.e. left continuously under illumination until a decline in photocurrent or hydrogen evolution rates is observed or if the testing electrolyte can be changed after a set period of time or if there is a set tolerance in the observed performance drop before instability can be concluded.

2.7.2 Mode of testing

Testing of photocatalytic materials for hydrogen production has typically been carried out in two main modes related to the mobility of the catalytic material relative to the testing electrolyte. These include irradiated suspensions or immobilised photocatalyst materials with some examples being shown in Table 2. 1. Additionally, immobilised photocatalyst materials can also be used as a photoelectrodes and integrated into a three electrode type electrochemical cell. This configuration allows for the photoelectrochemical characterisation of photocatalyst

materials with regard to its photocurrent density vs an applied potential bias (Kim *et al.*, 2011; Guo *et al.*, 2016).

Table 2. 1 List of various photocatalytic materials being tested in either a suspension or as an immobilized photocatalyst.

Photocatalytic material	**Suspension /Immobilised**	**Photocatalytic /Photoelectrochemical**	**Reference**
$La_5Ti_2CuS_5O_7$/$BiVO_4$	Both	Photocatalytic	(Sun *et al.*, in press)
$SrTiO_3$	Immobilised	Photocatalytic	(Goto *et al.*, 2017)
CdSe & CdS	Suspension	Photocatalytic	(Uchihara *et al.*, 1990)
TiO_2	Immobilised	Photoelectrochemical	(Fujishima & Honda, 1972)
CdS	Suspension	Photocatalytic	(Sahu, Upadhyay & Sinha, 2009)
CdSe QDs / $SrTiO_3$	Immobilised	Photoelectrochemical	(Sreedhar *et al.*, 2015)
Fe_3O_4	Suspension	Photocatalytic	(Mangrulkar *et al.*, 2012)
CdSe	Immobilised/Suspension	Photocatalytic	(Mubeen *et al.*, 2013)

2.7.2.1: Aqueous suspensions photocatalysts

Aqueous suspensions involve the irradiation of photocatalytic particles suspended in the desired testing electrolyte. Evolved gases then enter the vapour space above the suspension and can be collected to determine photocatalytic performance. Although these systems are generally simple in design and low cost, a few drawbacks are that H_2 and O_2 are evolved into the same space which is both a health and safety hazard as well as requiring further downstream processing to separate these gases (Fabian *et al.*, 2015).Furthermore the interaction of light with a suspension of randomly moving particles as well as other elements in the system such as the presence of bubbles makes it challenging to understand and model the how light is scattered within the system and what effect this has on the photocatalytic performance (Motegh, 2013).

2.7.2.2: Immobilized photocatalysts

Immobilised photocatalyst consist mostly of planar systems with photocatalyst particles immobilised on a surface as a film where they can be irradiated. The advantages of this are that oxidation and reduction type photocatalysts can be physically separated allowing the separation of evolved gases It also allows that the illuminated area becomes a lot better defined and light distribution can be modelled more easily as opposed to the random motion of particles. The disadvantage of this method is that it generally requires more complicated testing set-ups, compared to particle suspensions.

The mode in which the photocatalytic material will be tested is one of the main considerations for when designing a suitable photoreactor.(Bouchy & Zahraa, 2003). Additional considerations included: The choice of sacrificial regent usage (Sabate *et al.*, 1990; Andrew Frame *et al.*, 2008), Source of irradiation, measurement methodology as well as materials of construction for the photoreactor.

2.7.3 Sacrificial Reagents

Sacrificial reagents are non-catalytic chemical additives, added to the electrolyte being tested such that they improve photocatalytic performance by minimising recombination rates (Commentary, 2013). The first type of sacrificial reagents are hole scavengers or electron donors which quench photogenerated holes within the photocatalytic device and are consequently oxidised. The second type are electron scavengers which remove photogenerated electrons and are themselves reduced. The main purpose of using these reagents is to introduce a competing reaction that favours the production of the desired product.

2.7.3.1: Sacrificial reagents for hydrogen evolution.

Hole scavengers are the dominant sacrificial reagent type used for the photocatalytic production of hydrogen because electrons are required for the evolution of hydrogen. The most common inorganic hole scavengers are aqueous solutions of Na_2SO_3 and Na_2S either used separately or combined. While the most common organic hole scavengers include solutions of MeOH, Ethylenediaminetetraacetic acid (EDTA) as well as various other alcohols and hydrocarbons (Commentary, 2013).

In order of increasing performance, Joo *et al.* (2006) tested CdSe nanoribbons in pure H_2O, a 20 % MeOH solution and a 0.1 M Na_2SO_3/0.11 M Na_2S solution under UV and visible light. The use of a sacrificial electron donor here resulted in increased hydrogen evolution due to the suppression of the recombination dynamics as well as a decrease in the rate of photo-corrosion as was evident from the lower concentration of Cd^{2+} ions in the testing electrolyte. A flaw in the

interpretation of the H_2 evolution rate here however, for the MeOH solution, is that oxidation of methanol also produces hydrogen as can be seen from the equation below:

$$CH_3OH\ (l) + H_2O\ (l) \rightarrow CO_2\ (g) + 3H_2\ (g)$$

This means that hydrogen is being produced in two photocatalytic reactions instead of just one (Commentary, 2013) and should not be counted towards the activity reported or at least acknowledged as a part of the combined reported activity.

Many researchers have reported these increases in photocatalytic activity and stability upon using hole scavengers. Wu *et al.* (2014) indicates that the choice of hole scavenger strongly influences the QE of the photocatalytic device and that the transfer of photogenerated holes is a key efficiency limiting step for the case of CdS-Pt and CdSe/CdSe-Pt nanorods. In a similar system of Pt decorated CdS nanorods, Berr *et al.* (2012) found that their photocatalytic system was more stable and efficient the higher the redox potential of hole scavenger was. Mubeen *et al.* (2013) carried out the photocatalytic production of hydrogen by suspending CdSe based segmented nanowire devices, in 0.1 M KI acidified with HCl to a pH of 2, his aim was to demonstrate the stability of his devices (> 24 hours) to produce hydrogen with a kinetically less challenging redox reaction than water splitting. The use of KI and HCL as a testing electrolyte in their study however, without any mechanistic detail or comparison to more commonly studied systems was found to be quite arbitrary.

The enhancement effects of the use of hole scavengers be for the photocatalytic production of hydrogen has been well studied and will play a key role at making processes more efficient for larger scale hydrogen production. It should however be recalled that for the reporting of a STH benchmark efficiency, these reagents cannot be used, but this does then imply that this reported efficiency is then minimum performance expectation for any particular photocatalytic system.

2.7.4 Evolved gas measuring system

A challenging aspect in determining photocatalytic performance is being able to accurately measure the rate of the gases evolved when they are only evolved at a rate of a few 100 μmol per hour, if that. This has been quite an understated and underdiscussed practicality in the literature looked at. What is more is that gas chromatography has been the go to method for the quantification of these evolved gases with virtually no exploration in the use of other methods such as mass spectrometry (M.S.). Chen *et al.* (2010) briefly refers to the use of an M.S for the analytical determination of a true hydrogen production rate but provides no further details regarding its use.

2.8: Chapter Conclusion

This chapter has provided an overview of the relevant aspects leading up to and involved in the photocatalytic production of hydrogen gas. The field as a whole is still relatively new, and can is still currently in the midst of rapid expansion particularly with regard to the development of novel materials as photocatalysts.

In parallel to this, there are also a lot of opportunities for further exploration. This includes from a materials development point of view: Continued investigation into small band-gap semiconductors such as CdSe with the aim of increasing its resistance to photo-decomposition; Employing the template directed electrodeposition technique, which is a relatively simple, fast and low-cost technique to produce more stoichiometric electrodeposits; Testing the performance of multi-segmented nanowires such as those presented by Mubeen *et al*. (2013) in different testing electrolytes and including different co-catalyst materials into the nanowire heterostructure.

From a testing point of view, the development and description of a testing system that firstly, allows for the accurate reporting of STH efficiencies as defined by Chen *et al*. (2010) and secondly makes use of an alternative analytical technique such as mass spectrometry for the quantification of photocatalytically evolved gases.

Chapter 3: Study Objectives

Based on the insights obtained from literature, and with the intention of building on previous work conducted at the University of Cape Town on the synthesis of functional nanowires (Fawzy, 2016), the work presented by Mubeen *et al.* (2013) is of particular interest for use as a foundation from which further developments can be made. This includes exploring differently sized nanowire diameters and testing devices in more commonly reported testing electrolytes such as MeOH solutions.

In addition to this, it is of interest for establishment of photocatalytic research at UCT to design a system that allows for the proper reporting of photocatalytic performance as outlined by Chen *et al.* (2010) &; Qureshi & Takanabe, (2017) which will accelerate and enable further work in this field to be conducted in our labs. Also, the use of alternative analytical techniques for hydrogen detection and measurement has also been lacking in literature and it will be of interest to explore the use of mass spectrometry in this capacity.

With these points in mind the following project objectives have been set for the fulfilment of the M.Sc.:

i) Prepare nanowire devices consisting of PEDOT:PSS/CdSe/Ni/Au/Pt segments as previously described by Mubeen *et al.*, (2013) with the aim of further developing device preparation methodology. This development includes building on work conducted by Fawzy, (2016) such as: Enhancing the working electrode assembly methodology using alternative materials and commercially available options. As well as further describing observations made during the electrochemical preparation of nanowires to optimize the electrochemical deposition parameters.

ii) Design and creation of a simple photoreactor for testing the photocatalytic activity of porous anodised alumina type devices.

iii) Set-up components of an initial testing system that allows for online real time hydrogen detection using mass spectrometry. The testing system will have the potential to be developed for more advanced photocatalytic testing.

Based on the above objectives, it is hypothesised that the devices will be able to produce hydrogen upon being irradiated, based on the success of previous studies. It is further hypothesised that mass spectrometry will be able to detect hydrogen evolved in an online manner.

Chapter 4: Experimental Methods

This chapter provides the details of the experimental techniques used to test the hypothesis formulated in the previous chapter. First the templated electrodeposition technique used to synthesise photo-active nanowires is described followed by characterization techniques. Post treatments to improve the activity and stability of the nanowires are then discussed followed by the catalyst testing methodology.

4.1: Chemicals and apparatus

Details of all reagents and materials used and described in this experimental method can be found listed in Table A1.1 in Appendix A1.

4.2: Thermal evaporation of silver metal as a contact

4.2.1 Anodised aluminium oxide

Anodised aluminium oxide (AAO) membranes with uniform and ordered cylindrical pores were used as a template for electrochemical nanowire deposition. Membranes with a few different specifications were obtained from either Whatman® or InRedox®. These specifications included various pore diameters of 100 nm, 160 nm and 200 nm with two different membrane diameter sizes of 13 mm and 25 mm (25 mm discs also came with a polypropylene support ring).

4.2.2 Silver evaporation

A thin layer of silver metal was thermally evaporated onto one side of a blank AAO membrane to act as the working electrode during electrodeposition. An excess amount melted silver wire, or a piece of sliver slug were placed into a molybdenum evaporation boat inside an evaporation chamber. The AAO membranes were placed inside a metal holder as described by Fawzy (2016) that kept one side of the membrane exposed approximately 10 cm above the evaporation boat. The chamber was then sealed, and the vacuum pump switched on. Once a high vacuum of approximately $2x10^{-4}$ mbar was obtained, a potential difference of 2 V was applied across the evaporation boat terminals using an external power supply with a current setting at 25% of the maximum current. This caused the evaporation boat to glow red hot and the silver to melt and evaporate onto one side of the AAO membrane. The duration of the deposition was between 15-30 seconds or until a silver screen was observed on the glass walls of the chamber. The current was immediately turned off followed by the vacuum pump. The chamber was then carefully re-

pressurised with nitrogen gas until the chamber seals could be removed and the silver contacted AAO membranes could be carefully removed.

4.3: Assembly of the working electrode

The working electrode for the electrochemical synthesis of semiconducting and metallic nanowires could be assembled using three methods. The first two methods make use of a glass slide support onto which the silver contacted AAO membrane was electrically contacted using copper tape. These two methods are different in how the silver contacted AAO is isolated from the electrolyte. The third method makes use of a commercially obtained electrodeposition holder (obtained from InRedox®) designed specifically for electrodeposition into 13 mm diameter AAO membrane. (refer to Figure 4. 1)

4.3.1 Method 1: Glass slide isolated with double-sided tape

For method 1. A 7 cm segment of a 20 cm piece of adhesive copper tape was stuck down along the centre of a glass slide and the rest of the copper tape was folded in half onto itself to serve as the point of electrical contact. A hole of equal diameter to the membrane size was then cut out of a rectangular piece of double-sided tape. The Ag contacted AAO membrane was then placed Ag side down onto the copper tape at the bottom most part of the glass slide, ensuring that contact between the Ag layer and copper tape is maximised. The double- sided tape is then stuck onto the glass slide such that the cut-out hole aligns with the open pore side of the AAO membrane and that it completely covers any exposed copper tape.

4.3.2 Method 2: Glass slide isolated with nail varnish

For method 2. adhesive copper tape was attached to a glass slide as described above. The Ag contacted AAO membrane was then placed Ag side down onto the copper tape at the bottom most part of the glass slide, ensuring that contact between the Ag layer and copper tape is maximised. Nail varnish, instead of double sided tape, was then carefully applied around the circular edge of AAO membrane using a paint brush with relatively thin and short bristle. It was important to ensure that the nail varnish completely sealed the AAO membrane and that there were no gaps in the application. The nail varnish was then applied to any exposed copper tape surface to insulate the surface. The assembly was then left to dry inside a fume hood for a minimum of 30 minutes before being used as a working electrode.

4.3.3 Method 3: Commercial electrodeposition holder

The PEEK electrodeposition holder is specifically designed to accommodate only one size diameter membrane (13 mm).

Figure 4. 1: Deconstructed components of PEEK electrodeposition holder

The front face of the holder was first unscrewed, and the O-ring lifted out. The AAO membrane was then placed Ag contact side down onto the stainless-steel stub. The O-ring was then carefully placed on top of the AAO membrane and the holder face screwed back on to secure the AAO membrane in place. A metal rod protected by a glass sheath was then screwed into the top of the holder that made contact to the stainless-steel stub. The assembly was then ready to be used as a working electrode.

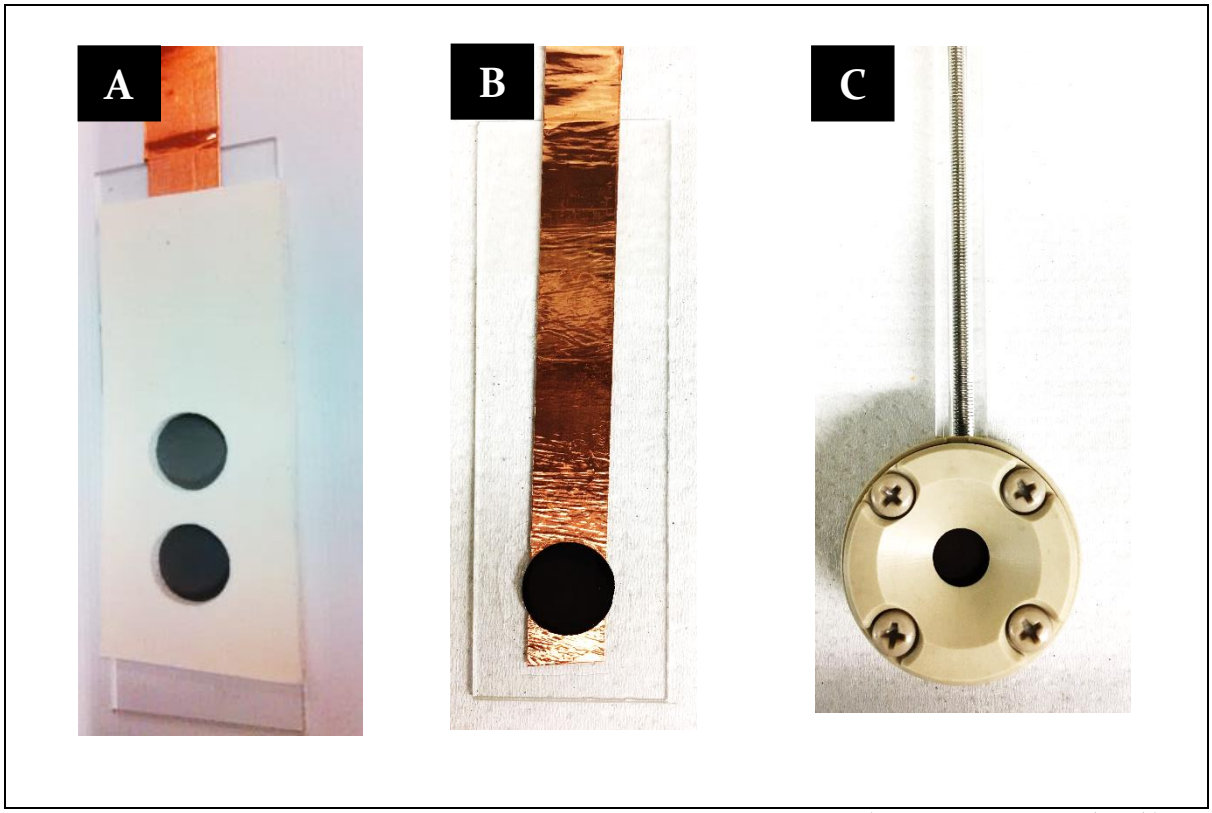

Figure 4. 2: Summary of working electrode construction methods used [A]Method 1 (Adapted from Fawzy (2016)*) [B] Method 2 using nail varnish, [C] Method 3 using an electrodepostion holder.*

4.4: Template directed electrodeposition of nanowire segments

The cell was setup by first connecting the working electrode (WE), reference electrode (RE) and counter electrode to the Gamry (REF 300) potentiostat using the connecting wires and crocodile clips. The electrodes were arranged such that the WE is directly opposite the CE and the RE in the middle. The respective plating solution was then slowly poured into the cell until the AAO disc in the holder was completely submerged. A nitrogen line was then inserted into the solution and degassed for 20 minutes while being magnetically stirred. The solution was then blanketed with N_2 before the electrodeposition script was run.

The cell was thoroughly washed with hot soapy water and rinsed three times with 18.2 MΩ deionised water before between each set of electrodepositions runs. Additionally, the cell was rinsed out with the respective plating solution before an electrodeposition with that same plating solution.

Experimental procedures regarding the electrodeposition of semiconductor (CdSe) and metals (Ni, Au and Pt) are summarised in Table 4. 1:

Table 4. 1: Parameters for the electrodeposition of CdSe, Ni, Au and Pt. Optimised for 160 nm pore diameters used for fabrication of photocatalytic devices.

Nanowire Segment:	Reagent concentrations	Electrodeposition technique	Electrodeposition parameters*
Cadmium Selenide	$[CdSO_4.8/3.H_2O\ ]$ = 5 mM $[SeO_2]$ = 1 mM $[H_2SO_4]$ = 0.25 M pH = 0.75	Cyclic Electrodeposition	Potential: -0.35 V to -0.8 V Scan rate: 10 - 50 mV/s No. cycles: 50
Nickel	$[NiSO_4.6H_2O]$ = 0.23 M $[H_3BO_3]$ = 0.15 M	Chrono-amperometry	Potential: -1 V Deposition time: 500 s
Gold	$[HAuCl_4]$ = 5 mM $[H_3BO_3]$ = 0.5 M	Chrono-potentiometry	Current (mA): -0.35 Deposition time: 250 s
Platinum	$[H_2PtCl_6.6H_2O]$ = 10 mM	Chrono-potentiometry	Current (mA): -0.25 Deposition time:- 600 s

** All potentials are referenced to a Ag/AgCl reference electrode saturated in 3M KCl.*

A comparison of the applied potentials stated in Table 4.1 and the associated theoretical standard potentials are also provided in Table A1.2 in Appendix A1.

Solutions were all made 500 ml at a time, using 18.2 MΩ D.I water, and stored in plastic polypropylene bottles until needed for electrodeposition. Once electrodeposition is started, deposits appear black for CdSe and Ni, slightly orange for Au and dark grey for Pt. Observing partial deposition into the pores usually indicated poor Ag contact formation i.e. pores not sufficiently blocked by thermally evaporated silver film.

It should also be noted that magnetic stirring was only used during cyclic electrodeposition of CdSe and not during or once Ni had been electrodeposited since Ni is a ferromagnetic material and can be loosened from the multi-segmented nanowire structure from the force of a changing magnetic field.

4.5: Disassembly of working electrode

After electrodepositions were completed, all electrodes were disconnected. The Teflon lid was lifted off the cell and all electrodes were rinsed thoroughly using 18.2 MΩ D.I water. The Ag/AgCl RE was kept in 3 M KCl solution until it was needed again. The Pt mesh CE was left to dry in air.

4.5.1 Disassembly of working electrode when Method 1 or 2 was used

The working electrodes constructed using a glass slide in method 1 and method 2 were soaked in acetone for 30 minutes and 10 minutes respectively. This allowed for the double-sided tape to be loosened or nail varnish to be dissolved. The use of tweezers was sometimes required to remove the AAO membrane from the double-sided tape, this had to be done very carefully to prevent the membrane from cracking. For method 2 the membrane usually falls right of the glass slide after 10 minutes of soaking in acetone. After removing the membrane from the glass slide, it was rinsed in D.I water and allowed to dry at 70 °C for 30 minutes.

4.5.2 Deconstruction of working electrode for when Method 3 was used

After the holder was rinsed with D.I water, the AAO membrane is removed by unscrewing the holder face, carefully removing the O-ring, lifting the stainless-steel stub out of the hole and gently sliding the membrane off. Occasionally the membrane would stick to the O-ring, in this case, flat and thin tweezers were used to carefully separate it. The membrane was then rinsed in D.I water, and all the components of the holder were thoroughly rinsed with D.I water. The holder was left to dry in air in its disassembled state until it was to be used again.

If the Ag contact was not covering the pores sufficiently, electrodeposition was seen to occur on the stainless-steel stub. As per supplier guidelines, this was then gently polished off using fine grit polishing paper.

4.5.3 Acid etching of silver contact

The silver etching is important because removal of the silver layer allows the CdSe nanowires to be in contact with the anodic PEDOT layer. Moreover, it allows a large portion of the light to irradiate the photoactive CdSe segment. It is therefore important that the silver layer be removed as much as possible without damaging the CdSe layer.

This was accomplished by making a up a 2:1 solution of nitric acid (70%) and DI water. A small glass vial was placed inside a glass petri dish and then filled up to the brim with the nitric acid solution. Additionally, A small beaker filled with D.I water was kept nearby. The membrane was held near its edge with a pair of tweezers and the Ag contacted side was then carefully lowered onto the top of the vial such that it contacted the nitric acid solution. The Ag contact around the edges where no electrodeposition took place was seen to quickly dissolve. This was done for approximately 10 seconds after which the device is immediately dipped in clean D.I water to halt the etching action. This processed was repeated until the silver layer is seen to be completely removed. Care must be taken not to dissolve the electrodeposited nanowires inside the AAO template. Once the silver contact has been removed, the membrane was again rinsed in D.I water and left to dry at 70 °C in air.

4.5.4 Preparation of nanowire suspension in EtOH

In order to remove the nanowires from the AAO membrane, the membrane was broken in half, put in a 1.5 ml Eppendorf tube and filled with a 3 M NaOH solution to dissolve the template for 1 hour. The Eppendorf tube was kept upright at all times such that all solid material settled at the very bottom of the tube. The supernatant solution was then decanted, taking care not to dispose of the solids that had settled. Decanting could be preceded with a centrifuging step (3000 rpm for 3 min), but this was found not to be required unless small losses of material could not be tolerated. The NaOH dissolution step was repeated for another 30 minutes to completely dissolve any residue of the AAO membrane.

After the AAO membrane had been dissolved, the NaOH was replaced with D.I water, by successively rinsing 3 times with D.I water, decanting the solution between each rinse. Finally, the water was replaced with pure ethanol by successively rinsing 3 times with ethanol, decanting the solution between each rinse. The solids in ethanol were then gently sonicated for 5 minutes

resulting in a dark grey suspension of nanowires. This nanowire suspension could then be drop-casted onto silicon wafers for observation under the optical microscope or the scanning electron microscope.

4.6: Post treatments of photocatalytic devices

4.6.1 Annealing

The electrodeposited nanowires were annealed in argon to ensure that ohmic contact was obtained between nanowire segments and to improve the crystallinity the of the CdSe segments. This was achieved by sandwiching the membrane between two pieces of glass wool inside a glass tube. The tube was then vertically placed inside a furnace, a temperature probe was inserted as close as possible to the membrane, an argon gas line was connected to the inlet and a vent line connected to the outlet. Argon gas was continuously run through the system. The furnace set-point was set to 350 °C for 1 hour, with a ramp rate of 5 °C per minute from ambient temperature. Once the glass tube was cool enough, it was removed from the furnace and the annealed membrane was carefully removed from the glass tube.

4.6.2 Application of PEDOT:PSS as the anode electrocatalyst

PEDOT:PSS was drop-casted onto the CdSe side of the AAO membrane to form a thin transparent and conductive film to serve as the anode electrocatalyst of the photocatalytic device. The membrane was then allowed to dry in air at 120 °C for 1 hour. The membrane was left to cool before it was treated with a few drops glacial acetic acid. The film was then left to dry on a hot plate at 120 °C for 30 minutes under extraction until all the acetic acid had evaporated. The acetic acid treatment was found to increase the film stability in the MeOH solution.

4.7: Physical Characterization

4.7.1 Optical light microscope

An optical microscope was used as a fast and cost-effective method to check that nanowires have indeed formed before making use of more advanced characterisation techniques.

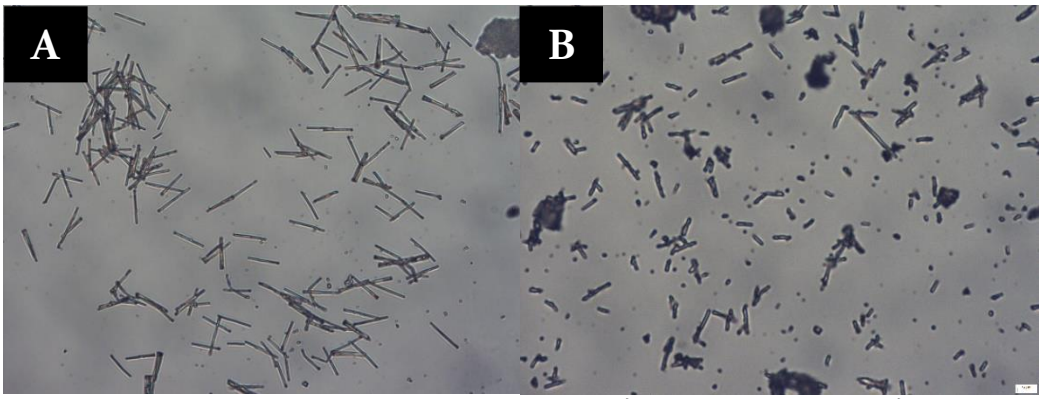

Figure 4. 3: Optical Microscope image at 50 000 x magnification [A} Pure nickel nanowires, [B} Pure Pt nanowires

Nanowires could be magnified up to 100 000 x their size, making it possible to also roughly estimate the lengths of individual nanowires. It should however be noted that this may not be the case if working with smaller sized materials.

4.7.1 Scanning electron microscopy (SEM) & Energy dispersive X-ray spectroscopy

Scanning electron microscopy (SEM) was carried out at the Electron Microscope Unit at UCT. The system, FEI Field Emission Nova NanoSEM 230 make use of an Oxford X-Max detector and Inca software between 5 and 20 kV. Samples were prepared by drop casting a small droplet of a nanowires suspended in ethanol on a clean silicon wafer and quickly dried using a high flow of N_2 gas. The wafers were secured on stubs using adhesive carbon tape. Non-conductive samples (such as blank AAO membranes) had to be carbon coated before examined under the SEM.

This technique was used to observe the nanowire morphology and determine the nanowire dimensions. Additionally, making use of a back-scatter detector greatly helped identify the different nanowire segments.

The SEM system used was also coupled with an EDX detector. This was mainly used to determine Cd/Se atomic ratios in nanowire segments and to confirm the identity of metal segments Ni, Au and Pt.

4.7.2 X-ray diffraction

X-ray diffraction was conducted on a Bruker D8 Advance with a Co Kα radiation source (λ = 0.178897 nm) operating at 35 kV. This technique was used to confirm that the crystal structure of the as prepared CdSe nanowires were cubic CdSe and that a phase change to the wurtzite structure is achieved after annealing at 500 °C for 1 hour. in argon.

The AAO membrane filled with CdSe nanowires were then placed centrally on a sample holder (either zero back-ground or standard), with the x-ray angle being increased from 0° to 120° in 30 minutes using the standard holder and 70 minutes using the zero-background holder. The reason for a slower scan with the zero-background holder was due to the membrane shifting while being scanned due to the smooth surface of the zero-background holder and the rotational motion of the stage.

4.8: Testing of Photocatalysts

This section explains how the photocatalytic devices prepared in the previous section are tested for their hydrogen evolution ability in various aqueous media.

4.8.1 Solar simulator

A 1.6 kW xenon lamp as part of a SPI solar cell tester providing AM 1.5 global terrestrial conditions was used as an irradiating light source during photocatalytic testing, the light intensity ranges between 700 -1100 W/m² ("Ni ve rs ity ap e To w n ve rs ity of e To w", n.d.).

The solar cell tester could only be used in 20-minute increments as over-heating would occur. This was one limitation in the testing methodology, that photocatalytic materials could not be irradiated for longer periods of time.

4.8.2 Photoreactor

4.8.2.1: Construction of the photoreactor

Pasteur pipettes (Borosilicate) were cut and blown using a glass cutter and a small blow torch respectively to make the bubbler, photocatalyst holder and cover. Epoxy resin was then used to hold these components in place inside a cylindrical polytope glass vial (Soda lime). The epoxy was hardened in air at 70°C for 2 hours.

4.8.2.2: Photoreactor set-up under irradiation

A glass photoreactor designed and made inhouse was used to test photocatalytic devices in various aqueous media to produce hydrogen gas. A schematic of this set-up is shown in figure 4.4.

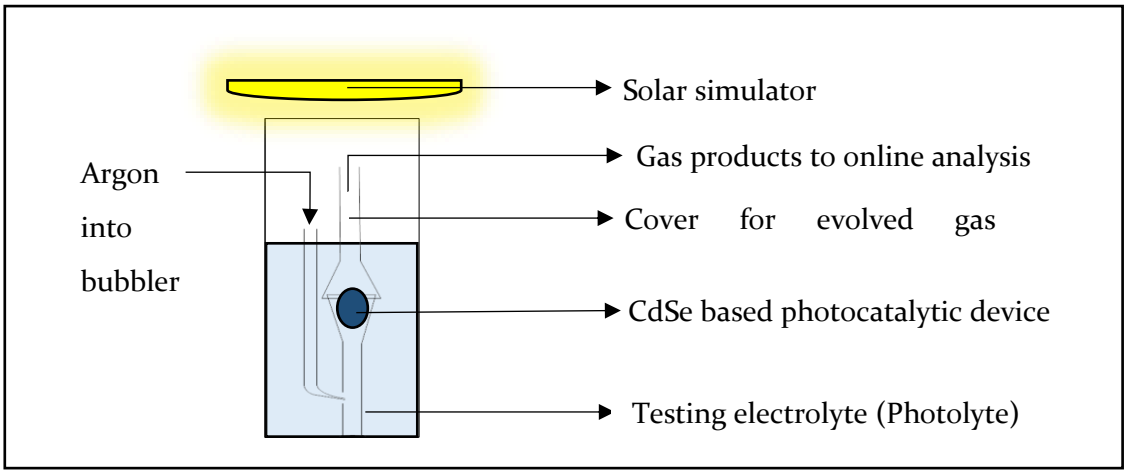

Figure 4. 4: Schematic of photoreactor set-up for testing of photocatalytic devices

Argon gas was bubbled at 3.5 ml/min and was used as a carrier gas as well as an agitator for the photocatalytic device to knock off bubbles adsorbed on the surface that would otherwise not be collected. Due to the pressure drop across the photoreactor, the gas product flow rate could not be measured with a bubble column. This unfortunately meant that the flow rate of evolved species such as hydrogen could not be measured using the mass spectrometer.

4.8.3 Testing electrolyte used for hydrogen evolution

An 80 vol. % MeOH testing electrolyte was used for the photocatalytic evolution of hydrogen gas.

4.8.4 Mass spectrometer

The gas product line is connected to and analysed by a Pfeiffer Omnistar mass spectrometer, model GSD 301 with a mass range of 1-300 amu, operated in molecular ion detection (MID) mode and using Quadstar 422 software for data analysis. The mass spectrometer ionises the incoming products with an electron beam and measures the ion current for each specified species. The expected gaseous species were N_2, O_2, Ar, H_2O, H_2, CO_2 and MeOH. A unique mass to charge ratio (m/z) characteristic of each species was used to calibrate the mass spectrometer, these are reported in table A1.3 in Appendix A1.

This allowed an increase or decrease in hydrogen gas to be observed and related to the time the photocatalytic device had been irradiated. If increases in the hydrogen ionic current is observed with radiation, this would imply that the devices are photo-active. Additionally, decreases in the hydrogen ionic current in the absence of irradiation would also imply photoactivity. Once this can be confirmed more rigorous testing of these types of devices can be tested that explores their stability and activity.

4.8.5 Detection of hydrogen

To ensure that the set-up shown in figure 4.4 was able to detect hydrogen gas via the mass spectrometer capillary, a solar cell connected to a mini bench-top electrolyser was used to generate hydrogen gas from pure water under illumination from the solar simulator. A schematic of this set-up is provided in Figure 4.5.

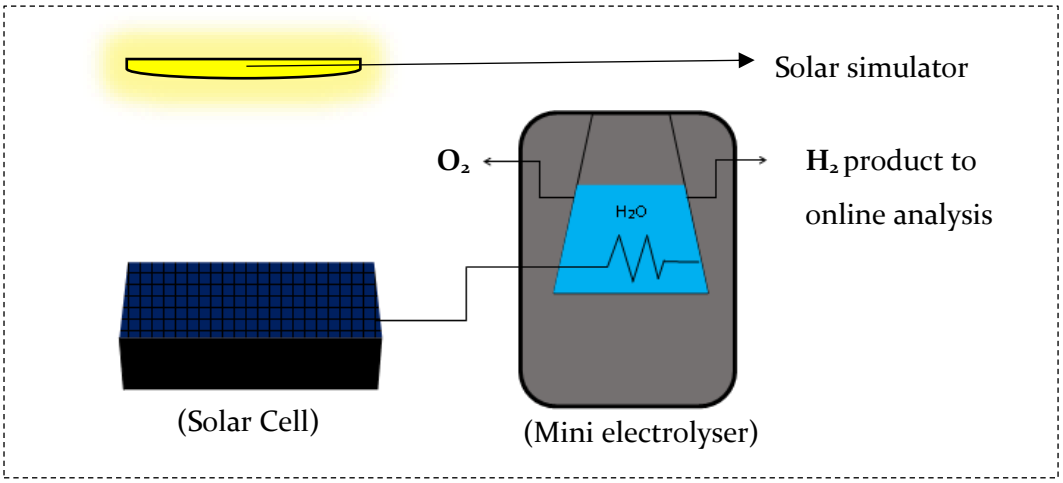

Figure 4. 5 Schematic of set-up used to generate hydrogen gas for calibration of mass spectrometer

The mass spectrometer was calibrated using the mass/charge ratios provided in Table A1.3 in Appendix A1.

4.8.6 Photocatalytic testing protocol

the following photocatalytic testing protocol was developed with aim of having a consistent method of testing to ensure reproducibility and comparability of photocatalytic performance.

1. Rinse reactor with D.I water 3 times.
2. Allow reactor to dry in the oven for 20 minutes until completely dry.
3. Carefully insert the photocatalyst into the holder.
4. Connect the Ar gas line to the bubbler setting the flow to 3.5 ml/min.
5. Insert glass cover connected to the mass spec and ensure that it completely covers the catalyst holder.
6. Put the photoreactor system inside the illumination area tilting it slightly allowing the photoactive CdSe layer to face the light.
7. Slowly add solution, ensuring that the liquid level covers the catalyst and that Ar gas bubbles are not leaking out the sides and are being channelled through the cover.
8. Close the covers around the illumination area.
9. Set the Mass Spec to MID mode and open the valve, allowing 10 minutes for the ion currents to reach steady state.

10. Ensure that the bubbles are all still being collected into the mass spec cover.
11. Restart Mass Spec cycle and wait 5 minutes.
12. Switch the light on.
13. Allow it to run for 20 minutes.
14. Switch the light off.
15. Leave the mass spectrometer running for a further 5 minutes before turning it off, saving the data.

After the testing of a device, the solar simulator was left off for 30 minutes to cool down before another device could be tested.

Chapter 5: Results & Discussion

This chapter presents the results obtained in pursuit of the objectives and hypotheses previously stated using the methods outlined in the previous chapter. Firstly, the significant advances made to the methodology for preparing photocatalytic nanowire devices using the template directed electrodeposition technique is presented in section 5.1:. Section 5.2: then focuses specifically on the electrosynthesis and characterisation of semiconducting CdSe nanowires while section 5.3 focuses on the electrosynthesis of the pure metal co-catalyst materials Ni, Au and Pt. Section 5.4: uses the insights obtained from single component electrosynthesis in sections 5.2: & 5.3 and presents results obtained for multi-segmented nanowires. Lastly, the significant advances made to the photocatalytic testing methodology as well as the results obtained with the established system is presented in section 5.6:

5.1: Template directed electrodeposition - Method development

Considerable progress has been made to the ease of how nanowires are synthesised using template directed electrodeposition specifically regarding the assembly and disassembly of the working electrode that uses fragile anodised aluminium oxide (AAO) substrates.

5.1.1 Synthesis

5.1.1.1: Porous anodised aluminium oxide membranes

AAO membranes of two different average pore sizes were used as a template for nanowire growth to determine possible effects on the electrodeposition parameters. The popular 200 nm pores (Figure 5. 1 A) are supplied by Whatman® and have been used in various reported literature

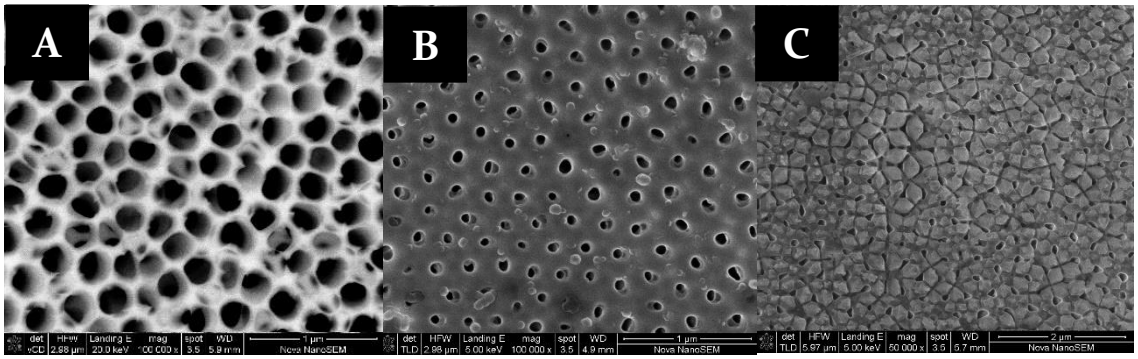

Figure 5. 1 SEM images of porous AAO membranes. [A] 200 nm pores .[B] 160 nm pores side 1 .[C] 160 nm pores reverse side.

(Peña *et al.*, 2002; Kumar *et al.*, 2010; Mubeen *et al.*, 2013).The 160 nm pore membranes (Figure 5. 1 B & C) are supplied by InRedox® a more recently established supplier of these and other materials related to the electrosynthesis of low-dimensional nanomaterials.

Although Whatman® membranes have been popular, they are prone to cracking and break quite easily. They also come in a small range of pore sizes to choose from. Additionally, the actual diameter of the nanowires have been found to be ca 50 -100 nm larger than the pore size rating (Peña *et al.*, 2002; Fawzy, 2016). 13 mm 25 mm diameter membranes were used for electrodeposition of nanowires. 25 mm diameter membranes with a polypropylene support ring were found to be very easy to handle, the support ring however could not handle temperatures above 100 °C and would cause disfiguration of the entire membrane. Therefore, devices for testing were only fabricated using 13 mm diameter membranes.

InRedox® have provided more robust membranes that are less prone to cracking and breaking with more consistency between pore size rating and actual nanowire diameter. The membranes are also fully customizable in terms of pore size, membrane thickness, membrane shape and membrane diameter. SEM images taken of each side (Figure 5. 1 B & C) of their membranes however, show that one side is smooth with good exposure of the pores (Figure 5. 1 B) and that the reverse side is covered with flat protrusions (Figure 5. 1 C) between the pores that hinder their exposure. Although how this would affect the process of electrodeposition is not yet clear, it is nearly impossible to distinguish which side is which with the eye making it difficult to consistently use the same side. This feature was not observed in the imaging of Whatman® membranes.

A comparision between theses membranes from the different suppliers also show a stark contrast between the interpore distance, with Whatman® pores arranged quite densly as opposed to the InRedox® membranes where pores are ca. 200 nm apart from each other.

5.1.1.2: High vacuum evaporation of silver films as a conductive substrate

Silver films, evaporated from pieces of pure silver wire onto one side of AAO membranes function as the working electrode during the electrodeposition of nanowires. The evaporation was carried out using a high vacuum of $2x10^{-4}$ mbar, the evaporation was carried out for between 20 – 40 seconds. This is a rougher vacuum than was used by Fawzy (2016) of $\approx 10^{-6}$ mbar, and significantly reduced the time needed to evaporate the film as the vacuum pump took about an hour to reach $\approx 10^{-6}$ mbar and only about 10 minutes to reach $\approx 10^{-4}$ mbar.

It is critical that a conductive silver film that effectivley blocks the membrane pores is evaporated. If the pores are not sealed off with the film, the electrolyte will leach through open spaces and deposit onto any other conductive surface creating difficulty in forming nanowires.

Fortunatley a fast visual test can be applied, if the deposited film resembles a shiny silver colour then silver has been successfully deposited.If however the film is shiny with a slight brown or gold colour then the silver evaporated is not covering the pores completey as shown in Figure 5. 2 B.

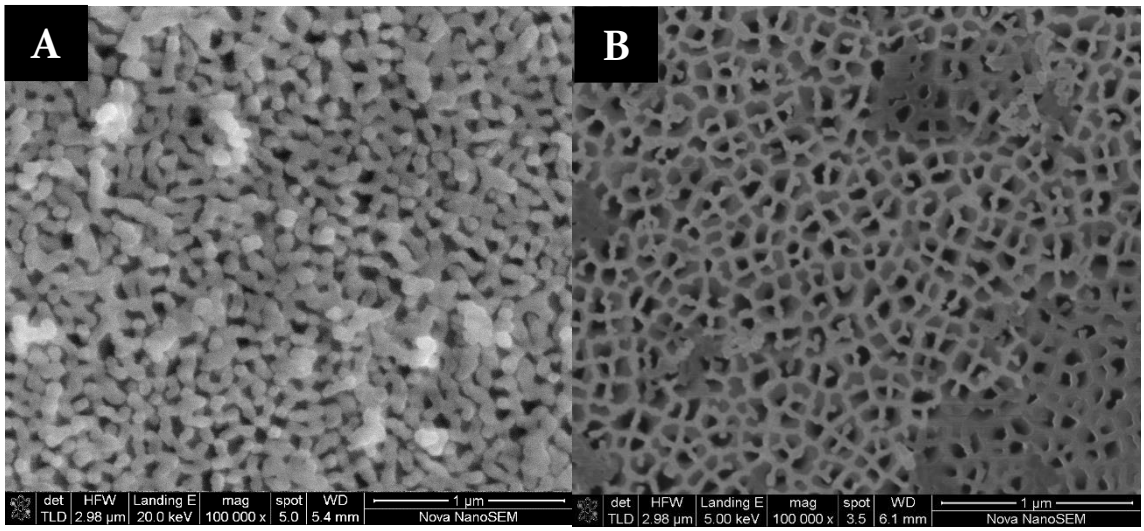

Figure 5. 2 SEM images of evaporated silver films. [A] Film evaporated at 2x10^{-4} mbar suitable for electrodeposition. [B] Film evaporated at 5x10^{-5} mbar unsuitable for electrodeposition

It is not at this stage clear as to why the film morphology breaks down when thermally evaporated at a higher vacuum level which results in an outlining of the pores with silver instead of covering the pores, but it was clear that the former case does not allow for successful deposition of nanowire material.

5.1.1.3: Methods of working electrode assembly: Advantages and disadvantages

In order to ensure electrodeposition only happens inside the pores and not on the back-side of the silver film, this side must be isolated from the electrolyte. This can be done in three ways, two of which have been made use of in this work. The reader is referred to the experimental section which shows images of these working electrode assemblies.

1. A glass slide with copper tape down the centre and double- sided tape with a 13 mm hole used to stick the AAO membrane down and electrically isolate it.

Figure 5. 3: Working electrode constructed using double-sided tape (adapted from Fawzy, (2016)*)*

2. A glass slide with copper tape down the centre and nail varnish used to isolate to seal the edges of the AAO membrane onto the conductive copper tape.

Figure 5. 4 Working electrode constructed using nail varnish to isolate the porous membrane

3. A holder made of PEEK, designed specifically for electrodeposition into AAO membranes. (Acquired from InRedox®)

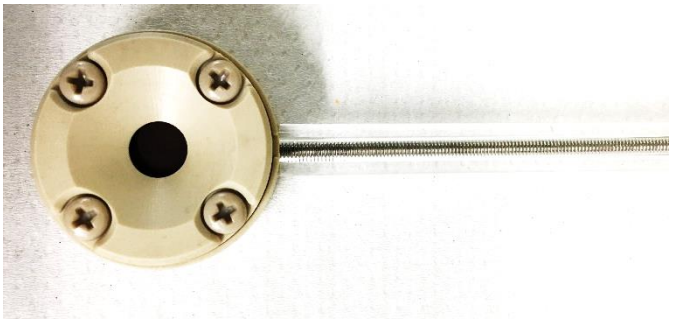

Figure 5. 5 Working electrode construction using an electrodeposition holder

This development in the working electrode assembly shown in Figure 5. 3, Figure 5. 4 & Figure 5. 5 used for the template directed electrodeposition of nanowires shows that this type of technique can be implemented using simple materials, making it more accessible for further investigation and development. Especially since explanations of how this is carried out is largely vague and rarely found in the literature looked at. The advantages and disadvantages of using these assembly methods is describe in Table 5. 1 .

Table 5. 1 Advantages and disadvantages of working electrode construction methods

Method	Advantages	Disadvantages
1	✓ Proper isolation of AAO membrane is achieved ✓ Multiple AAO membranes can be used at once ✓ Materials are easily available and cost effective. ✓ Can be used for small (13 mm) or large (25 mm) diameter membranes.	X Removal of AAO membrane after being stuck easily causes cracking or breaking of the membrane. X Many contaminates, and foreign matter are present on the double-sided tape with unknown consequences during electrodeposition.

2	✓ Proper isolation of the AAO membrane is achieved. ✓ Multiple AAO membranes can be attached ✓ Can be used for small (13 mm) or large (25 mm) diameter membranes. ✓ Nail varnish has proven to be stable and inert even in acidic media ✓ Nail varnish readily dissolves in acetone allowing easy removal of the AAO membrane.	X Leakage of nail varnish occurs into the pores around the edges of the membrane reducing the electrochemically active surface area for electrodeposition to take place. X Requires careful and even application around the AAO membrane. X Requires 30 – 60 minutes of drying time
3	✓ Proper isolation of the AAO membrane is achieved. ✓ The holder is made from PEEK, which is a chemically, mechanically and thermally stable thermoplastic.	X Can only accommodate one AAO membrane for electrodeposition at a time X A separate holder must be purchased for different membrane diameters. X Costly

All three of the methods for the construction of the working electrode outlined in Table 5. 1 have successfully been used to electrochemically grow nanowires. Due to the brittleness of the AAO membranes however, and how sensitive to contaminates electrodeposition is, method 3 was predominately used to construct devices for testing. Method 3 minimises the need to directly handle the AAO membrane, reducing the risk of breaking them. Additionally, it eliminates sources of possible contamination such as double-sided tape or nail varnish in contact with the electrolyte.

5.2: Cadmium selenide nanowires

This section contains details on the template directed growth of CdSe nanowires by applying cyclic voltammetry and is referred to as cyclic electrodeposition. The behaviour of the curves from start to finish is observed to better understand how this affects the stoichiometry of the resulting nanowires.

5.2.1 Cyclic electrodeposition of CdSe nanowires

5.2.1.1: Cyclic electrodeposition of CdSe nanowires into 200 nm pores.

In the following three figures, the progression of the CdSe nanowire growth is shown. Figure 5. 6 shows the first 10 cycles. Figure 5. 7 shows every 10th cycle of cycle 10 to cycle 160. Finally, Figure 5. 8 shows every 10th cycle of cycle 170 to cycle 300. This was done to simplify the graphs so that curve transitions could be more easily observed.

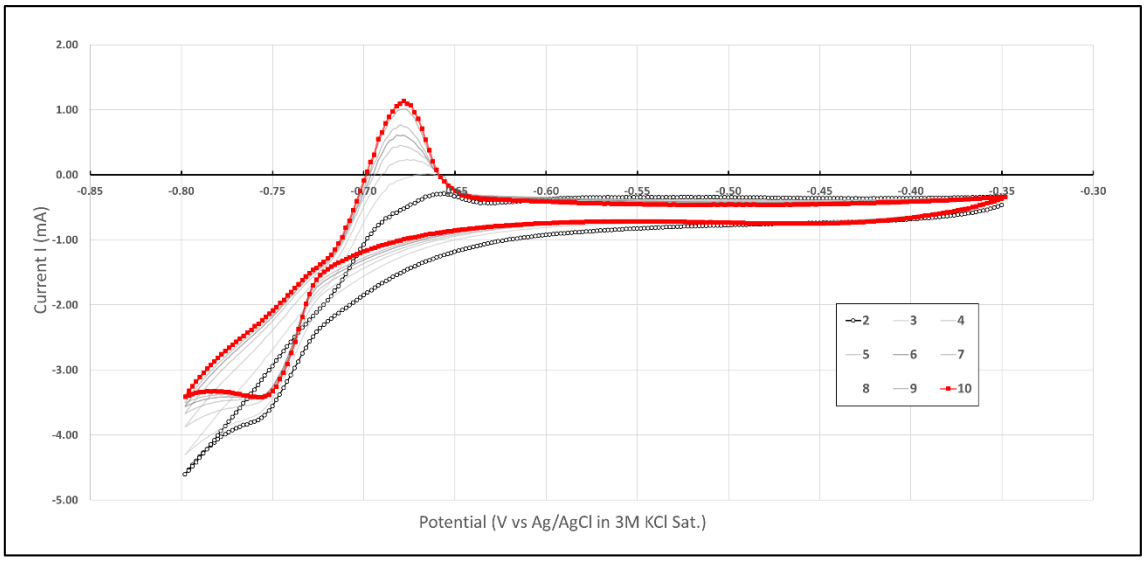

Figure 5. 6 First 10 cycles of cyclic CdSe electrodeposition into 200 nm pores

The very first few curves throughout all the depositions performed have been observed to reach relatively high negative currents down to -12 mA at times. This is thought to be due the presence of a high initial concentration of electroactive ions at the working electrode surface and/or formation of silver alloys with Cd and Se species. It could also be due to the removal of surface impurities. For this reason, the first cycle has been omitted from Figure 5. 6. The first 10 cycles are also normally characterised by a big shift to more positive currents, with cycle two appearing completely below the x-axis and cycle 10 having a part of its stripping peak in the above the x-axis.

The first 10 cycles, observe peaks shifting into more steady state positions with an overall shift to more positive currents. It therefore would make sense that the nanowire piece grown from the first 10 cycles or so would be very unbalanced regarding the ratio of cadmium to selenium and even more due to the presence of silver alloys with these elements.

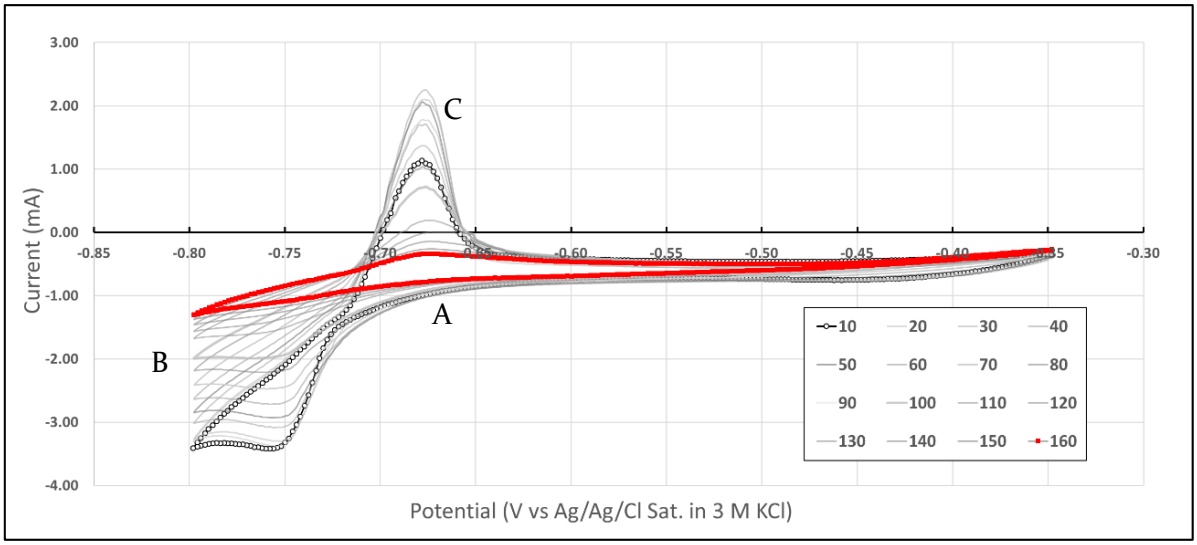

Figure 5. 7 Every 10th cycle of cycle 10 to cycle 160 of CdSe cyclic electrodeposition into 200 nm pores

CdSe electrodeposition is typically cycled from -0.35 V to -0.8 V and back to -0.35 V. Along this path, the onset of the reduction peak is observed to occur rapidly at -0.73 V and with a dip at -0.76 V. On the reverse cycle, the Cd stripping peak occurs at -0.68 V. These are the steady state reduction and stripping potentials of this system as seen in Figure 5. 7.

After the first 10 cycles, the reduction and oxidation peaks remain relatively consistent with respect to potential. Both peaks however shift with respect to current. The current associated with the oxidation and reduction peak becomes more positive from cycle 10 to cycle 50 approximately. From cycle 50 to cycle 160 however, the oxidation peak current decreases while the reduction peak current continues in the positive direction. The features of the cycle diminish as the growth progresses. Which is most likely due to the ions being depleted in the electrolyte with each cycle.

The steady state cyclic voltammogram presented here corresponds well to what other researchers who have used cyclic electrodeposition technique of CdSe and have presented this information (Kressin *et al.*, 1991; Shpaisman & Givan, Uri Patolsky, 2010; Fawzy, 2016).Although some researchers state they have used this electrosynthesis technique, but do not present their obtained cyclic voltammetry data (Klein, Herrick, *et al.*, 1993; Peña *et al.*, 2002; Schierhorn *et al.*, 2009)

The progression of the CV and the formation of stoichiometric CdSe was first elucidated by Kressin *et al.* (1991) who first developed the technique for CdSe thin films. Following his explanation, the region labelled A on Figure 5. 7 is where CdSe is deposited along with excess Se. Se electrodeposits much more readily than Cd at these potentials, noting that its standard

reduction potential is much more positive than that of Cd as shown in Table A1.2 in Appendix A1. Region B sees excess deposition of Cd ions due to the higher concentration of Cd^{2+}. Region C is then where excess Cd is stripped back into the solution leaving behind mostly CdSe after which the process is repeated. This explanation was corroborated by Shpaisman & Givan, Uri Patolsky (2010) who repeated the process but for electrodepositing nanowires as opposed to films and is critical to the formation of stoichiometric deposits.

Differences are observed in the anodic peak potential where Cd is stripped. For Kressin *et al.*, (1991) & Shpaisman & Givan, Uri Patolsky (2010), This stripping occurs at less negative potentials of ca. -0.6 V.(Vs Ag/AgCl for Shpaisman & Givan, Uri Patolsky (2010) and Vs SCE for Kressin *et al.*(1991)). This is mainly thought to be due to differences in Cd concnetrations as well as the use of different scan rates since Kressin *et al.* (1991) & Shpaisman & Givan, Uri Patolsky, (2010) both use high scan rates of 1000 mV/s and 750 mV/s and both made use of higher concentrations of Cd in their deposition electrolytes (0.3 M $CdSO_4$) as opposed to that used for the results reported here which correspond with the andoic peak position observed by Fawzy (2016) who used similar scan rates (10 -50 mV/s) and similar concentrations of Cd (5 mM $CdSO_4$) to this work.

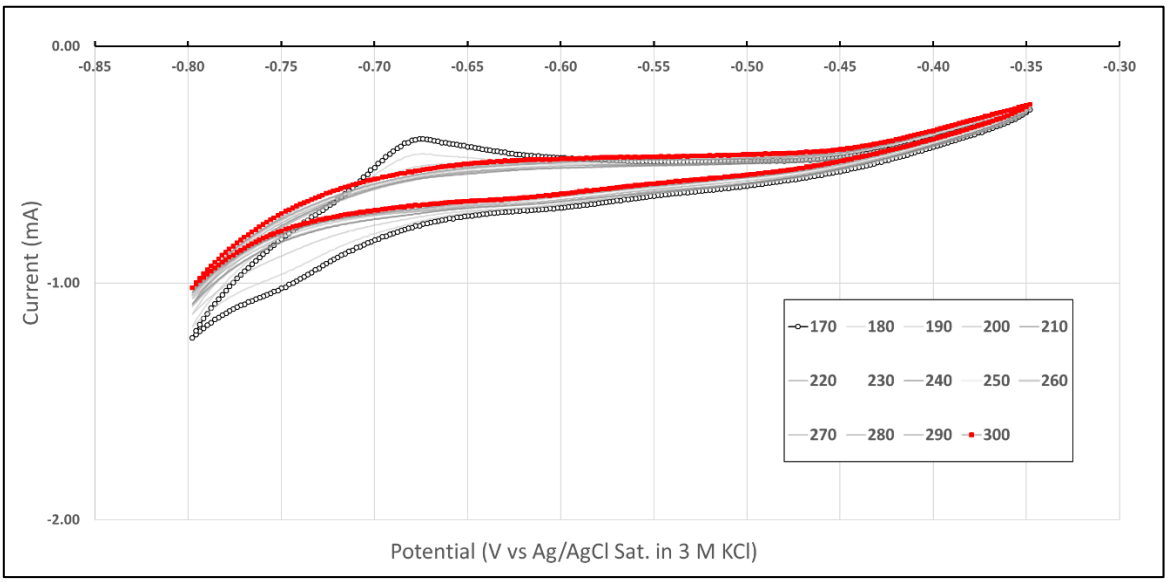

Figure 5. 8 Every 10th cycle of cycle 170-300 of CdSe cyclic electrodeposition into 200 nm pores

Towards the end of the electrodeposition, the peaks featured previously completely disappear and the entire cycle has migrated to the cathodic current region as is illustrated in Figure 5. 8. This behaviour has not been previously reported but is most likely due to the depletion of Se ions in the electrolyte, with electrodeposition happening only for Cd.

This has two implications, first, that if the electrodeposition is carried out for too many cycles the segment deposited after the Se has been depleted below some limit, will predominately be

Cd. To prevent this and ensure that majority of nanowires is stoichiometrically CdSe, the electrodeposition should only be allowed to run for between 80 -100 cycles for this system and parameters used. After 100 cycles, the anodic stripping peak is observed to fall into the cathodic region.

Secondly that if longer nanowires need to be grown using extended cycles, a larger volume of electrolyte will need to be used, such that Se ion depletion becomes negligible or alternatively, the electrolyte will need to be refreshed after a certain amount of cycles.

5.2.2 Electrodeposition of CdSe nanowires inside 160 nm pores

Electrodeposition of CdSe was also carried out inside the pores of 160 nm diameter AAO membranes. The resulting CV for this is shown in Figure 5. 9:

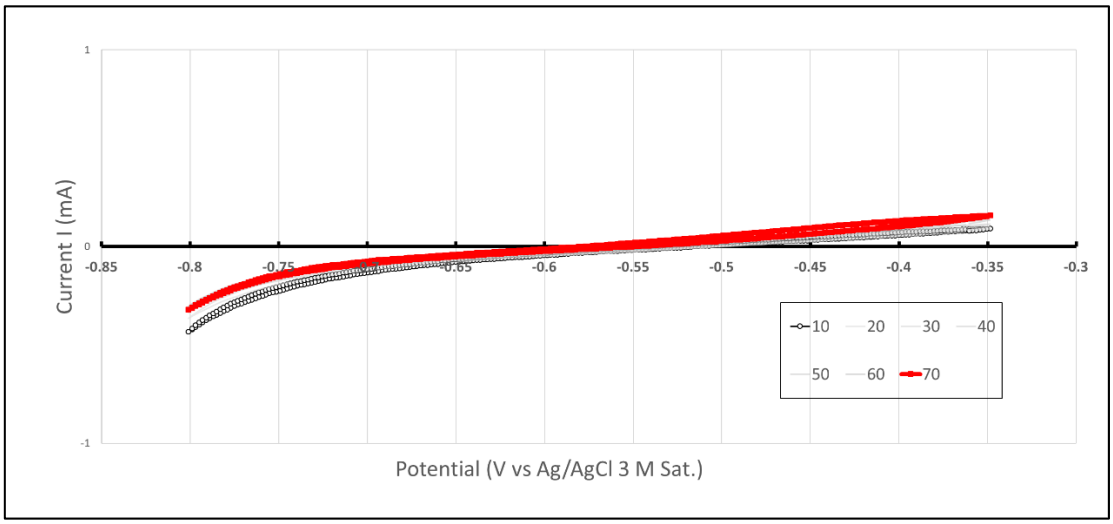

Figure 5. 9: Every 10th cycle of 70 cycles of CdSe electrodeposition into 160 nm pores

The electrodeposition here was carried out for 70 cycles, at a scan rate of 15 mV/s using the same electrolyte compositions as used for 200 nm pores. What is surprising here is that none of the salient peaks associated with bulk Cd deposition and stripping are present as is for the 200 nm pores. Additionally, there appears to be much less shift with respect to current and almost no hysteresis observed for each cycle as there is for the CVs of the 200 nm pores.

This was an unexpected result considering that the difference in pore size was only 40 nm. One does not expect 200 nm pores and 160 nm pores to exhibit such dissimilar behaviour reflected in their respective CVs. A plausible reason may be the effect of the larger inter-pore distance observed in Figure 5. 1 of the 160 nm InRedox® membranes compared to the 200 nm Whatman® pores. These larger inter-pore distances in combination with a smaller pore size would also result in a lower active surface area for electrodeposition which could contribute to the observed

voltammogram. Despite an observed lack in cyclic voltammetry features, nanowires were successfully electro-synthesised from the CV presented in Figure 5. 9 with SEM images presented in Figure 5. 10.

5.2.3 SEM/EDX of CdSe nanowires

Scanning Electron Microscopy was used to assess the morphology of the electrodeposited nanowires, whilst an Energy Dispersion X-ray analysis was used to determine the ratio of Cd to Se in electrodeposited CdSe.

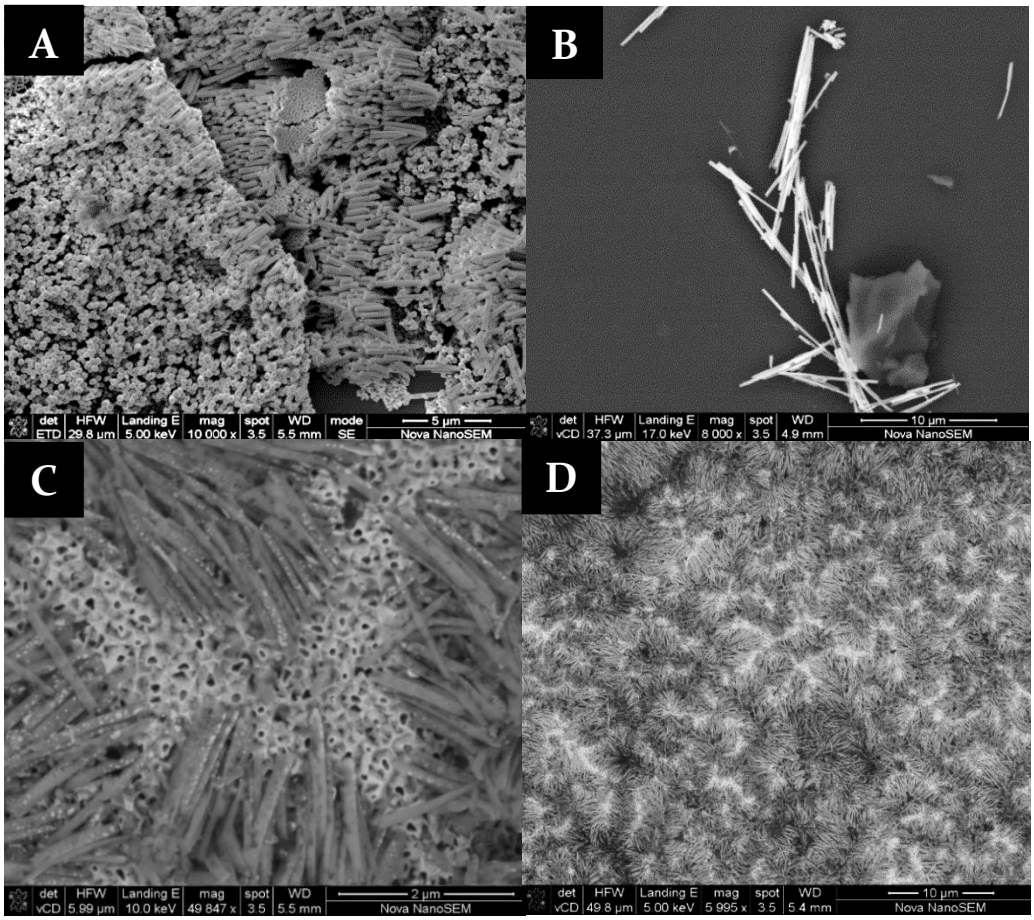

Figure 5. 10 SEM of CdSe nanowires grown in [A] 200 nm pores using a 25 mm diameter AAO membrane. [B] 200 nm of a 13 mm diameter AAO membrane grown for an extended period. [C & D] 13 mm AAO membrane with 160 nm wide pores.

Figure 5. 10 A & B show electrodeposited CdSe nanowires into 200 nm pores. For A, a 25 mm membrane diameter was used with a method 2 working electrode assembly. Image B illustrates nanowires electrodeposited for an extended period ca. 700 cycles using working electrode assembly method 2 as well but with a 13 mm AAO membrane. Image C & D are CdSe nanowire electrodeposits done using a PEEK electrodeposition holder into 160 nm pores. C shows a close-up of these nanowires growing out of their pores while D shows a broader overview of the nanowires. The length of CdSe nanowires can reach up to 15 µm and longer and depend mostly on the number of cycles as observed by Shpaisman & Givan, Uri Patolsky, (2010) as well. In this

work, nanowire length was also observed to be depend on the pore size, with smaller pores being filled faster than larger ones with the same number of cycles and scan rate used. EDX was used to determine the ratio of Cd to Se in the electrodeposited nanowires, these results are shown in Table 5. 2.

Table 5. 2 Atomic ratio of Cd to Se of nanowire samples shown in Figure 5.10

Sample	**Cd (at%)/Se(at%)**
[A] 200 nm pores using a 25 mm diameter AAO membrane	8.6
[B] 200 nm of a 13 mm diameter AAO membrane grown for an extended period	1.5
[C & D] 13 mm AAO membrane with 160 nm wide pores.	0.82

This EDX analysis was done to determine the atomic % of Cd and Se and the ratio Cd/Se was calculated by averaging the data of all points analysed for each corresponding sample shown in Figure 5. 10.

Nanowires shown in Figure 5. 10 A were found to be rich in Cd whereas nanowires for B, C and D were found to be closer to stoichiometric proportion. This shows that a significant variation in the ratio between Cd and Se can occur in these electrodeposited nanowires even though experimental conditions are kept consistent. A potential reason for the variation in the stoichiometry could be due to the use of different membrane sizes but more likely linked to the relative consumption of the Se and Cd ions during the deposition. Small changes to the ratio between these ions have been observed to cause big difference in the stoichiometry. Shpaisman & Givan, Uri Patolsky (2010) also reports that significant variation in the ratio between Cd and Se can occur along the length of nanowire axis when either just a forward or reverse scan is isolated for the electrodeposition, but this was observed to be corrected when full cycles were applied.

It is not yet clear how significant variation in the stoichiometry of electrodeposited nanowires as seen in Table 5. 2 can affect its photocatalytic performance. This is one of the main drivers for further understanding the behaviour the cyclic electrodeposition process. Understanding this process will also help understand how CdSe nanowire growth can be optimised to produce quality stoichiometric nanowires more consistently.

5.2.4 X-ray diffraction of CdSe nanowires embedded in pores

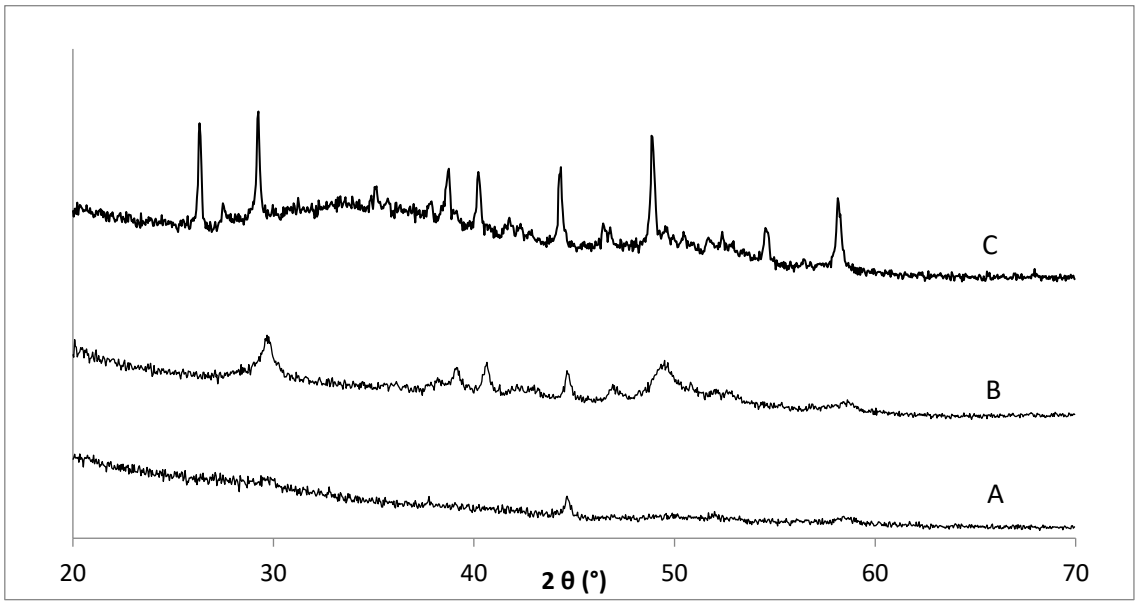

Figure 5. 11: X-ray diffraction plots of different sides of CdSe nanowires embedded in AAO membrane {A, B] XRD scan of side 1 and 2 respectively. [C] XRD of side 2 after annealing.

X-ray diffraction was performed with the nanowires embedded inside the membrane pores and it was found that a reliable signal could be obtained when the side of AAO membrane where CdSe had been deposited and Ag layer etched was exposed, as is shown by scan B. Scan A shows the result for the reverse side to B where a reliable signal was not obtained. Scan C was done on the same side as B after the embedded nanowires were annealed in at 350 °C in Ar for an hour. Reference patterns for the peaks obtained in Figure 5. 11 are illustrated and discussed in Figure 5. 12

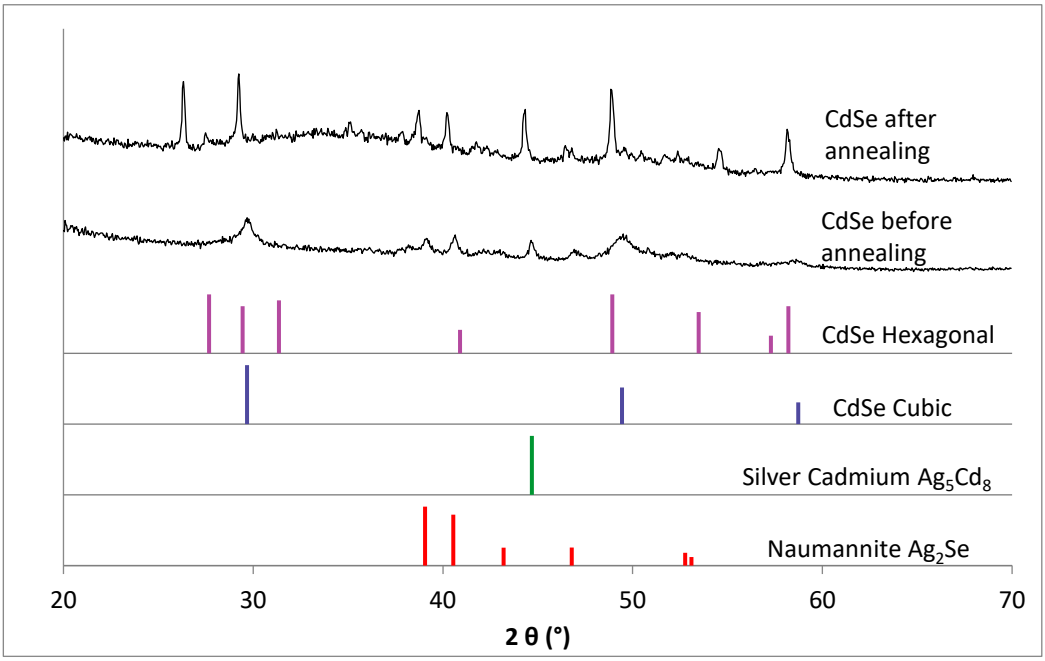

Figure 5. 12: X-ray diffraction plots of annealed and unannealed CdSe nanowires embedded in porous AAO membranes including the relevant matching reference patterns. Naumannite: PDF 01-071-2410, Silver Cadmium: PDF 03-065-3158, CdSe Cubic: PDF 03-065-2891, CdSe Hexagonal: PDF 00-002-0330

The XRD analysis confirmed the zinc blend or cubic crystal structure for unannealed or as prepared CdSe nanowires. Annealing of the embedded nanowires produced scans with sharper peaks indicating an increase in the crystallinity, this is accompanied with a phase transformation from cubic to hexagonal or wurtzite all of which has been reported in previous studies for electrodeposited CdSe (Kressin *et al.*, 1991; Fawzy, 2016).

Annealing also resulted in a shifting of the resulting peaks, causing a mismatch between the hexagonal or wurtzite crystal structure reference pattern. The exact reason for this is not known but it is suspected that it could either be due to an interaction between CdSe and the anodised alumina membrane during annealing or because the nanowires are preferentially arranged in a vertical manner by nature of being embedded in the membrane. Joo *et al.* (2006) observed XRD peak shifting to higher angles for CdSe nanoribbons in with a wurtzite crystal structure. This was attributed to a contraction of the crystal lattice due to high surface tension. Since a shift to lower angles is observed in Figure 5.12, this may then indicate an expansion in the lattice structure post annealing.

The presence of Ag_2Se as well Ag_5Cd_8 were also noted in the diffractogram show in Figure 5. 11. With other researchers reporting similar appearances of Ag in their XRD patterns (Xu *et al.*, 2000; Peña *et al.*, 2002) as a result of using it as the cathodic substrate. The presence of these Ag species was difficult to eliminate even after multiple etching treatments with HNO_3.

5.3: Electrodeposition of nickel, gold and platinum nanowires

After the cyclic electrodeposition of CdSe, conductive metals Ni and then Au are electrodeposited on top of the CdSe segment forming multi-segmented nanowires. This forms an ohmic contact to the CdSe segment allowing electrons to be conducted away from the CdSe segment. Pt is finally electrodeposited at the end to function as the HER electrocatalyst. This section describes what electrochemical techniques was used for the electrodeposition of each of these metals and the associated parameters. Challenges faced during the electrodeposition of these metals are also mentioned and how they were overcome.

5.3.1 Electrodeposition of nickel nanowires

Chronoamperometry or constant potential electrodeposition was used for the electrodeposition of Ni into the pores of the AAO membrane. Ni electrodeposition using the parameters outlined in the experimental methods chapter was found to be the most straight forward electrodeposition with high chances of successful nanowire formation.

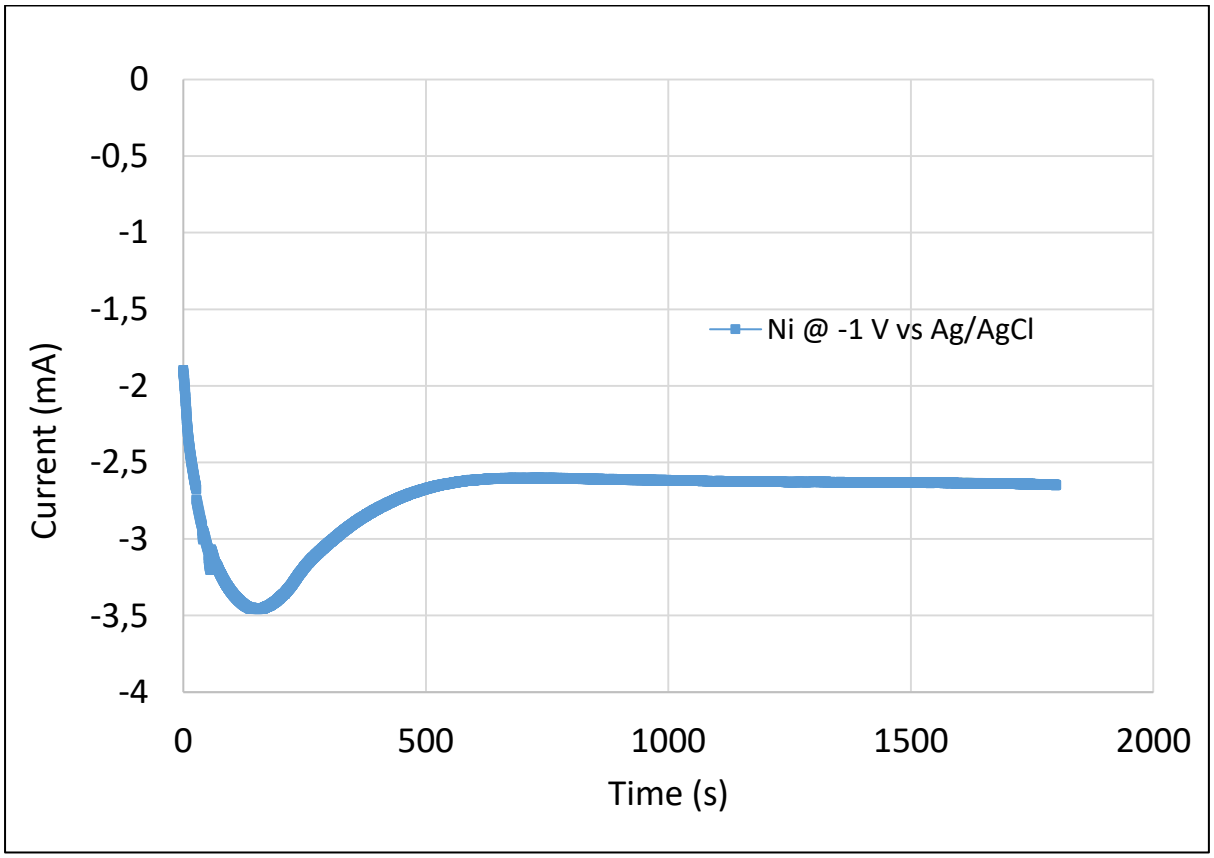

Figure 5. 13: Chronoamperometry applied for the electrodeposition of Ni, Au and Pt nanowires

Nickel was deposited first at -1 V vs Ag/AgCl. The electrodeposition of Ni was almost always observed to have an initial dip in current after which the curve flattens out. this has been

reported to be due to the immediate nucleation of crystallites onto the conductive Ag substrate at the bottom of the pore.

5.3.2 SEM and TEM analysis of Ni nanowires

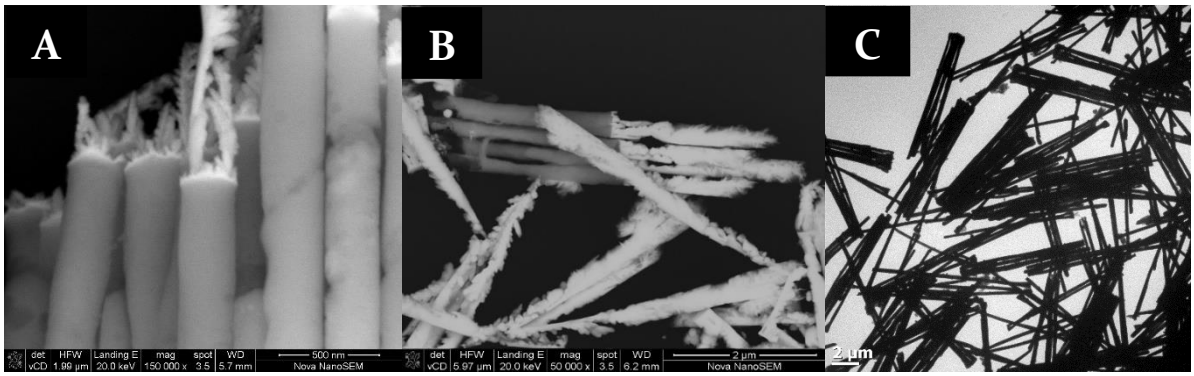

Figure 5. 14: SEM images of Ni-Au-Pt nanowires using a backscatter detector [A &B], TEM image of pure Ni nanowires [C].

The chronoamperogram shown in Figure 5. 13 results in the Ni nanowire structures shown in Figure 5. 14. An EDX analysis has identified the darker deposits as nickel and the brighter ones as gold and platinum for image A and B. It was observed that the morphology of nickel conforms well to that of the cylindrical pore being ca. 250 nm in diameter.

5.3.3 Electrodeposition of Au nanowires

Au nanowires were electrodeposited using chronoamperometry as outline by Fawzy (2016).The Au nanowire segment has a dual function, First together with Ni promoting the conduction of electrons formed in the CdSe segment to the Pt electrocatalyst. Its second, less reported function is that it is needed in a protective capacity for the electrodeposition of Pt from chloride based electrolytes since these electrolytes are corrosive towards base metals such as Ni.(Rao & Trivedi, 2005) . It is therefore important for these Au segments to be well formed.

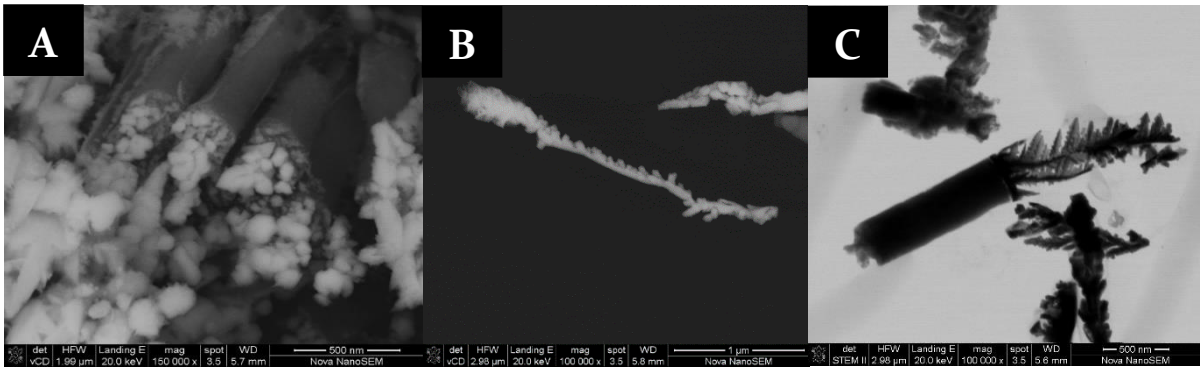

Figure 5. 15: SEM images of irregular Au nanowire electrodeposits

The morphology of Au nanowires was found to be irregular when compared to Ni as is shown in Figure 5. 14 (A & B) as well as Figure 5. 15. These morphologies were observed to be jagged

with small protrusions. This lead to an investigation into alternative electrodeposition technique for Au nanowires. The suspected cause of this is that the rate of deposition was occurring too fast and not allowing enough time for the metal to deposit laterally as opposed along the pore axis. Further suspected causes could be poor pore wettability or concentrations of the electrodeposition salt solutions being too low at 5 mM of the Au precursor $HAuCl_4$.

Habouti *et al.* (2011) had observed similar jagged morphologies of electrodeposited Au nanowires. They used the same Au precursor used in this work but at higher concentrations (1.2 M $HAuCl_4$) with the addition of glacial acetic acid. Their observation was that chrono methods had resulted in jagged nanowire structures while being able to obtain well formed, smooth deposits using a pulsed chronoamperometry electrodeposition technique, but with an unknown cyanide-based deposition electrolyte. Although this made it difficult to compare the two methods these ideas were incorporated here to improve the Au nanowire morphology.

5.3.3.1: Chronoamperometry

To correct the morphology of the Au nanowire segment, several different electrodeposition techniques were applied. This included chronoamperometry, pulsed chronoamperometry, a combination of chronoamperometry and chronopotentiometry as well as just chronopotentiometry. The idea behind applying these techniques was to lower the rate at which deposition was occurring.

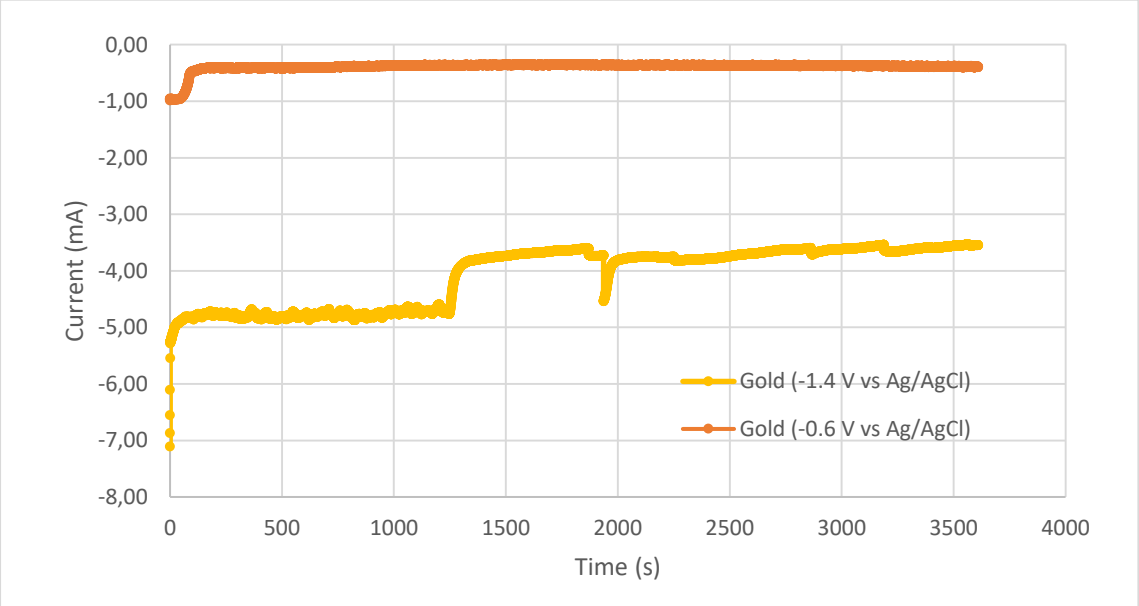

Figure 5. 16: Chronoamperometry for the electrodeposition of Au nanowires at a high overpotential (-1.4V) and a low overpotential (-0.6 V)

The chronoamperogram shown in Figure 5. 16 shows the current response to two different potentials used to electrodeposit Au nanowires. The higher electrodeposition potential (-1.4 V) sees a higher current magnitude and therefore an increase in the rate at which deposition is occurring. For the higher potential deposition, a 2x increase in the magnetic stirrer speed was made at approximately 1250 seconds. The current response immediately decreases in magnitude, indicating that the electrodeposition response is sensitive to changes in agitation speed and that mass transport limitations are present within the system.

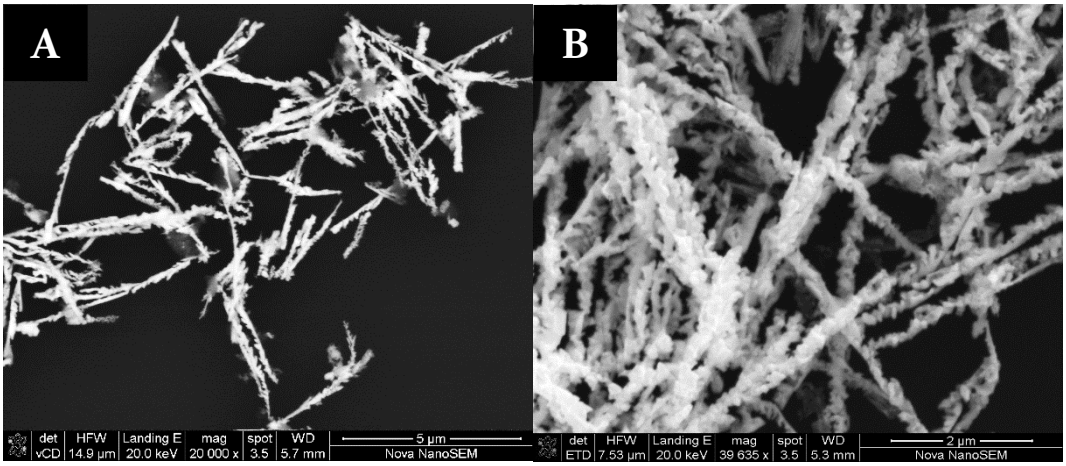

Figure 5. 17: SEM images of Au electrodeposits using both high and low potentials [A] deposited at -0.6 V and [B] deposited at -1.4 V

The resulting electrodepositions from both the high and low potentials used are shown in Figure 5. 17 Both these attempts still show jagged Au nanowire morphologies [B] more so than [A], indicating that higher potentials and therefore faster rates of deposition do not promote complete lateral filling of the pore resulting in well-formed Au nanowire morphology.

5.3.3.2: Pulsed Chronoamperometry

A pulsed chronoamperometry electrodeposition of Au nanowires was attempted. The rational for this was that keeping the potentials positive for short intervals might help keep the concentration of the electroactive Au ions at the solid/liquid interface higher.

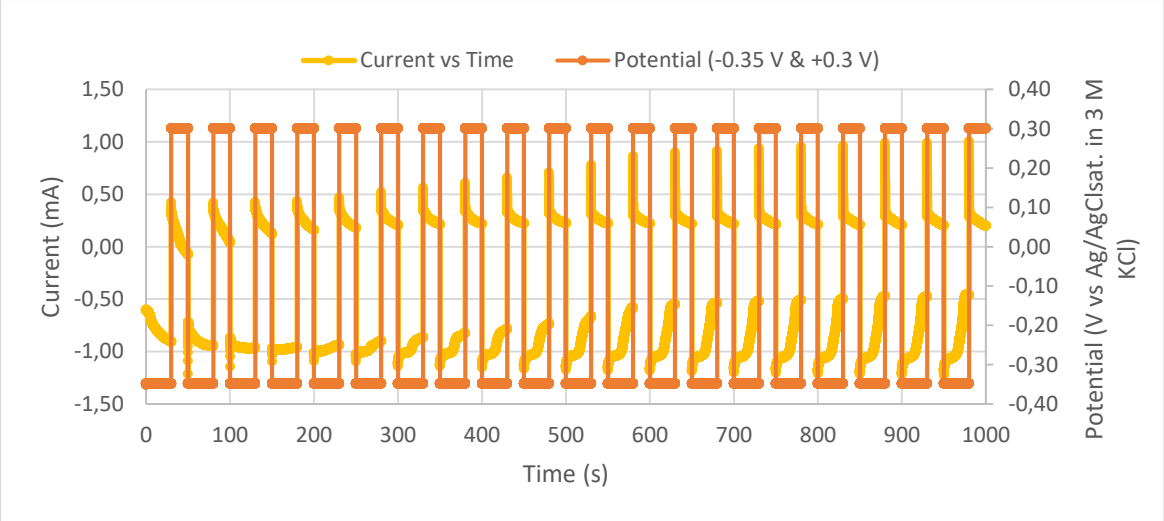

Figure 5. 18: Pulsed chronoamperometry for electrodeposition of Au nanowires

The electrodeposition took place at a potential of -0.35 V for 30 seconds. The potential wave was then kept at +0.3 V for 20 seconds, halting electrodeposition and allowing recovery of the Au ion concentrations at the solid/liquid interface.

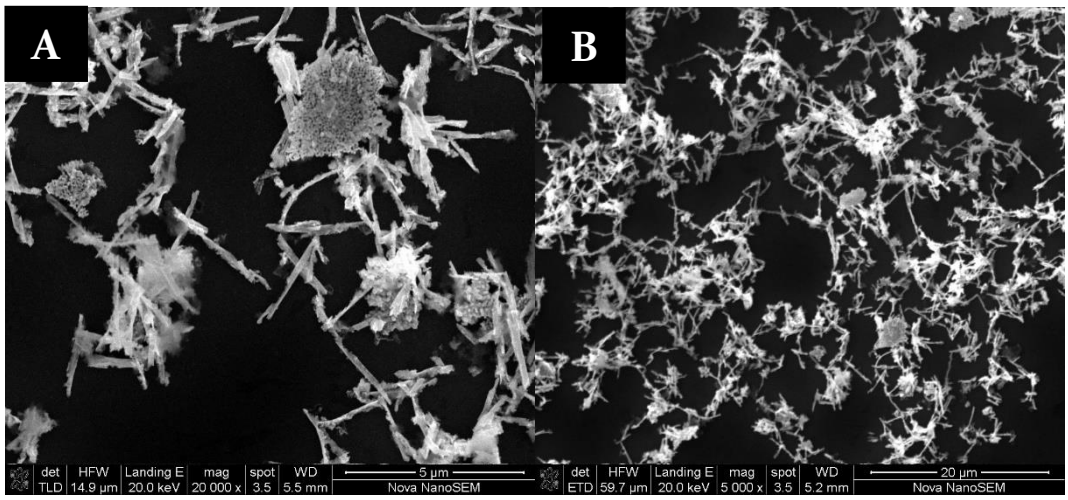

Figure 6. 19: Au nanowires deposited using pulsed chronoamperometry

The SEM images in Figure 6. 19 show the resulting Au nanowire deposits from pulsed chronoamperometry. It should be noted that incomplete Ag etching here has resulted in areas where the Au deposits are attached to Ag layers. Visually it is observed that there is a slight morphological improvement with the use of a pulsed Au electrodeposition, but that this is still accompanied by many defects along the nanowire growth axis.

5.3.3.3: Combined chronopotentiometry and chronoamperometry for gold electrodeposition

Since different variations of chronoamperometry have shown no significant improvement to the morphology of Au nanowire morphology, a current controlled method such as

chronopotentiometry was considered. This entailed fixing the current and allowing the potential to vary with time, which is essentially the reverse of chronoamperometry which was used previously.

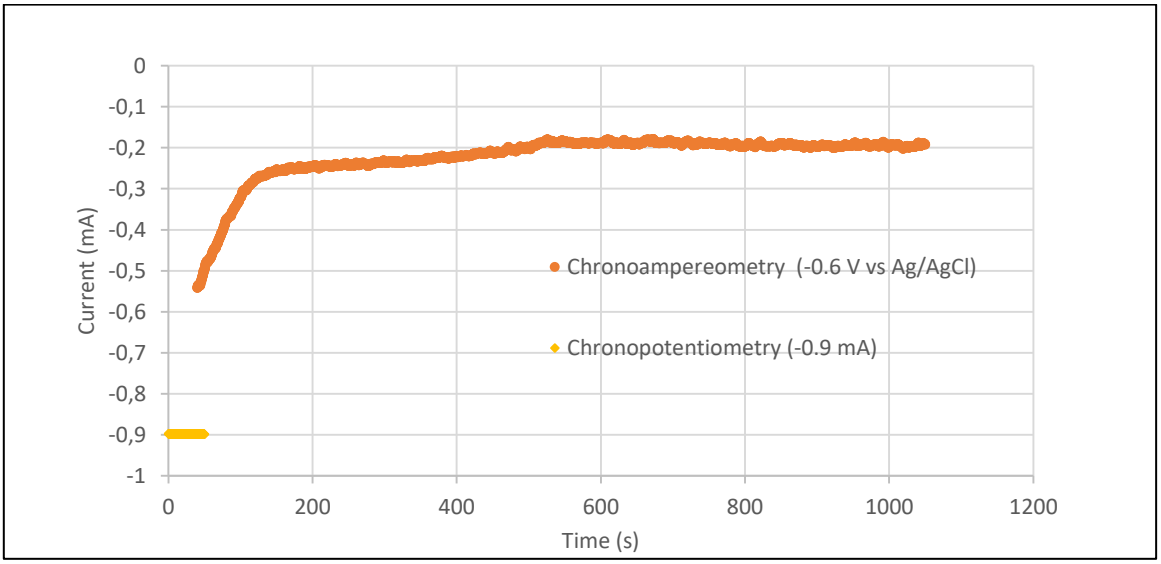

Figure 5. 20: Combined chronopotentiometry and chronoamperometry for the electrodeposition of Au nanowires

It was suspected that perhaps how the initial growth of the nanowire took place affected the morphology of the rest of the nanowire. So then if the initial nucleation phase was more controlled such that the nanowire could grow on a well formed based, the rest of the nanowire would be well formed. Based on this, it was decided to use chronopotentiometry initially, keeping the current magnitude low at -0.9 mA for 40 seconds. followed by chronoamperometry for the rest of the deposition at -0.6 V.

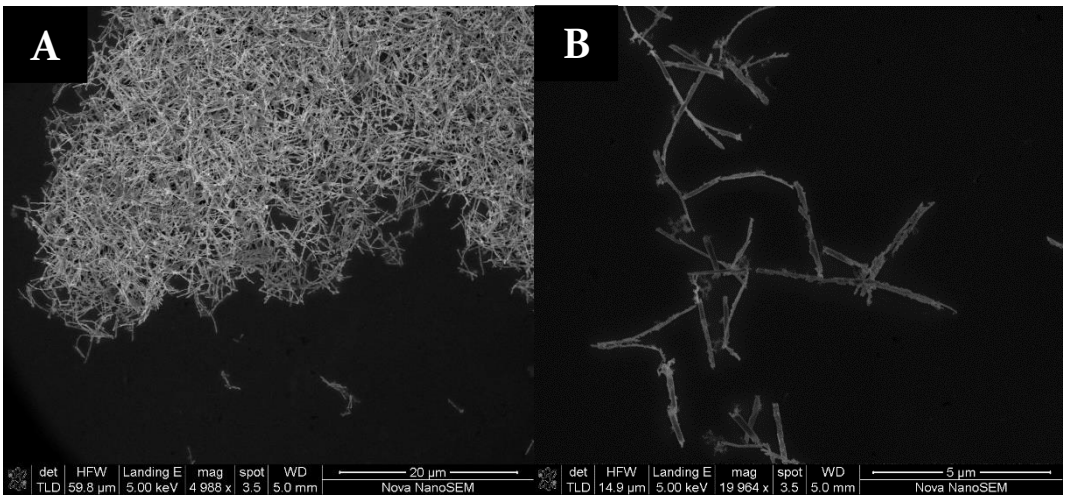

Figure 5. 21: SEM images of gold nanowires deposited using a combination of chronopotentiometry and chronoamperometry

Combining these potentiodynamic and potentiostatic electrodeposition techniques showed a definite improvement in the resulting nanowire morphology. It is observed throughout the SEM analysis that segments of the nanowires have conformed well to the cylindrical pore followed

by segments with a jagged and partially broken morphology. The former observation is suspected to be a result of using chronopotentiometry at low current deposition rates as it has not been observed with just chronoamperometry. With this result, chronopotentiometry was chosen as the preferred method to electrodeposit the Au nanowire segments.

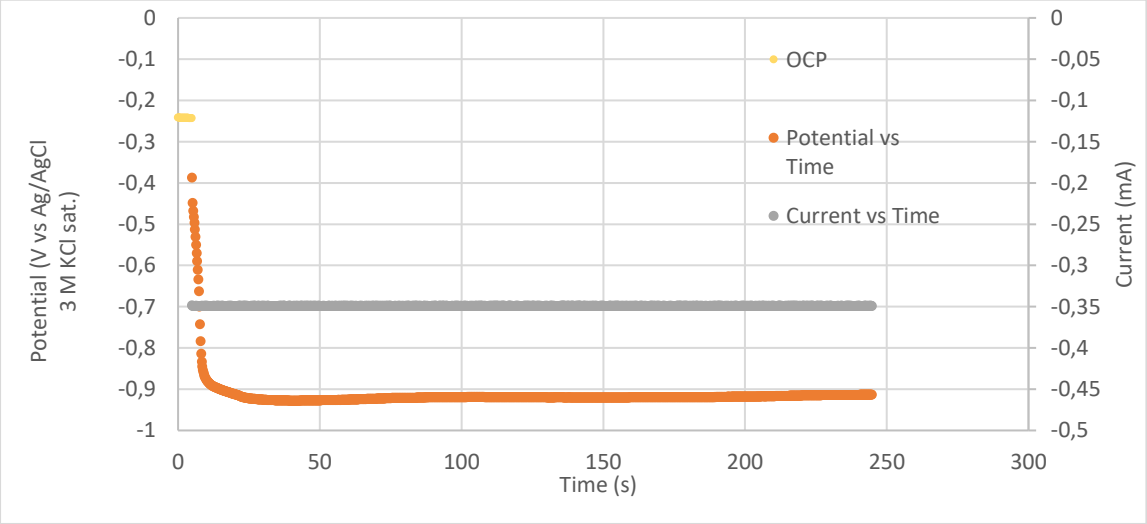

Figure 5. 22: Chronopotentiometry of Au nanowire segment in multi-segmented nanowires

Applying chronopotentiometry for Au electrodeposition was done at an even lower current of -0.35 mA for 250 s. This resulted in a relatively stable potential just lower than -0.9 V which could not be achieved using chronoamperometry. If a potential of -0.9 was applied during chronoamperometry, the resulting current would have been much higher than -0.35 mA in magnitude as seen from the high potential chronoamperometry shown in figure 5.10. Furthermore, the open circuit potential was also measured to gauge where the system starting point is and was found to be approximately -0.24 V vs Ag/AgCl.

5.3.4 Electrodeposition of Pt nanowires

chronopotentiometry was also adopted for the electrodeposition of Pt segments since the Au and Pt salt solutions are of a similar low concentrations concentration

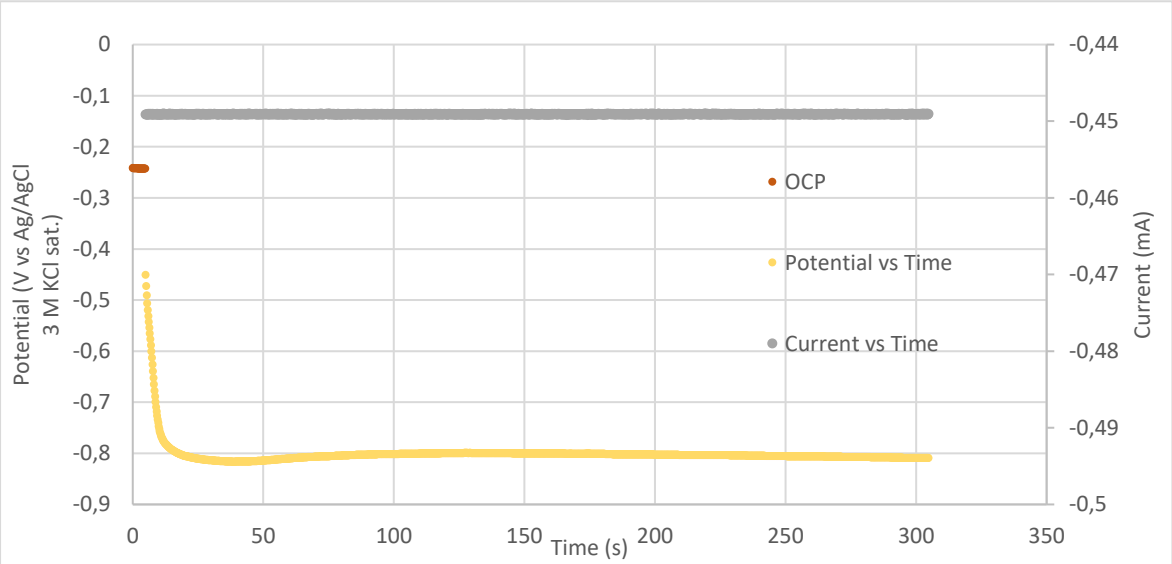

Figure 5. 23: Platinum chronopotentiometry at -0.45 mA

This was done at a current of -0.45 mA for just over 300 s as shown in Figure 5. 23. The potential response is similar to that seen for Au with an initial sharp drop in potential, then remaining fairly consistent. The steady state potential of Pt chronopotentiometry is approximately -0.8 V at -0.45 mA. The morphology of these deposits is shown in section 5.4 where multi-segmented nanowires were electrodeposited.

5.4: Electrodeposition of multi-segmented nanowires

Once the electrodeposition techniques for each semi-conductor and metal component was satisfactory, multi-segmented nanowires could be synthesised with more confidence. The electrodeposition parameters were selected based on the findings in the preceding sections 5.2 and 5.3. These parameters used for each segment are also summarised in Table 4.1.

5.4.1 SEM analysis of multi-segmented nanowires

Multi-segmented nanowires were looked at using SEM coupled with a backscatter detector and an EDX detector. Use of a backscatter detector for these materials allows the different metals to be identified giving a rough indication of size of each segment. This along with EDX was used to confirm the identity of the elements in different segments.

The SEM images presented in Figure 5. 24 show a group of complete multi-segmented nanowires in the order of CdSe/Ni/Au/Pt electrodeposited into 160 nm pores.

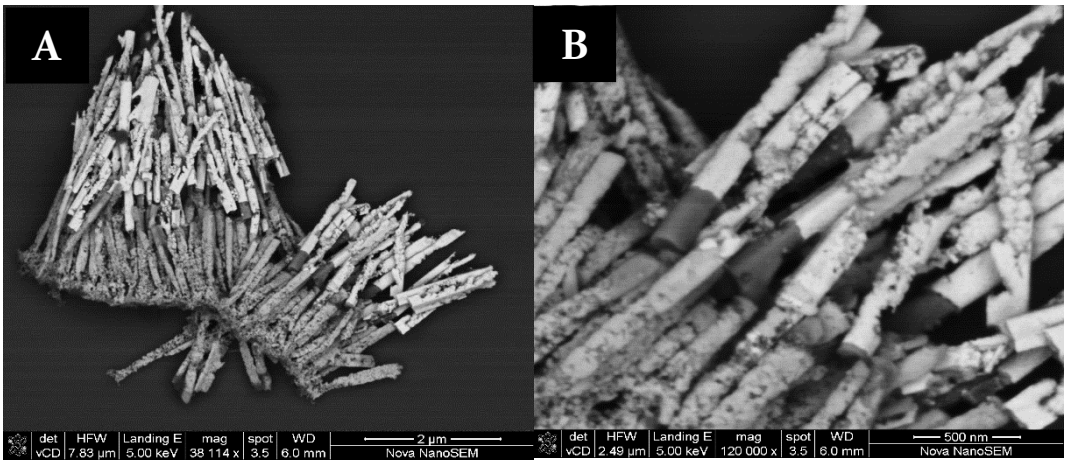

Figure 5. 24: Multi-segmented nanowires applying cyclic voltammetry for CdSe, Chronoamperometry for Ni and Chronopotentiometry for Au and Pt.

The images show that the morphology of Au and Pt segments have improved significantly in comparison to the images shown in Figure 5. 15 for example by conforming to the cylindrical pores. good contact between Ni, Au and Pt segments is also observed. This particular electrodeposition however shows poor contact between the semi-conducting CdSe segment and the rest of the pure metal segments. This along with the brittle appearance of the CdSe segment for this deposit and the reliability of the CdSe stoichiometry discussed previously highlights a few of the challenges associated with the template electrodeposition technique and defects that can affect the performance of the photocatalytic device when tested.

5.5: Fabrication of photocatalytic devices for testing

Insights obtained from the electrodepositions carried out in the preceding sections coupled with post electrodeposition annealing as well as the application of PEDOT:PSS as the protective anodic electrocatalyst allowed for fabrication of CdSe based photocatalytic devices. These key steps are emphasised here:

1) Electrodeposition of semi-conducting and metallic nanowires into AAO pores.

2) Annealing devices at 350 °C for 1 hr in Ar

3) Drop casting or spin coating of transparent conductive polymer PEDOT:PSS film as the anodic electrocatalyst.

Using this protocol, two photocatalytic devices were fabricated for testing with their electrodeposition plots being summarised in Figure 5. 26 & Figure 5. 26.The parameters regarding the electrodeposition of each device are kept the same, and the deposition times for each segment was kept much shorter to reduce overall nanowire length.

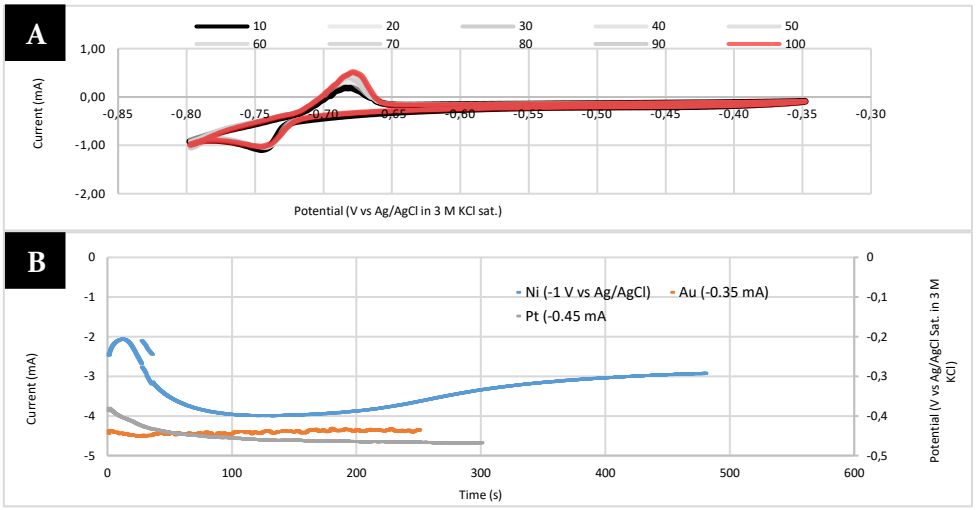

Figure 5. 25: Electrodeposition plots for device 1. [A] CdSe segment, [B] Ni, Au and Pt segments

To ensure reproducibility, each electrodeposition plot for each nanowire segment is compared. Similarity in shape, position of peaks and potential in the case of chronopotentiometry are observed before testing devices.

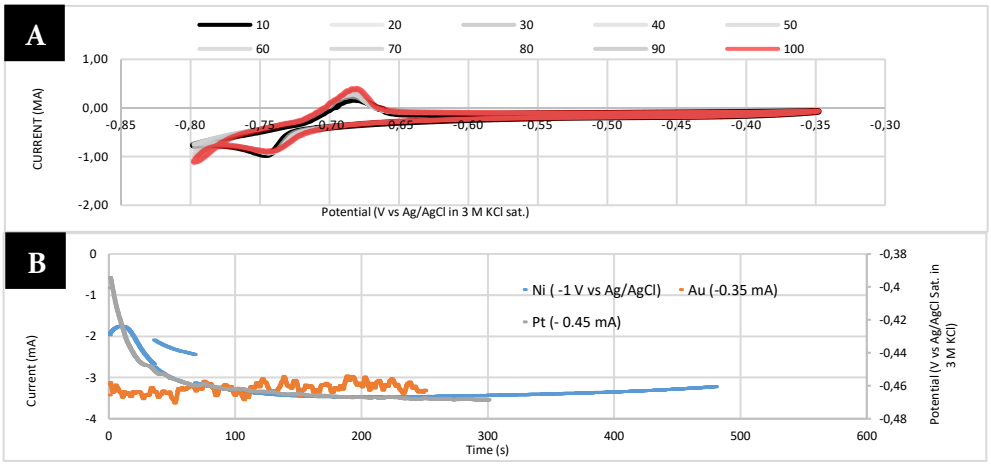

Figure 5. 26 Electrodeposition plots for device 2. [A] CdSe segment, [B] Ni, Au and Pt segments

It should be noted that exactly identical plots have never been achieved using this method, there have always been small variations to some degree for the same segments being deposited. This could be due to a range of factors such as contaminants, small variations in temperature, an uneven silver film having been deposited or use of a different potentiostat with different sensitivities.

After the electrodeposition of CdSe, Ni, Au and Pt, the photocatalytic device was annealed and PEDOT:PSS was drop casted and dried, completing the device fabrication for testing.

5.6: Photocatalytic testing

The first part of the results section deals with how templated electrodeposition is used as a synthesis technique for semi-conductor and metal nanowires, the characterisation thereof and how photocatalytic devices were fabricated. This second part deals with how these photocatalytic devices were tested for hydrogen production under illumination. The development of the method used is first presented followed by the results obtained from testing the 2 fabricated devices in an 80 % MeoH solution.

5.6.1 Photocatalytic Testing - Method Development

Development of a testing method to adequately gauge the activity of a photocatalyst is presented here. Testing the performance of non-particulate planar like photocatalyst is challenging for several reasons: These particular membranes are extremely fragile and need to be handled with great care, hence the photocatalyst cannot be exposed to even mild torsional or forces of compression. The orientation of the membrane should be such that the semi-conducting CdSe is being directly illuminated by the light source to ensure maximum light absorption. The membrane needs to be positioned upright and slightly slanted to allow gas evolution to take place on both sides. Due to the small amounts photocatalytic gases evolved, an inert carrier gas such as argon needs to be bubbled to displace bubbles off the surface of the photocatalyst. The reactor needs to be completely transparent to allow light to penetrate. The system needs to allow for easy sampling of a vapor space to determine which gases are being produced.

As far as it is known, there exists no commercially available testing system that takes all these requirements into account and a system needed to be designed and created from scratch. The design of this photoreactor and its external system was created with the intention of allowing for the proper reporting of photocatalytic activity as outlined by Chen *et al.* (2010) & Qureshi & Takanabe (2017).

Although the system was designed with this aim in mind, which is no trivial task. The first step in this work is to ensure that the system allows for the detection of hydrogen gas evolved from these photocatalytic devices. Once this is achieved further development of the system such as creating a photocatalytic standard as a benchmark can be considered.

5.6.1.1: Design and construction of a photo-reactor and testing system

A glass photo-reactor was designed and constructed to specifically test 13 mm diameter photocatalytic devices. The photo-reactor was created as outlined in the experimental methods.

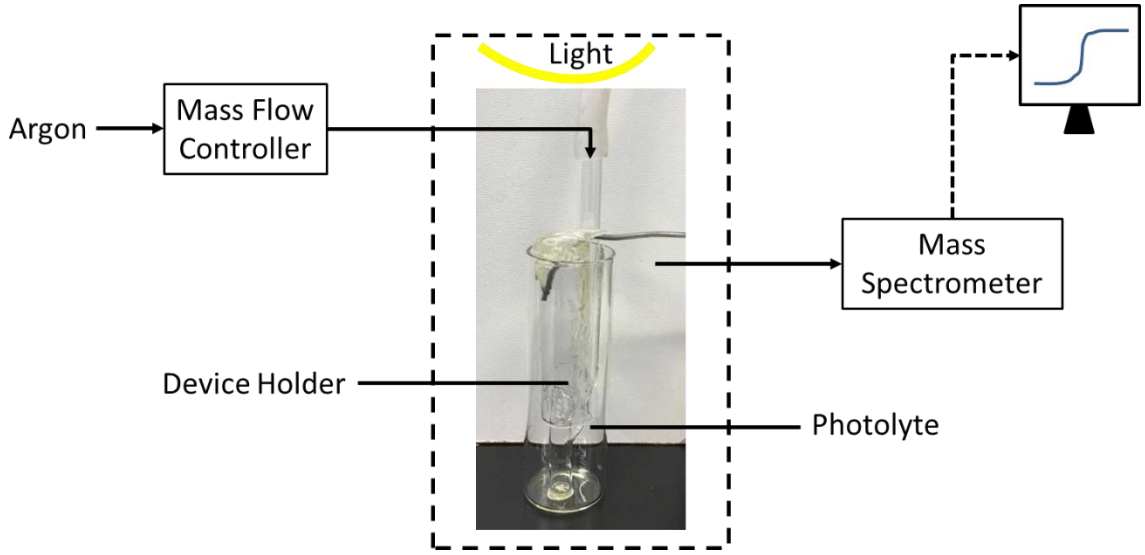

Figure 5. 27: Schematic of photocatalytic testing system

The photo-reactor and surrounding elements are displayed in figure 5.27. The photoreactor is kept in a closed space (dashed line) under the lens of the solar simulator.

A clamp is used to hold in place and slightly tilt the reactor. An argon line is connected to the bubbler and the flow is controlled using a mass flow controller between 2 and 5 ml/min calibrated using a bubble meter. The mass spectrometer is connected to the system by placing the glass around the device holder area such that a vapour space is created between the top surface of the solution and stainless-steel tube capillary. The vessel can then be filled with the

photolyte such that the photocatalytic device is sufficiently submerged. This is illustrated in Figure 5. 28.

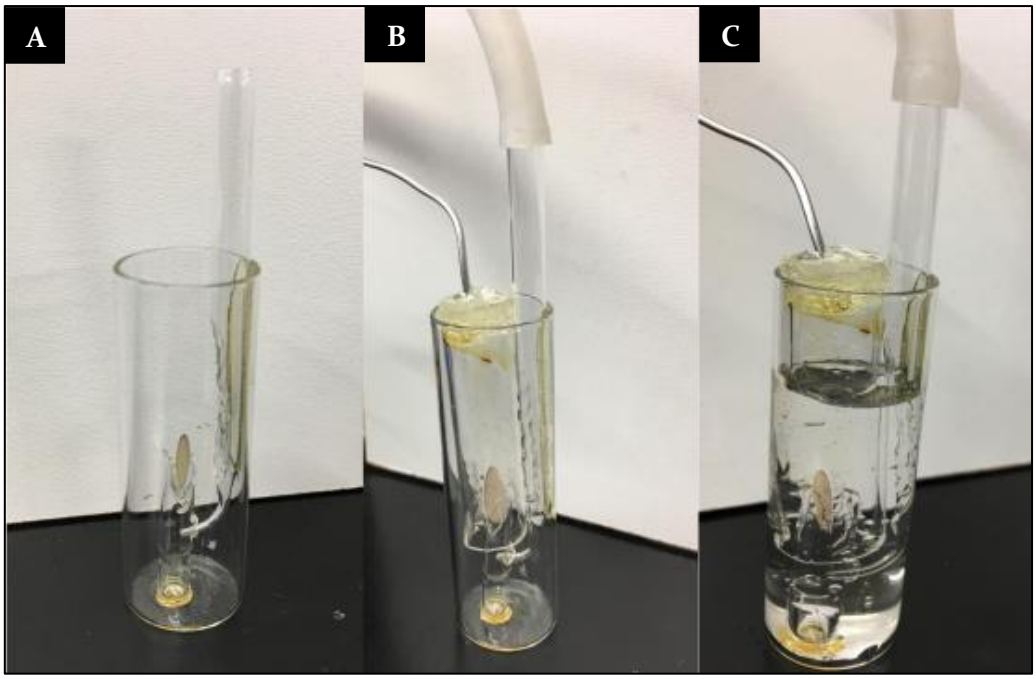

Figure 5. 28: Loading of photoreactor [A] 13 mm photocatalytic device inserted into holder. [B] glass sheath connected to M.S. and sealed with epoxy placed over holder & Ar gas line connected. [C] Testing electrolyte added, completely submerging the device.

5.6.1.2: Confirmation of hydrogen detection

To check that the mass spectrometer can indeed detect hydrogen, a solar-cell electrolyser connected to a 7 x 15 cm solar cell was used to produce hydrogen from pure water

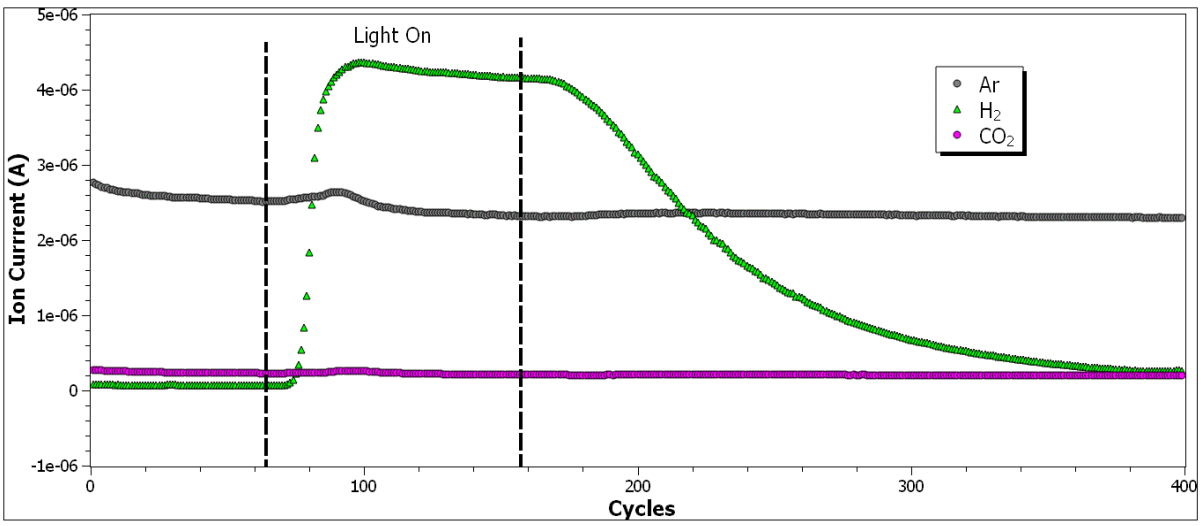

Figure 5. 29: Hydrogen detection using mass spectrometry and a solar-cell electrolyser

The solar cell was put under illumination at ambient conditions and the hydrogen outlet was connected directly to the mass spectrometer capillary.

The test had a positive outcome, indicating that the system was correctly set-up to detect hydrogen. Almost immediately after the light was turned on the hydrogen ion current spiked and shortly after the light was turned off the hydrogen ion current started to decline as indicated in Figure 5. 29. The delay in the response to the light is most likely due to the residence time within the capillary.

5.6.2 Devices tested in 80% MeOH

The following procedure was followed in testing each device and is also outlined in the experimental methods chapter:

The photocatalytic device is carefully inserted into the holder. The glass cover holding the mass spectrometer capillary inlet is placed over the device. The argon gas line is connected and the photoreactor is placed under the light. The correct orientation of the device towards the light must be ensured. The mass spectrometer valve is then opened and allowed to start measuring until a stable baseline has been obtained. Argon gas is then bubbled until the argon ion current reaches a steady state value. Once the Ar ion current has stabilised, the photolyte or testing electrolyte was added using a narrow nozzle directly into the photoreactor. Again the system is left to reach a steady state. The light is then turned on for 4 -5 minutes and subsequently turned off.

5.6.2.1: Device 1

The procedure described above was followed for device 1. The electrodeposition plots for this device was summarised in Figure 5. 25.

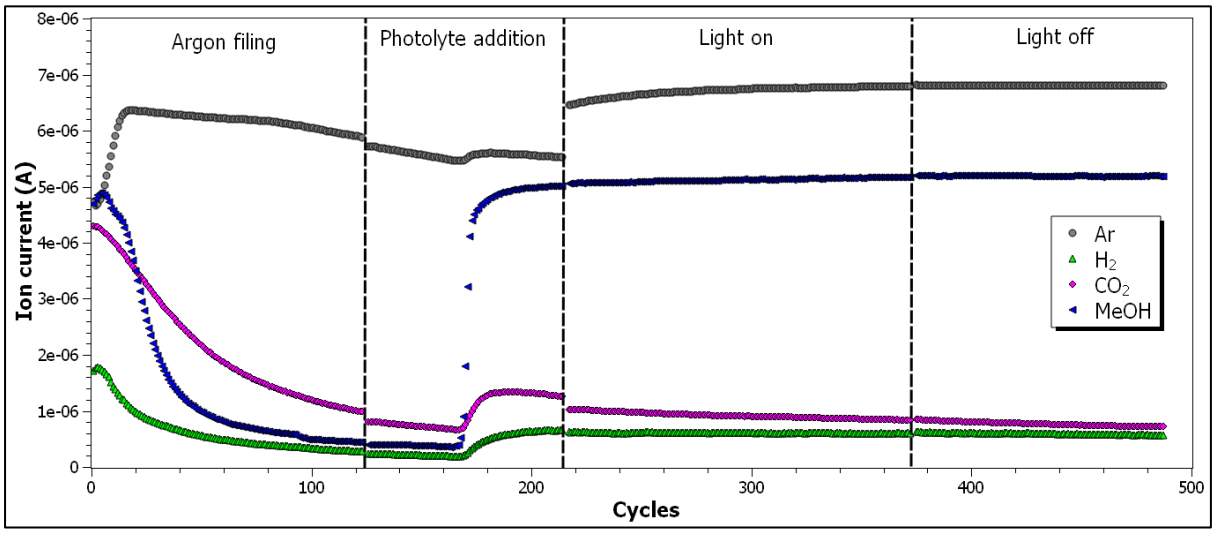

Figure 5. 30: Mass spectrometer ion current output for Device 1 tested in 80% MeOH

The mass spectrometer response to the addition of the photolyte is the most significant feature in Figure 5. 30. a few seconds after the photolyte is added. Spikes in the ion currents of H_2, CO_2 as well as MeOH are observed. This indicates that methanol oxidation occurs almost immediately upon contact between electrolyte and photocatalayst. This is in the absence of any applied irradiation meaning that the observed reaction most likely only a catalytic response as opposed to a photocatalytic one. This is plausible since the oxidation of alcohols in the presence of noble metals such as Pt is well known (Mallat & Baiker, 1994).

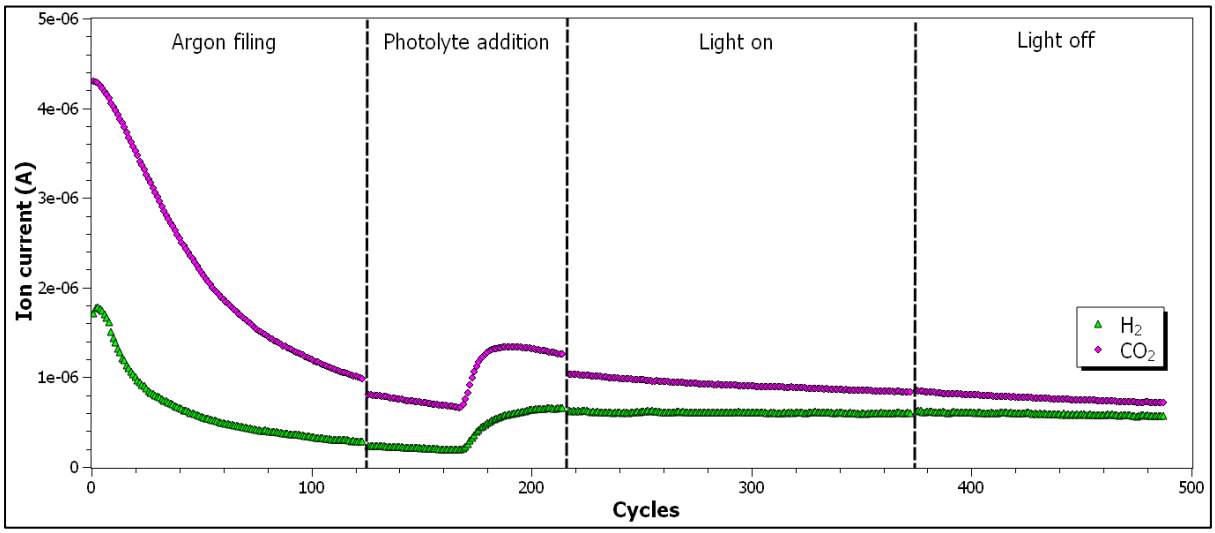

Figure 5. 31: Mass spectrometer output for Device 1 tested in 80% Methanol

The ion currents for hydrogen and carbon dioxide are almost six times lower than that of argon and methanol. It is therefore, from an activity point of view, more meaningful to observe the behaviour of these curves in response to the applied irradiation.

Figure 5. 31 both CO_2 and H_2 ion currents increase from their baselines upon methanol addition under no irradiation. For the duration of the irradiation however, no significant additional increase in ion current for both these species was observed. Furthermore, after irradiation had been stopped, no significant decrease in the ion currents were observed.

5.6.2.2: Device 2

The same procedure was used to test device 2 but initial ion current baselines were established for a longer period.

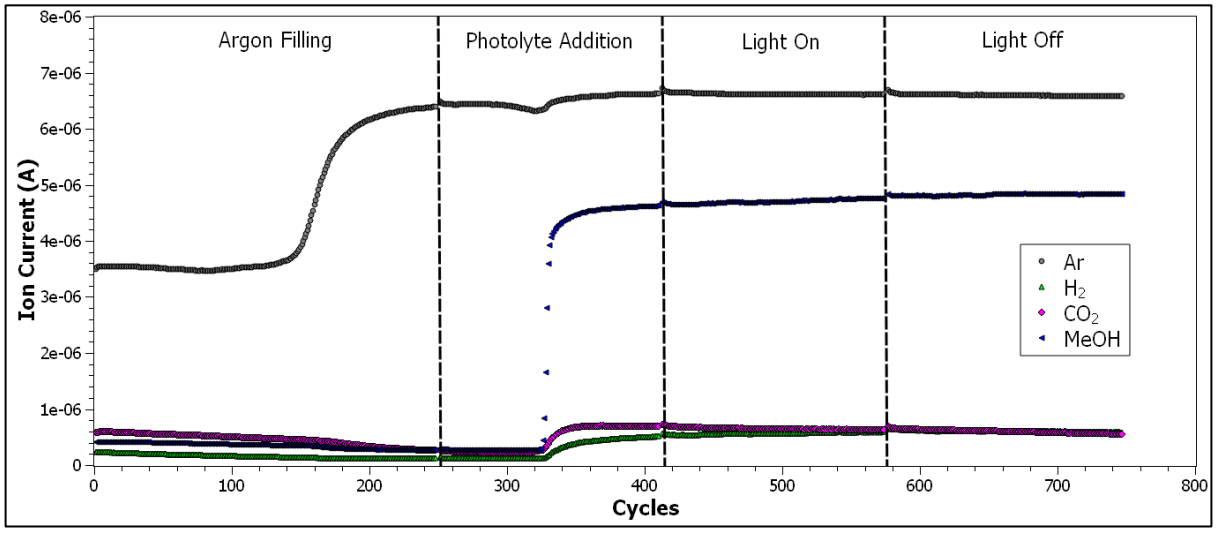

Figure 5. 32: Mass spectrometer output for device 2 tested in 80% MeOH

Addition of MeOH to the system without irradiation yielded the same response as seen for device 1, an immediate increase in the ion currents for H_2, CO_2 and MeOH, indicating catalytic methanol oxidation.

The behaviour of the H_2 and CO_2 ion current for device 2 is different to that of device 1. Upon irradiation the H_2 ion current continues to increase gradually while the CO_2 curve gradually decreases.

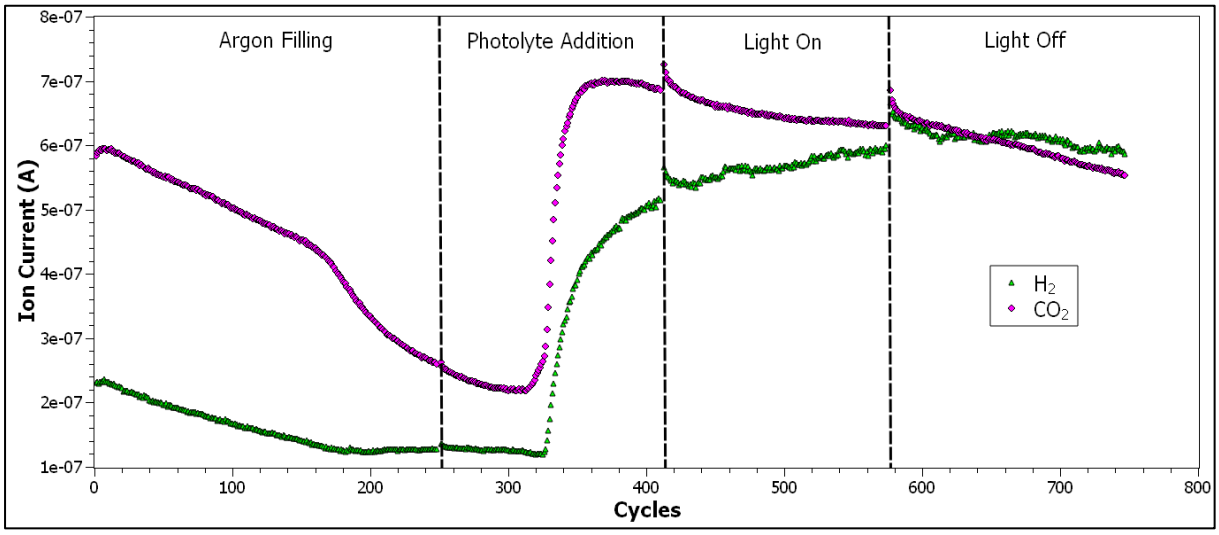

Figure 5. 33: Hydrogen and carbon dioxide ion currents for device 2 tested in 80% MeOH

When the irradiation is stopped, the ion current for both can be seen to decrease, The H_2 curve is also slightly rougher during irradiation than before irradiation had started. This could be an indication that the irradiation is driving some photocatalytic activity.

The electrodeposition curves for each segment of each device are comparable and both devices were subjected to the same annealing conditions and PEDOT:PSS polymer application. Be this as it may, device 1 showed no clear signs of being photo- active whereas device 2 gave a subtle

response to the applied irradiation with respect to the hydrogen ion current, indicating that small amounts of photocatalytic activity may have been present. Although this is not the most desirable result, it does bring up the issue of how catalytic activity should be decoupled from photocatalytic activity. This seems to be an important consideration for the case of testing in MeOH. At this point, testing in electrolytes that do not spontaneously react with any of the materials in the system seems like a reasonable way to isolate photocatalytic activity from catalytic activity. This could be done by testing in electrolytes containing effective inorganic hydrogen evolution promotors or hole scavengers such as Na_2S/Na_2SO_3 (Andrew Frame *et al.*, 2008; Commentary, 2013)

As for device 1 there are many reasons as to why it could be inactive, the most probably of which are:

1) Poor contact between the segments along the nanowire structure as seen in Figure 5. 24 resulting in an inability for charge to be separated properly.

2) Formation of Ag_5Cd_8 and Ag_2Se phases interfering with the process of light absorption

3) The ratio of Cd to Se being out of proportion in the CdSe segment of the nanowires.

4) A PEDOT:PSS layer that is too thick, hence not allowing light to reach photoactive CdSe

It may be of use for each completed device to be characterized before being tested. This however runs the risk of destroying the device completely and will make estimating the illuminated area difficult to determine if a piece of the device is broken off for further characterisation.

There is still a lot of work to be done towards the electrosynthesis of active photocatalytic devices of consistent quality given that the results obtained were could not show definitive photoactivity. What the results do however show is that gases evolved from these types of planar devices, even though not produced photo-catalytically were detected using online mass spectrometry and that the design of the photoreactor enabled these measurements to be made.

Although this does not y*et al*low for the proper reporting of photocatalytic activity since hydrogen evolution has only been detected and not measured. The configuration of the mass spectrometer system for the accurate measurement of hydrogen evolution would form part of the next step of this research in its context.

Chapter 6: Conclusions and Recommendations

Based on the preceding results and discussion thereof, and in relation to the objectives set and hypotheses made in chapter 3, the current chapter presents the conclusions drawn and recommendations made for future work.

6.1: Method development for the preparation of segmented nanowire devices

Segmented CdSe/Ni/Au/Pt nanowires were prepared using a template directed electrodeposition technique into both 200 nm and 160 nm AAO membrane pores. Photocatalytic devices for the intended purpose of photocatalytic hydrogen production were also prepared with segments PEDOT:PSS/CdSe/Ni/Au/Pt that was subjected to post-treatments such as annealing and treatment with organic acids.

Device preparation methodology was further developed from previous studies (Fawzy, 2016) by:

Making use of different AAO suppliers and carrying out electrodeposition of segmented nanowires in both 200 nm pores (Whatman®) and 160 nm pores (InRedox®).

- Thermal evaporation of Ag films was done at a rougher vacuum level of 2 x10^{-4} mbar allowing thermal evaporation to take less time as most of the time taken is waiting for the correct vacuum level to be reached.
- Modifications to the construction of working electrode using a glass slide and copper tape consisted of the use of nail varnish as an isolation material instead of tape. This improved the ease by which the AAO membrane was recovered post electrodeposition as they are extremely fragile.
- Exploring the XRD analysis of CdSe nanowires still embedded into the pores of the AAO membrane. The analysis was carried out before and after annealing at 350 °C for 1 hour in argon. The reference pattern of the unannealed CdSe nanowires corresponded well to pattern obtained but the XRD pattern obtained for the annealed CdSe nanowires was found to have been shifted. The same analysis did not seem to work inside the 160 nm pores.
- Chronopotentiometry was found to be an effective electrochemical technique to control the morphology of Au & Pt nanowire segments whereas jagged nanowire structures of these segments were obtained using chronoamperometry.

The cyclic electrodeposition of CdSe nanowires proved to be a lot more complicated than initially anticipated. Variations in the pores sizes as well as pore characteristics such as the interpore distances was suspected to significantly impact on the ratio between Cd and Se in the

solid nanowire. This was attributed to mass transport effects taking place during the electrodeposition process. There is a lot of scope to determine how mass transfer effects, affect the stoichiometry of CdSe nanowires in systems where pore characteristics change and is recommended for future investigation.

6.2: Design and creation of photoreactor for AAO membrane based photocatalyst devices

A fully transparent glass photoreactor was constructed that was able to function as a holder for the 13 mm diameter photocatalytic device as well the testing electrolyte and additionally allowed Ar to be bubbled at very low flow-rates to act as an agitator and carrier gas. The design enabled the AAO based photocatalytic device to stand vertically slanted with the photoactive segment faced to the light source while gases could be carried away upwards from both sides.

The design of this photoreactor enabled the detection of hydrogen gas evolved from these devices but cannot yet enable accurate hydrogen evolution rate measurements which are required for the proper reporting of photocatalytic performances. It is recommended that this task takes priority in future research in this area and be targeted specifically towards these planar membrane type devices. This will require the development of a standard photocatalytic material against which these devices can be benchmarked which is essential for further development of a testing system like this.

6.3: Set-up of an online hydrogen detection system for photocatalytic device testing.

A photocatalytic hydrogen detection testing system using online mass spectrometry was successfully set-up. The elements of this system are shown in figure 5.27 consisted of an Ar mass flow controller coupled to an electronic flow meter, A mass spectrometer linked to a computer, an SPI solar cell tester as the source of irradiation and the previously described photoreactor containing the photocatalyst material. The system did allow for the detection of hydrogen gas evolved, but it was unclear if the hydrogen was produced because of irradiation or not.

For hydrogen detection the mass spectrometer is run in MID mode allowing it to detect the ions of any specified ionic masses. Regardless of how much of it is being produced. MCD mode however allows the concentration of a species in the sampled gas to be obtained but, for it to be meaningful in this application, the flowrate into and out of the vapour space above the liquid where hydrogen is being evolved into must be carefully controlled. Additionally, this mode

requires further calibration regarding hydrogen. Once this is accomplished, more advanced and meaningful photocatalytic performance data can be measured such as efficiency like STH and quantum efficiencies, and specific activities such as μmol H_2 produced per hour.

References

Abanades, S., Charvin, P., Lemont, F. & Flamant, G. 2008. Novel two-step SnO2/SnO water-splitting cycle for solar thermochemical production of hydrogen. *International Journal of Hydrogen Energy*. 33(21):6021–6030. DOI: 10.1016/j.ijhydene.2008.05.042.

Abe, R. 2010. Recent progress on photocatalytic and photoelectrochemical water splitting under visible light irradiation. *Journal of Photochemistry and Photobiology C: Photochemistry Reviews*. 11(4):179–209. DOI: 10.1016/j.jphotochemrev.2011.02.003.

Ager, J.W., Shaner, M.R., Walczak, K.A., Sharp, I.D. & Ardo, S. 2015. Experimental Demonstrations of Spontaneous, Solar-Driven Photoelectrochemical Water Splitting. *Energy Environ. Sci.* 8:2811–2824. DOI: 10.1039/C5EE00457H.

Andrew Frame, F., Carroll, E.C., Larsen, D.S., Sarahan, M., Browning, N.D. & Osterloh, F.E. 2008. First demonstration of CdSe as a photocatalyst for hydrogen evolution from water under UV and visible light. *Chemical communications (Cambridge, England)*. (19):2206–2208. DOI: 10.1039/b718796c.

Artificial Photosynthesis: Solar Splitting of Water to Hydrogen and Oxygen. n.d. Available: http://pubs.acs.org/doi/pdf/10.1021/ar000051a007 [2016, February 03].

Bakenne, A., Nuttall, W. & Kazantzis, N. 2016. Sankey-Diagram-based insights into the hydrogen economy of today. *International Journal of Hydrogen Energy*. 41(19):7744–7753. DOI: 10.1016/j.ijhydene.2015.12.216.

Berr, M.J., Wagner, P., Fischbach, S., Vaneski, A., Schneider, J., Susha, A.S., Rogach, A.L., Jäckel, F., *et al*. 2012. Hole scavenger redox potentials determine quantum efficiency and stability of Pt-decorated CdS nanorods for photocatalytic hydrogen generation. *Applied Physics Letters*. 100(22):2–5. DOI: 10.1063/1.4723575.

Bolton, R. 1996. Solar photoproduction. *Science*. 57(1):37–50. DOI: 10.1016/0038-092X(96)00032-1.

Bouchy, M. & Zahraa, O. 2003. Photocatalytic reactors. *International Journal of Photoenergy*. 5(3):191–197. DOI: 10.1155/S1110662X03000321.

Carmo, M., Fritz, D.L., Mergel, J. & Stolten, D. 2013. A comprehensive review on PEM water electrolysis. *International Journal of Hydrogen Energy*. 38(12):4901–4934. DOI: 10.1016/j.ijhydene.2013.01.151.

Chen, X., Shen, S., Guo, L. & Mao, S.S. 2010. Semiconductor-based photocatalytic hydrogen generation. *Chemical Reviews*. 110(11):6503–6570. DOI: 10.1021/cr1001645.

Chen, Z., Jaramillo, T.F., Deutsch, T.G., Kleiman-Shwarsctein, A., Forman, A.J., Gaillard, N., Garland, R., Takanabe, K., *et al*. 2010. Accelerating materials development for photoelectrochemical hydrogen production: Standards for methods, definitions, and reporting protocols. *Journal of Materials Research*. 25(1):3–16. DOI: 10.1557/JMR.2010.0020.

Cheng, X., Shi, Z., Glass, N., Zhang, L., Zhang, J., Song, D., Liu, Z.S., Wang, H., *et al*. 2007. A review of PEM hydrogen fuel cell contamination: Impacts, mechanisms, and mitigation. *Journal of Power Sources*. 165(2):739–756. DOI: 10.1016/j.jpowsour.2006.12.012.

Cherevan, A.S., Gebhardt, P., Shearer, C.J., Matsukawa, M., Domen, K. & Eder, D. 2014. Interface engineering in nanocarbon–Ta 2 O 5 hybrid photocatalysts. *Energy Environ. Sci.* 7(2):791–796. DOI: 10.1039/C3EE42558D.

Chong, B., Zhu, W. & Hou, X. 2017. Epitaxial hetero-structure of CdSe/TiO 2 nanotube arrays with PEDOT as a hole transfer layer for photoelectrochemical hydrogen evolution. *Journal of Materials Chemistry A*. 5(13):6233–6244. DOI: 10.1039/C6TA10202F.

Commentary, G. 2013. Undesired Role of Sacri fi cial Reagents in Photocatalysis. *J. Phys. Chem. Lett.* 4:3479–3483. DOI: 10.1021/jz4018199.

Coronado, J.M., Fresno, F. & Portela, R. 2013. *Design of Advanced Photocatalytic Materials for Energy and Environmental Applications*. DOI: 10.1007/978-1-4471-5061-9.

Dhar, S., Majumder, T., Chakraborty, P. & Mondal, S.P. 2018. DMSO modified PEDOT:PSS polymer/ZnO nanorods Schottky junction ultraviolet photodetector: Photoresponse, external quantum efficiency, detectivity, and responsivity augmentation using N doped graphene quantum dots. *Organic Electronics*. 53(November 2017):101–110. DOI: 10.1016/j.orgel.2017.11.024.

Dincer, I. & Acar, C. 2014. Review and evaluation of hydrogen production methods for better sustainability. *International Journal of Hydrogen Energy*. 40(34):11094–11111. DOI: 10.1016/j.ijhydene.2014.12.035.

Döscher, H., Young, J.L., Geisz, J.F., Turner, J.A. & Deutsch, T.G. 2016. Solar-to-hydrogen efficiency: shining light on photoelectrochemical device performance. *Energy Environ. Sci.* 9(1):74–80. DOI: 10.1039/C5EE03206G.

Erbs, W., Desilvestro, J., Borgarello, E. & Graetzel, M. 1984. Visible-light-induced oxygen generation from aqueous dispersions of tungsten(VI) oxide. *The Journal of Physical Chemistry*.

88(18):4001–4006. DOI: 10.1021/j150662a028.

Escobedo, J.F., Gomes, E.N., Oliveira, A.P. & Soares, J. 2009. Modeling hourly and daily fractions of UV , PAR and NIR to global solar radiation under various sky conditions at Botucatu , Brazil. *Applied Energy*. 86(3):299–309. DOI: 10.1016/j.apenergy.2008.04.013.

Fabian, D.M., Hu, S., Singh, N., Houle, F.A., Hisatomi, T., Domen, K., Osterloh, F.E. & Ardo, S. 2015. Particle suspension reactors and materials for solar-driven water splitting. *Energy Environ. Sci.* 8(10):2825–2850. DOI: 10.1039/C5EE01434D.

Fawzy, M. 2016. Electrochemical Synthesis of Functional Nanowires.

Fox, M.A. & Dulay, M.T. 1993. Heterogeneous Photocatalysis. *Chemical Reviews*. 93(1):341–357. DOI: 10.1021/cr00017a016.

Fujishima, A. & Honda, K. 1972a. Photolysis-decomposition of water at the surface of an irradiated semiconductor. *Nature*. 238(5385):37–38.

Fujishima, A. & Honda, K. 1972b. Electrochemical photolysis of water at a semiconductor electrode. *Nature*. 238(5358):37–38. DOI: 10.1038/238037a0.

Goto, Y., Hisatomi, T., Wang, Q., Takata, T., Yamada, T., Domen, K., Higashi, T., Ishikiriyama, K., *et al*. 2017. A Particulate Photocatalyst Water-Splitting Panel for Large-Scale Solar Hydrogen Generation. *Joule*. 2:1–12. DOI: 10.1016/j.joule.2017.12.009.

Guo, M., Wang, L., Xia, Y., Huang, W. & Li, Z. 2016. Fabrication of nano-CdSe thin films from gas/liquid interface reactions and self-assembly for photoelectrochemical hydrogen production. *International Journal of Hydrogen Energy*. 41(4):2278–2284. DOI: 10.1016/j.ijhydene.2015.12.080.

Habouti, S., Mátéfi-Tempfli, M., Solterbeck, C.H., Es-Souni, M., Mátéfi-Tempfli, S. & Es-Souni, M. 2011. On-substrate, self-standing Au-nanorod arrays showing morphology controlled properties. *Nano Today*. 6(1):12–19. DOI: 10.1016/j.nantod.2010.11.001.

Harriman, a. 1985. *Photoelectrochemistry, Photocatalysis and Photoreactors*. V. 38. M. Schiavello, Ed. Dordrecht: Springer Netherlands. DOI: 10.1007/978-94-015-7725-0.

Holladay, J.D., Hu, J., King, D.L. & Wang, Y. 2009. An overview of hydrogen production technologies. *Catalysis Today*. 139(4):244–260. DOI: 10.1016/j.cattod.2008.08.039.

Holmes, M.A., Townsend, T.K. & Osterloh, F.E. 2012. Quantum confinement controlled photocatalytic water splitting by suspended CdSe nanocrystals. *Chemical communications*

(Cambridge, England). 48(3):371–3. DOI: 10.1039/c1cc16082f.

Hurst, S.J., Payne, E.K., Qin, L. & Mirkin, C.A. 2006. Multisegmented one-dimensional nanorods prepared by hard-template synthetic methods. *Angewandte Chemie - International Edition*. 45(17):2672–2692. DOI: 10.1002/anie.200504025.

Hwang, D.W., Kim, H.G., Jang, J.S., Bae, S.W., Ji, S.M. & Lee, J.S. 2004. Photocatalytic decomposition of water–methanol solution over metal-doped layered perovskites under visible light irradiation. *Catalysis Today*. 93–95:845–850. DOI: 10.1016/j.cattod.2004.06.084.

Ikekawa, A., Kamiya, M., Fujita, Y. & Kwan, T. 1964. On the Competition of Homogeneous and Heterogeneous Chain Terminations in Heterogeneous Photooxidation Catalysis by Zinc Oxide By Akiko IKEKAWA , Mamoru KAMIYA , Yuzaburo FUJITA and Takao KWAN (Received June 12 , 1964) It has previously1) been shown th. (1959):32–36.

Ismail, A.A. & Bahnemann, D.W. 2014. Photochemical splitting of water for hydrogen production by photocatalysis: A review. *Solar Energy Materials and Solar Cells*. 128:85–101. DOI: 10.1016/j.solmat.2014.04.037.

Ismail, A.A., Bahnemann, D.W., Fawzy, M., He, Z., Jie, J., Zhang, W.W., Zhang, W.W., Luo, L., *et al*. 2009. Remote sensing by plasmonic transport. *Journal of the American Chemical Society*. 4(2):743. DOI: 10.1021/ja3046662.

Iwase, A., Ng, Y.H., Ishiguro, Y., Kudo, A. & Amal, R. 2011. Reduced Graphene Oxide as a Solid-State Electron Mediator in Z-Scheme Photocatalytic Water Splitting under Visible Light. *Journal of the American Chemical Society*. 133(29):11054–11057. DOI: 10.1021/ja203296z.

Jäckle, S., Liebhaber, M., Gersmann, C., Mews, M., Jäger, K., Christiansen, S. & Lips, K. 2017. Potential of PEDOT:PSS as a hole selective front contact for silicon heterojunction solar cells. *Scientific reports*. 7(1):2170. DOI: 10.1038/s41598-017-01946-3.

Jie, J., Zhang, W., Bello, I., Lee, C.S. & Lee, S.T. 2010. One-dimensional II-VI nanostructures: Synthesis, properties and optoelectronic applications. *Nano Today*. 5(4):313–336. DOI: 10.1016/j.nantod.2010.06.009.

Joo, J., Son, J.S., Kwon, S.G., Yu, J.H. & Hyeon, T. 2006. Low-temperature solution-phase synthesis of quantum well structured CdSe nanoribbons. *Journal of the American Chemical Society*. 128(17):5632–5633. DOI: 10.1021/ja0601686.

Kato, H. & Kudo, A. 2002. Visible-Light-Response and Photocatalytic Activities of TiO 2 and SrTiO 3 Photocatalysts Codoped with Antimony and Chromium. *The Journal of Physical*

Chemistry B. 106(19):5029–5034. DOI: 10.1021/jp0255482.

Kato, H., Asakura, K. & Kudo, A. 2003. Highly Efficient Water Splitting into H2 and O2 over Lanthanum-Doped NaTaO3 Photocatalysts with High Crystallinity and Surface Nanostructure. *Journal of the American Chemical Society*. 125(10):3082–3089. DOI: 10.1021/ja027751g.

Kibria, M.G., Zhao, S., Chowdhury, F.A., Wang, Q., Nguyen, H.P.T., Trudeau, M.L., Guo, H. & Mi, Z. 2014. Tuning the surface Fermi level on p-type gallium nitride nanowires for efficient overall water splitting. *Nature Communications*. 5. DOI: 10.1038/ncomms4825.

Kim, H., Seol, M., Lee, J. & Yong, K. 2011. Highly Efficient Photoelectrochemical Hydrogen Generation Using Hierarchical ZnO / WOx Nanowires Cosensitized with CdSe / CdS. *The Journal of Physical Chemistry C*. 115:25429–25436. DOI: 10.1021/jp2093115.

Kim, Y., Jung, J., Kim, S. & Chae, W. 2013. Cyclic Voltammetric and Chronoamperometric Deposition of CdS. 54(8):1467–1472.

Klein, J.D., Ii, R.D.H., Palmer, D., Sailor, M.J., Brumlik, C.J. & Martin, C.R. 1993. Electrochemical fabrication of cadmium chalcogenide microdiode arrays. *Chemistry of Materials*. 5(36):902–904. DOI: 10.1021/cm000031a002.

Kressin, A.M., Doan, V. V., Klein, J.D. & Sailor, M.J. 1991. Synthesis of stoichiometric cadmium selenide films via sequential monolayer electrodeposition. *Chemistry of Materials*. 3(6):1015–1020. DOI: 10.1021/cm00018a014.

Kroschwitz, J.I. & Nees, F. 1995. Kirk/Othmer Encyclopedia of Chemical Technology, Vols. 3-10. *Angewandte Chemie-English Edition*. 34(22):2564.

Kudo, A. & Kato, H. 2000. Effect of lanthanide-doping into NaTaO3 photocatalysts for efficient water splitting. *Chemical Physics Letters*. 331(5–6):373–377. DOI: 10.1016/S0009-2614(00)01220-3.

Kudo, A. & Miseki, Y. 2009. Heterogeneous photocatalyst materials for water splitting. *Chemical Society reviews*. 38(1):253–278. DOI: 10.1039/b800489g.

Kumar, S., Kumar, V., Sharma, S.K., Sharma, S.K. & Chakarvarti, S.K. 2010. Large scale synthesis of cadmium selenide nanowires using template synthesis technique and their characterization. *Superlattices and Microstructures*. 48(1):66–71. DOI: 10.1016/j.spmi.2010.03.008.

Laboratories, B. & Hill, M. 1980. Electrodeposition of CdSe Films from Selenosulfite Solution. 2378–2381.

Lai, M. & Riley, D.J. 2008. Templated electrosynthesis of nanomaterials and porous structures.

Journal of Colloid and Interface Science. 323(2):203–212. DOI: 10.1016/j.jcis.2008.04.054.

Lee, J.S. 2005. Photocatalytic water splitting under visible light with particulate semiconductor catalysts. *Catalysis Surveys from Asia*. 9(4):217–227. DOI: 10.1007/s10563-005-9157-0.

Lewis, N.S. & Nocera, D.G. 2006. Powering the planet: Chemical challenges in solar energy utilization. *Proceedings of the National Academy of Sciences*. 103(43):15729–15735. DOI: 10.1073/pnas.0603395103.

Li, X., Yu, J., Low, J., Fang, Y., Xiao, J. & Chen, X. 2015. Engineering heterogeneous semiconductors for solar water splitting. *J. Mater. Chem. A*. 3(6):2485–2534. DOI: 10.1039/C4TA04461D.

Lin, Y., Zhang, K., Chen, W., Liu, Y., Geng, Z., Zeng, J., Pan, N., Yan, L., *et al*. 2010. Dramatically Enhanced Photoresponse of Free Anchored CdSe Nanoparticles. *ACS nano*. 4(6):3033–3038. DOI: 10.1021/nn100134j.

Logan, B.E. 2004. Peer Reviewed: Extracting Hydrogen and Electricity from Renewable Resources. *Environmental Science & Technology*. 38(9):160A–167A. DOI: 10.1021/es040468s.

Maeda, K., Higashi, M., Lu, D., Abe, R. & Domen, K. 2010. Efficient Nonsacrificial Water Splitting through Two-Step Photoexcitation by Visible Light using a Modified Oxynitride as a Hydrogen Evolution Photocatalyst. *Journal of the American Chemical Society*. 132(16):5858–5868. DOI: 10.1021/ja1009025.

Mallat, T. & Baiker, A. 1994. Oxidation of alcohols with molecular oxygen on platinum metal catalysts in aqueous solutions. *Catalysis Today*. 19(2):247–283. DOI: 10.1016/0920-5861(94)80187-8.

Mangrulkar, P.A., Polshettiwar, V., Labhsetwar, N.K., Varma, R.S. & Rayalu, S.S. 2012. Nano-ferrites for water splitting: unprecedented high photocatalytic hydrogen production under visible light. *Nanoscale*. 4(16):5202–5209. DOI: 10.1039/C2NR30819C.

Meissner, D., Memming, R., Kastening, B. & Bahnemann, D. 1986. Fundamental problems of water splitting at cadmium sulfide. *Chemical Physics Letters*. 127(5):419–423. DOI: 10.1016/0009-2614(86)80583-8.

Montoya, J.H., Seitz, L.C., Chakthranont, P., Vojvodic, A., Jaramillo, T.F. & Nørskov, J.K. 2016. Materials for solar fuels and chemicals. *Nature Materials*. 16(1):70–81. DOI: 10.1038/nmat4778.

Motegh, M. 2013. Design of Photocatalytic Reactors. DOI: 10.4233/uuid:8e9ed02f-2fee-4613-

8d85-4ed12b54fa52.

Mubeen, S., Singh, N., Lee, J., Stucky, G.D., Moskovits, M. & McFarland, E.W. 2013. Synthesis of chemicals using solar energy with stable photoelectrochemically active heterostructures. *Nano Letters*. 13(5):2110–2115. DOI: 10.1021/nl400502u.

Muradov, N. 2003. Emission-free fuel reformers for mobile and portable fuel cell applications. 118:320–324. DOI: 10.1016/S0378-7753(03)00078-8.

Navarro Yerga, R.M., Consuelo ??lvarez Galv??n, M., del Valle, F., Villoria de la Mano, J.A. & Fierro, J.L.G. 2009. Water splitting on semiconductor catalysts under visiblelight irradiation. *ChemSusChem*. 2(6):471–485. DOI: 10.1002/cssc.200900018.

Ni, M., Leung, M. & Leung, D. 2007. Energy and exergy analysis of hydrogen production by solid oxide steam electrolyzer plant. *International Journal of Hydrogen Energy*. 32(18):4648–4660. DOI: 10.1016/j.ijhydene.2007.08.005.

"Ni ve rs ity ap e To w n ve rs ity of e To w". n.d.

Nikolaidis, P. & Poullikkas, A. 2017. A comparative overview of hydrogen production processes. *Renewable and Sustainable Energy Reviews*. 67:597–611. DOI: 10.1016/j.rser.2016.09.044.

Nozik, A.J. 1977. Photochemical diodes. *Applied Physics Letters*. 30(11):567–569. DOI: 10.1063/1.89262.

Orhan, M., Dincer, I. & Rosen, M. 2008. Energy and exergy assessments of the hydrogen production step of a copper–chlorine thermochemical water splitting cycle driven by nuclear-based heat. *International Journal of Hydrogen Energy*. 33(22):6456–6466. DOI: 10.1016/j.ijhydene.2008.08.035.

Ouyang, J. 2013. Solution-Processed PEDOT : PSS Films with Conductivities as Indium Tin Oxide through a Treatment with Mild and Weak Organic Acids. DOI: 10.1021/am404113n.

Pena, D.J., Mbindyo, J.K.N., Carado, A.J., Mallouk, T.E., Keating, C.D., Razavi, B., Mayer, T.S., Park, U. V, *et al*. 2002. Template Growth of Photoconductive Metal - CdSe - Metal Nanowires. *Journal of Physical Chemistry*. 106:7458–7462. DOI: 10.1021/jp0256591.

Peña, D.J., Mbindyo, J.K.N., Carado, A.J., Mallouk, T.E., Keating, C.D., Razavi, B. & Mayer, T.S. 2002. Template growth of photoconductive metal-CdSe-metal nanowires. *Journal of Physical Chemistry B*. 106(30):7458–7462. DOI: 10.1021/jp0256591.

Possin, G.E. 1970. A Method for Forming Very Small Diameter Wires. 772:3–6. DOI:

10.1063/1.1684640.

Preethi, V. & Kanmani, S. 2013. Photocatalytic hydrogen production. *Materials Science in Semiconductor Processing*. 16(3):561–575. DOI: 10.1016/j.mssp.2013.02.001.

Qureshi, M. & Takanabe, K. 2017. Insights on Measuring and Reporting Heterogeneous Photocatalysis: Efficiency Definitions and Setup Examples. *Chemistry of Materials*. 29(1):158–167. DOI: 10.1021/acs.chemmater.6b02907.

Rao, C.R.K. & Trivedi, D.C. 2005. Chemical and electrochemical depositions of platinum group metals and their applications. *Coordination Chemistry Reviews*. 249(5–6):613–631. DOI: 10.1016/j.ccr.2004.08.015.

Riordan, C. & Hulstron, R. 1990. What is an air mass 1.5 spectrum? (solar cell performance calculations). In *IEEE Conference on Photovoltaic Specialists*. IEEE. 1085–1088. DOI: 10.1109/PVSC.1990.111784.

Sabate, J., Cervera-March, S., Simarro, R. & Gimi~Nez, J. 1990. a Comparative Study of Semiconductor Photocatalysts for H Y Drogen Production By Visible Light Using Different Sacrificial. *International Association for Hydrogen Energy*. 15(2):115–124.

Sahu, N., Upadhyay, S. & Sinha, A. 2009. Kinetics of reduction of water to hydrogen by visible light on alumina supported Pt–CdS photocatalysts. *International Journal of Hydrogen Energy*. 34(1):130–137. DOI: 10.1016/j.ijhydene.2008.09.043.

Schierhorn, M., Boettcher, S.W., Kraemer, S., Stucky, G.D. & Moskovits, M. 2009. Photoelectrochemical performance of cdse nanorod arrays grown on a transparent conducting substrate. *Nano Letters*. 9(9):3262–3267. DOI: 10.1021/nl901522b.

Serpone, N., Emeline, A. V., Horikoshi, S., Kuznetsov, V.N. & Ryabchuk, V.K. 2012. On the genesis of heterogeneous photocatalysis: a brief historical perspective in the period 1910 to the mid-1980s. *Photochemical & Photobiological Sciences*. 11(7):1121. DOI: 10.1039/c2pp25026h.

Sharma, S. & Ghoshal, S.K. 2015. Hydrogen the future transportation fuel: From production to applications. *Renewable and Sustainable Energy Reviews*. 43:1151–1158. DOI: 10.1016/j.rser.2014.11.093.

Shimodaira, Y., Kato, H., Kobayashi, H. & Kudo, A. 2006. Photophysical Properties and Photocatalytic Activities of Bismuth Molybdates under Visible Light Irradiation. *The Journal of Physical Chemistry B*. 110(36):17790–17797. DOI: 10.1021/jp0622482.

Shpaisman, N. & Givan, Uri Patolsky, F. 2010. Electrochemical Synthesis of morphology controlled segmented CdSe. 4(4):1901–1906. DOI: 10.1149/1.2129814.

Spasiano, D., Marotta, R., Malato, S., Fernandez-Iba??ez, P. & Di Somma, I. 2015. Solar photocatalysis: Materials, reactors, some commercial, and pre-industrialized applications. A comprehensive approach. *Applied Catalysis B: Environmental*. 170–171:90–123. DOI: 10.1016/j.apcatb.2014.12.050.

Sreedhar, G., Sivanantham, A., Venkateshwaran, S., Panda, S.K. & Eashwar, M. 2015. Enhanced photoelectrochemical performance of CdSe quantum dot sensitized SrTiO 3. *J. Mater. Chem. A*. 3(25):13476–13482. DOI: 10.1039/C5TA00304K.

Stiegel, G.J. & Ramezan, M. 2006. Hydrogen from coal gasification: An economical pathway to a sustainable energy future. *International Journal of Coal Geology*. 65(3–4):173–190. DOI: 10.1016/j.coal.2005.05.002.

Su, R., Tiruvalam, R., Logsdail, A.J., He, Q., Downing, C.A., Jensen, M.T., Dimitratos, N., Kesavan, L., *et al*. 2014. Designer Titania-Supported Au–Pd Nanoparticles for Efficient Photocatalytic Hydrogen Production. *ACS Nano*. 8(4):3490–3497. DOI: 10.1021/nn500963m.

Sun, K., Zhang, S., Li, P., Xia, Y., Zhang, X., Du, D., Isikgor, F.H. & Ouyang, J. 2015. Review on application of PEDOTs and PEDOT:PSS in energy conversion and storage devices. *Journal of Materials Science: Materials in Electronics*. 26(7):4438–4462. DOI: 10.1007/s10854-015-2895-5.

Sun, S., Hisatomi, T., Wang, Q., Chen, S., Ma, G., Liu, J., Nandy, S., Minegishi, T., *et al*. (in press). Efficient Redox-Mediator-Free Z-scheme Water Splitting Employing Oxysulfide Photocatalysts under Visible Light. *ACS Catalysis*. acscatal.7b03884. DOI: 10.1021/acscatal.7b03884.

Tada, H., Mitsui, T., Kiyonaga, T., Akita, T. & Tanaka, K. 2006. All-solid-state Z-scheme in CdS–Au–TiO2 three-component nanojunction system. *Nature Materials*. 5(10):782–786. DOI: 10.1038/nmat1734.

Tanaka, D., Oaki, Y. & Imai, H. 2010. Enhanced photocatalytic activity of quantum-confined tungsten trioxide nanoparticles in mesoporous silica. *Chemical Communications*. 46(29):5286. DOI: 10.1039/cocc00540a.

Uchihara, T., Matsumura, M., Ono, J. & Tsubomura, H. 1990. Effect of EDTA on the photocatalytic activities and flatband potentials of cadmium sulfide and cadmium selenide. *The Journal of Physical Chemistry*. 94(1):415–418. DOI: 10.1021/j100364a069.

Wagner, F.T. & Somorjai, G.A. 1980. Photocatalytic and photoelectrochemical hydrogen

production on strontium titanate single crystals. *Journal of the American Chemical Society*. 102(17):5494–5502. DOI: 10.1021/ja00537a013.

Wang, M., Wang, Z., Gong, X. & Guo, Z. 2014. The intensification technologies to water electrolysis for hydrogen production - A review. *Renewable and Sustainable Energy Reviews*. 29:573–588. DOI: 10.1016/j.rser.2013.08.090.

Wang, P., Schwertmann, L., Marschall, R. & Wark, M. 2014. Tetragonal tungsten bronze-type nanorod photocatalysts with tunnel structures: Ta substitution for Nb and overall water splitting. *J. Mater. Chem. A*. 2(23):8815–8822. DOI: 10.1039/C4TA01393J.

Wu, K., Chen, Z., Lv, H., Zhu, H., Hill, C.L. & Lian, T. 2014. Hole removal rate limits photodriven H2 generation efficiency in CdS-Pt and CdSe/CdS-Pt semiconductor nanorod-metal tip heterostructures. *Journal of the American Chemical Society*. 136(21):7708–7716. DOI: 10.1021/ja5023893.

Xia, Y., Sun, K. & Ouyang, J. 2012. Solution-processed metallic conducting polymer films as transparent electrode of optoelectronic devices. *Advanced Materials*. 24(18):2436–2440. DOI: 10.1002/adma.201104795.

Xu, D., Shi, X., Guo, G., Gui, L. & Tang, Y. 2000. Electrochemical Preparation of CdSe Nanowire Arrays. 5061–5063.

Xu, Y., Huang, Y. & Zhang, B. 2016. Rational Design of Semiconductor-based Photocatalysts for Advanced Photocatalytic Hydrogen Production: the Case of Cadmium Chalcogenides. *Inorg. Chem. Front.* DOI: 10.1039/C5QI00217F.

Yanagida, S., Ogata, T., Shindo, A., Hosokawa, H., Mori, H., Sakata, T. & Wada, Y. 1995. Semiconductor Photocatalysis: Size Control of Surface-Capped CdS Nanocrystallites and the Quantum Size Effect in Their Photocatalysis. *Bulletin of the Chemical Society of Japan*. 68(3):752–758. DOI: 10.1246/bcsj.68.752.

Yao, W. & Ye, J. 2008. A new efficient visible-light-driven photocatalyst Na0.5Bi1.5VMoO8 for oxygen evolution. *Chemical Physics Letters*. 450(4–6):370–374. DOI: 10.1016/j.cplett.2007.11.045.

Yildiz, B. & Kazimi, M. 2006. Efficiency of hydrogen production systems using alternative nuclear energy technologies. *International Journal of Hydrogen Energy*. 31(1):77–92. DOI: 10.1016/j.ijhydene.2005.02.009.

Yu, B., Zhang, W., Xu, J., Chen, J., Luo, X. & Stephan, K. 2012. Preparation and electrochemical behavior of dense YSZ film for SOEC. *International Journal of Hydrogen Energy*. 37(17):12074–

12080. DOI: 10.1016/j.ijhydene.2012.05.063.

Yu, Z., Xia, Y., Du, D. & Ouyang, J. 2016. PEDOT : PSS Films with Metallic Conductivity through a Treatment with Common Organic Solutions of Organic Salts and Their Application as a Transparent Electrode of Polymer Solar Cells. DOI: 10.1021/acsami.6b00317.

Yu-Zhang, K., Guo, D.Z., Mallet, J., Molinari, M., Loualiche, a. & Troyon, M. 2008. Electrodeposition and Characterization of CdSe Semiconducting Nanowires. *Journal of Nanoscience and Nanotechnology*. 8(4):2022–2028. DOI: 10.1166/jnn.2008.055.

Zhang, G., Lin, B., Qiu, Y., He, L., Chen, Y. & Gao, B. 2015. Highly efficient visible-light-driven photocatalytic hydrogen generation by immobilizing CdSe nanocrystals on ZnCr-layered double hydroxide nanosheets. *International Journal of Hydrogen Energy*. 40(14):4758–4765. DOI: 10.1016/j.ijhydene.2015.02.055.

Zhao, J., Holmes, M.A. & Osterloh, F.E. 2013. Quantum confinement controls photocatalysis: A free energy analysis for photocatalytic proton reduction at CdSe nanocrystals. *ACS Nano*. 7(5):4316–4325. DOI: 10.1021/nn400826h.

Appendix A1

Table A 1.1: Chemicals and reagents

Reagent	Details	Supplier
Cadmium sulphate ($CdSO_4.8/3.H_2O$)	99.0%	Sigma-Aldrich
Selenium dioxide (SeO_2)	99.9%, trace metals basis	Sigma-Aldrich
Nickel (II) sulphate ($NiSO_4.6H_2O$)	99%	Sigma-Aldrich
Gold (III) chloride hydrate ()	99.999 % trace metals basis	Sigma-Aldrich
Chloroplatinic acid ($H_2PtCl_6.6H_2O$)	37.50 % Pt basis	Sigma-Aldrich
Boric acid (H_3BO_3)	99.97 % trace metal basis	Sigma-Aldrich
Poly(3,4-ethylenedioxythiophene)-poly(styrenesulfonate)	1.3 wt. % dispersion in H_2O, Conductive grade	Sigma-Aldrich
Sulphuric Acid	Analytic reagent	Kimix
Nitric Acid	Analytic reagent	Kimix
Sodium hydroxide flakes	Analytical reagent	Kimix
Acetone Isopropanol Glacial acetic acid	Analytic reagent	Kimix
25 mm anodised aluminium oxide membranes with polypropylene support ring	Thickness: 60 µm, pore diameter: 100 & 200 nm	Whatman®
13 mm anodised aluminium oxide membranes	Thickness: 60 µm, Pore diameter: 200 nm	Whatman®
13 mm anodised aluminium oxide membranes	Thickness: 50 µm, Pore diameter: 160 nm	InRedox®

Table A 1.2 : Comparison of theoretical Standard Reduction Potentials with applied and measured potentials during electrodeposition

Element	Reduction half-reaction	Standard Reduction Potential E° (V vs SHE)	Applied/Measured Potential E (V vs Ag/AgCl sat. 3.5 KCl)
Cd	$CdSO_4 + 2e^- \leftrightarrow Cd\ (s) + SO_4^{2-}$	-0.246	-0.3 to -0.8
Se	$H_2SeO_3 + 4H^+ 4e^- \leftrightarrow Se\ (s) + 3H_20$	0.74	-0.3 to -0.8
Ni	$Ni^{2+}(aq) + 2e^- \leftrightarrow Ni\ (s)$	-0.257	- 1
Au	$AuCl_4^- + 3e^- \leftrightarrow Au\ (s) + 4Cl^-$	1.002	-0.4 to -0.5*
Pt	$[PtCl4]^{2-} + 2e^- \leftrightarrow Pt\ (s) + 4Cl^-$	0.755	-0.4 to -0.5*

* Potentials stated for Au and Pt electrodepositions are the approximate steady-state potentials measured since these metals were deposited using a constant current of -0.35 mA and -0.25 mA respectively.

Table A1. 3 Mass to Charge ratios of species for detection using mass spectrometry

Species	N_2	O_2	Ar	H_20	H_2	CO_2	MeOH
m/z identifier	14	15.97	20.01	18	1.94	44.13	31.04